Acknowledgements

I would like to first, above all, thank God and my savior Jesus Christ who enabled me to complete this work and whose creation we seek to explore as scientists. Tremendous thanks to the members of my committee, Professors Walter and Zuiderweg for their insightful suggestions and support, and Professor Fierke for her exceptional ideas at the start of this project and mentorship and support throughout. I would like to thank my advisor Professor Al-Hashimi for his continual help and support. I would like to thank the members of the Al-Hashimi lab for their help and encouragement. Thanks to Qi and Alex for helpful discussions about spin relaxation and to Anette for helpful discussions about metal binding and for praying for me. Thanks also to Dr. Meredith Lambert who taught me how to assign an RNA.

I would also like to acknowledge my Mom, Dad, and sister Becky for their love, support, and encouragement. Thanks to Jia for his love and support. Last but not least, I would like to thank Melodie for keeping me accountable with work and faith and for continually praying for my research.

Table of Contents

List of Figures

Figure

List of Tables

Tables

List of Abbreviations

A – adenine
C –cytosine
C domain –catalytic domain of RNase P
CT – constant time
COSY – correlated spectroscopy
CPMG – Carr Purcell Meiboom Gill experiment
DNA –deoxyribonuclei acid
E-P4 – elongated P4
FID –free-induction decay
G – guanine
GDO (ϑ) –generalized degree of order
HIV-1 – human immunodeficiency virus
HSQC –heteronuclear single quantum coherence
INEPT – insensitive nuclei enhanced by polarization transfer
IPAP – in phase, anti-phase detection scheme
J3/4 –junction region between helix 3 and 4
MES - 2-(N-Morpholino)ethanesulfonic acid
miRNA – micro RNA
mRNA – messenger RNA
NAIM –nucleotide analog interference mapping
NcRNA – non-coding RNA
NMR – nuclear magnetic resonance
NOE –nuclear overhauser effect
NOESY –nuclear overhauser effect spectroscopy
P4 – paired region 4
PDB – protein data bank
PEG – polyethylene glycol
Pre-tRNA – precursor transfer RNA
RDCs – residual dipolar couplings
RMSD – root mean squared deviation
RNA - ribonucleic acid
RNase P – ribonuclease P
rRNA – ribosomal RNA
RNP – ribonucleoprotein

S domain – specificity domain of RNase P
SRP – signal recognition particle
TAR – trans-activation response element from HIV-1
trFRET – time-resolved fluorescence resonance energy transfer
TOCY – total correlated spectroscopy
TROSY – transferse relaxation optimized spectroscopy
U – uridine

Chapter 1

Introduction

The recent sequencing of the genome from a variety of organisms has spurred a structural genomics initiative which is seeking high-throughput structure determination of proteins as part of a broader goal: comprehensive molecular characterization of the network of molecular interactions governing cell function. Concurrently, a quieter revolution is uncovering a universe of non-coding RNAs (ncRNAs) with functions that go beyond messenger, translational, or ribosomal RNA. RNA interference, which involves non-coding RNAs, was discovered by Fire and Mello in their studies of gene regulation in *C. elegans*[1]. They received the Nobel Prize in 2006 in Medicine and have again brought RNA to the spotlight. A class of non-coding RNAs discovered even earlier by Cech and Altman catalyze reactions and are called ribozymes. One of the first ribozymes to be discovered was RNase P (ribonuclease P), whose highly conserved P4 helix is the focus of this thesis.

I. RNase P: Reaction catalyzed and proposed mechanism.

RNase P and tRNA processing

RNase P is an essential tRNA processing enzyme that cleaves the 5' leader of pre-tRNA to form the mature 5' end of the tRNA. It is found in all forms of life since it

performs an essential step in tRNA processing[2]. The different forms of RNase P in bacteria and eukaryotes make it a potential target for developing antibiotics while its ability to cleave a variety of RNAs is being exploited in practical applications such as gene therapy[3, 4]. The processing of tRNA is necessary because pre-tRNAs are transcribed together in one continuous unit along with some rRNA and mRNA[5]. In *E. coli*, processing begins by endonuclease RNase E cleaving the pre-tRNAs from each other and from other types of RNA. The 3' end is likely cleaved first to form the mature 3'-end before RNase P can act, since RNase P is inhibited by long 3' precursor sequences. In *E. coli*, processing of the 3' end is catalyzed by the enzymes RNases II, D, BN[6], T[7-10] and PH, which function stochastically[11](Fig. 1-1). After the mature 3' end is formed, RNase P cleaves the leader sequence of pre-tRNA, on average ~ 17 nt in length[12], to form the mature 5' end of tRNA. The sequence of processing events is different in eukaryotes and archaea than in bacteria because the last 3' processing enzyme, RNase Z, prefers shorter 5' ends so it likely acts after RNase P has generated the mature 5' end[13-17]. Processing of tRNA prepares it to be aminoacylated, catalyzed by tRNA sythetases, and then used as a substrate for protein synthesis catalyzed by the ribosome.

RNase P: catalyzed reaction and mechanism

RNase P catalyzes hydrolysis of a phosphodiester bond near the 5' end of pre-tRNA (Fig. 1-2A), as mentioned above, which is the last step in pre-tRNA processing in *E. coli* but occurs before 3' end processing in archaea and higher eukaryotes. RNase P catalyzes cleavage between the U^{-1} and the G^{+1} position in pre-tRNA to create a 5' product with a 3'-OH end and a mature tRNA with a 5' phosphate. Bacterial RNase P

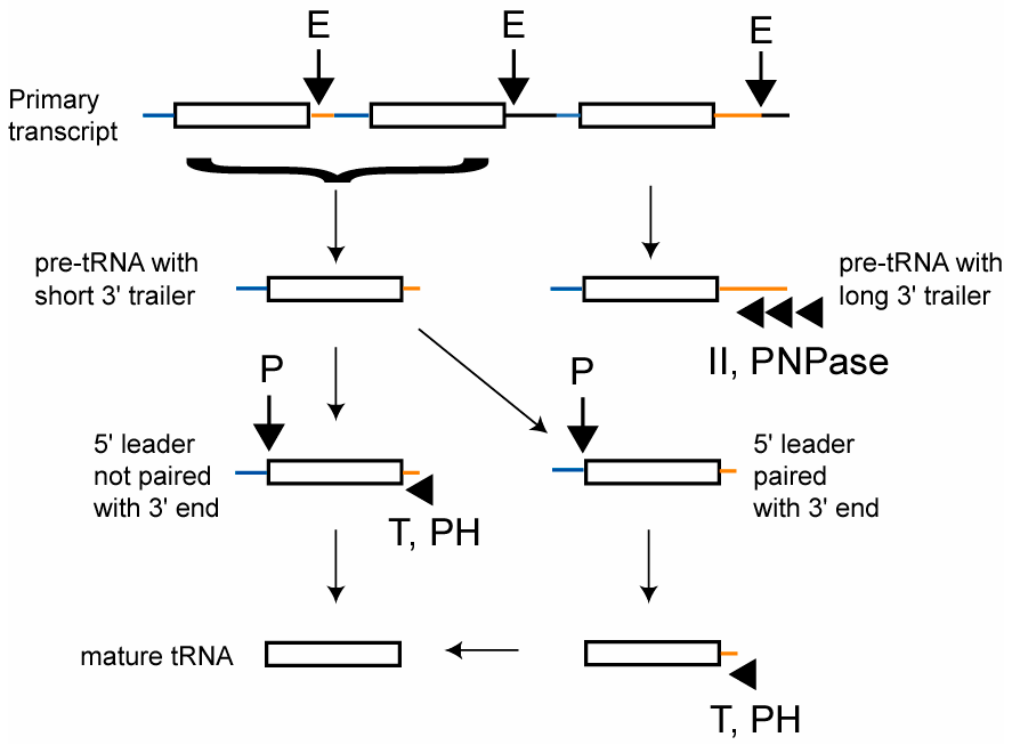

Figure 1-1. A proposed model for *E. coli* pre-tRNA processing. Boxes represent the core tRNA and lines are extra sequences: left side (blue) is the 5' end and the right side (orange) is the 3' end. Vertical arrows indicate endonuclease cleavage by the indicated enzyme and horizontal arrows are exonuclease activity by the indicated enzyme[11].

consists of a large (350–400 nt) essential RNA component, composed of a catalytic (C) domain and a specificity (S) domain, and one or more protein components (while archaea have 4 proteins and eukaryotes 9 or 10)[18, 19] that are dispensable for catalysis at high salt and metal concentrations; maximum catalytic activity occurs with 1 M monovalent ions and 10 mM Mg^{2+} [20, 21]. A very recent study has shown that the human form of P RNA also can perform catalysis very slowly in the absence of protein[22]. The catalytic mechanism is thought to involve S_N2-type in-line attack of the 5' phosphate by a metal activated solvent nucleophile at the G^{+1} position resulting in a trigonal bipyramidal intermediate involving the phosphate group on the 5' end of the mature tRNA (Fig. 1-2B)[23, 24]. The model for the possible locations of the stabilizing metal ions in the

intermediate is suggested by crystal structures of protein metalloenzyme phosphoryl transferases[24] and evidence for metal involvement in pre-tRNA binding and catalysis[25-30] (Fig. 1-2B) . What is known about the role of metal ions in RNase P will be discussed further in section II.

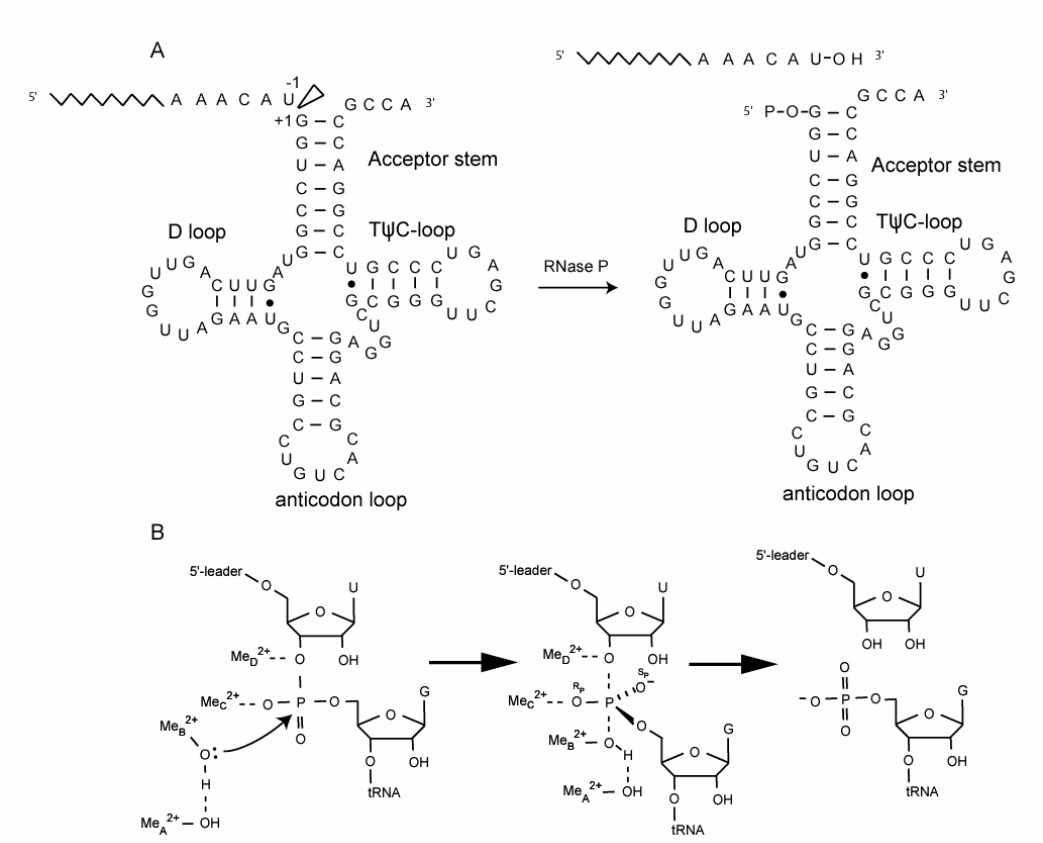

Figure 1-2. Reaction cleaved by RNase P and proposed mechanism. (A) Secondary structure of pre-tRNA showing the cleavage site between the U^{-1} and G^{+1} positions (left) and products of the RNase P reaction: mature tRNA (with 5'-phosphate) and the 5' end with a 3'-OH tail (right)[21]. (B) Proposed model for nucleolytic attack and subsequent cleavage in the backbone of the pre-tRNA through a trigonal bipyramidal intermediate coordinated by two or more metal ions[23, 24].

The role of P4 as an essential catalytic component of RNase P

The P4 helix is located at the junction of the RNase P catalytic and specificity domains and has the greatest number of universally conserved residues of RNase P (Fig.

1-3). A large body of work has established the importance of P4 in RNase P catalysis. Of particular importance are highly conserved residues near the U52 bulge that have been shown by cross-linking to be in close proximity (within 4.5 Å) to the 5' leader of the tRNA substrate[31, 32]. Phosphorothioate substitution studies[33-35] together with nucleotide

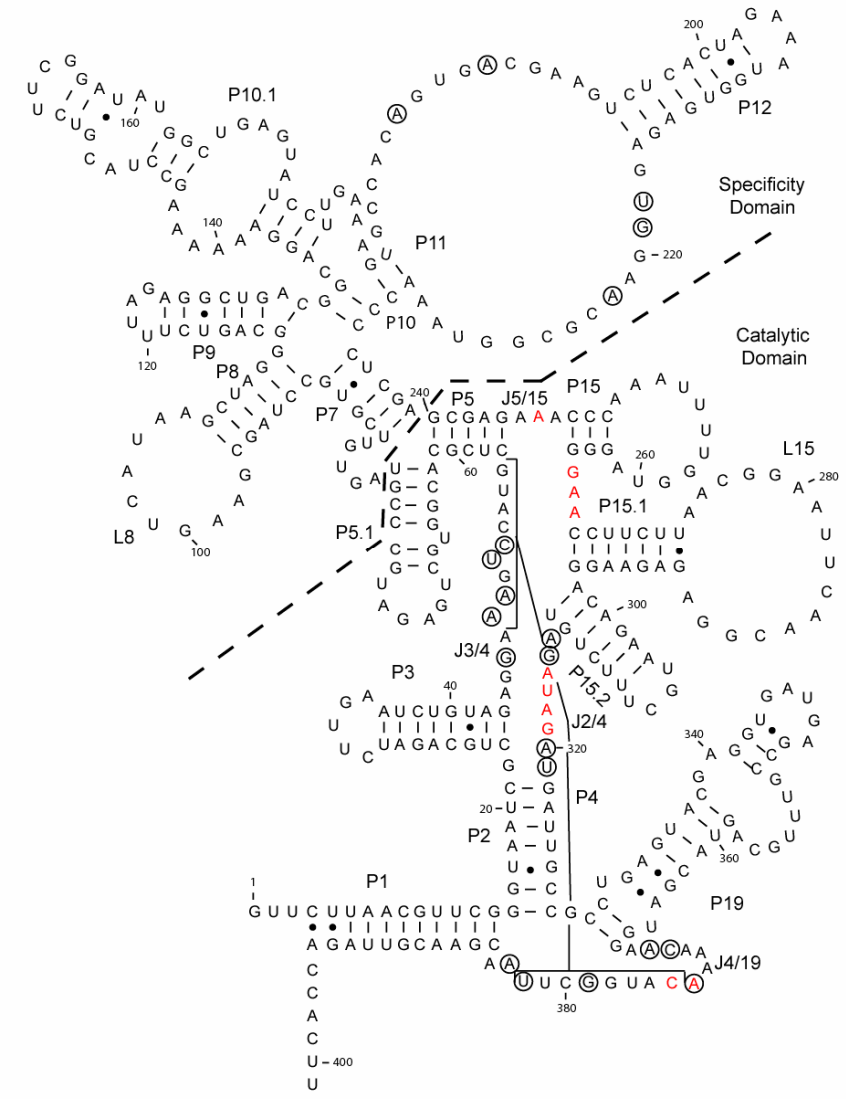

Figure 1-3. Secondary structure of RNase P *B. subtilis*. Universally conserved residues are circled[36]. Residues suggested as part of the active site in *B. stearothermophilus*[37] crystal structure are shown in red. Paired (P) and junction (J) regions are labeled. Dots indicate non-Watson Crick base pairs. Solid lines show the two strands of P4 which are base paired. The dotted line separates the two domains.

analog interference mapping (NAIM)[25, 38-41] have shown that residues below the bulge are important for both tRNA binding (Fig. 1-4, blue symbols) and catalysis (Fig. 1-4, red symbols). In many cases, the phosphorothioate substitution effects could be rescued by Mn^{2+}, suggesting the involvement of inner sphere coordinated metals in substrate binding[33] (Fig. 1-4, black filled blue arrows), catalysis[34, 35, 42], and/or structure needed for both (Fig. 1-4, black filled red arrows). The complete rescue of catalysis by Mn^{2+} of the phosphorothioate substitution at the A50 position raised the possibility that the water-activating catalytic metal binds to this site in P4[34]. Subsequent NMR chemical shift mapping experiments on the *E. coli* P4 helix alone revealed an alternative Mg^{2+} binding

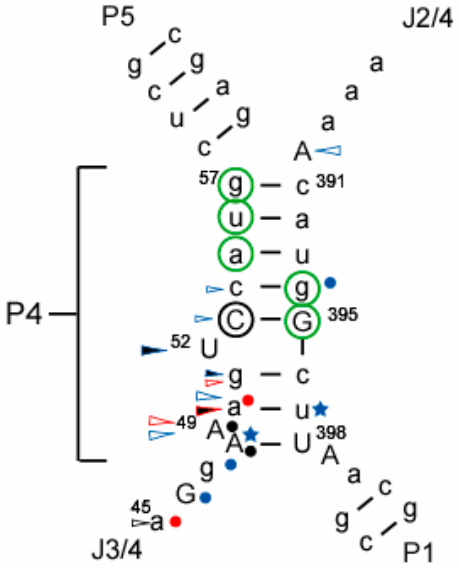

Figure 1-4. The P4 element of RNase P showing implications of key biochemical studies. (A) Secondary structure of P4 as seen in the crystal structure of *B. stearothermophilus* RNase P[37]. Green circles indicate Mg^{2+} binding sites identified in *E. coli* P4 by NMR[43]. Black open circle indicates a site of mutation that disrupts catalysis[44], arrows indicate sites where phosphorothioate substitutions interfere with catalysis (red) and substrate binding (blue) or both[33-35] (black), black filled arrows indicate sites that are rescued with Mn^{2+} [33-35], filled circles indicate sites where nucleotide analog substitutions interfere with catalysis[25, 40] (red), substrate binding[39, 41] (blue) or both[25, 40, 41] (black), blue stars indicate 2'OH sites that are important for substrate binding[38]. Upper case letters are universally conserved residues in RNase P bacteria and archaea[45].

site above the bulge[43] (green circles, Fig. 1-4). A C53 to U53 mutation above the bulge significantly improves the enzyme's ability to use Ca^{2+} as the catalytic metal[44] (black open circle, Fig. 1-4), possibly due to a change in the P4 conformation involving the position of the uridine bulge[43]. While there is a lot of biochemical evidence suggesting that important metal binding sites are located in P4, the positions and roles of each bound metal ion have yet to be deciphered. Additionally, the exact location of the active site of the enzyme is unclear.

The precise role of P4 in catalysis remains to be elucidated, although it has been shown that the P4 bulge is required for catalysis. Changing the bulge identity has modest effects on catalysis while disrupting the sequence above or below the bulge has drastic effects[46]. A recent NMR study demonstrated that mutations that move the uridine bulge in the 5' direction by one nucleotide cause the bulge to change from a minor to a major groove location and move the Mg^{2+} binding site. However, changing the bulged uridine to an adenine had no effect on structure or Mg^{2+} binding properties[47]. Alterations in the bulge and surrounding sequence in P4 affect catalytic activity, but how and why remains unclear. Given its central location near the substrate binding site based on 3D structural models[48], there is little doubt that the RNase P catalytic cycle, beginning with folding and assembly of the ribonucleoprotein followed by recognition of substrate, catalysis, and finally product release, will require changes in the P4 conformation that allow the structural requirements of these distinct steps to be dynamically satisfied by a single enzyme. An increasing number of studies indicate that the dynamical properties of RNA structures play an important role in such adaptive conformational changes[49-51].

Structural and dynamical basis for catalysis

High-resolution structures of the RNA component of RNase P together with 3D structural models obtained from cross-linking with the substrate and product provide possible locations for the active site and evidence for dynamics during the catalytic cycle. To date, there have been four crystal structures of the RNase P RNA component: the specificity domains of *B. subtilis*[52] and *T. thermophilus*[53], and the full RNA domains (with catalytic domain) of *T. maritima*[54] and *B. stearothermophilus*[37] at 3.85 Å and 3.3 Å respectively (Fig. 1-5). The two crystal structures of the entire RNA from A-type[54] and B-type[37] bacteria show an overall flat enzyme with P4 in the center at the junction of four helical domains (P2, P3, P5, and P19) where it forms tertiary interactions with loop L8. While both studies suggest that the active sites contain the J5/15 and J2/4 (J4/19 in B-

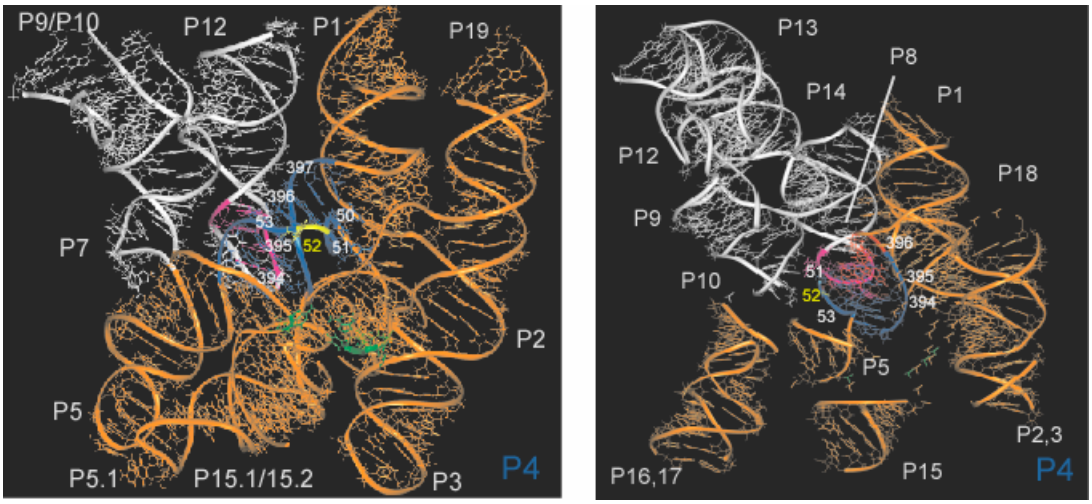

Figure 1-5. Crystal structures of *B. stearothermophilus* P RNA (left)[37] and *T. maritima* (right)[54]. Highlighted in color are P4 (blue), P4 bulge (yellow), L8 (pink), the specificity domain (white), the catalytic domain (orange), and tRNA cross-link regions (green)[55].

type) region, analysis of the B-type crystal structure also suggests the involvement of J2/15.2 and P15 (red residues, Fig. 1-3). Both models include sites in P4 as part of the active site, but the residues involved are in different domains. In the B-type crystal one

distal residue in P4 near J2/4 is listed while in the A-type crystal an adenine below the bulged uridine is included; only the latter site is consistent with biochemical studies. The reason for the different proposed active site regions is the reliance on different tertiary structure models created by each research group for the location of the pre-tRNA and the location of bound metal ions. The B-type structural model is based on pre-tRNA cross-links to the C domain while the A-type model is based on cross-links to the S domain[56] resulting in different pre-tRNA locations. Location of the active site in the B-type crystal was also based on a Pb^{2+} binding site discovered near the pre-tRNA cross-link sites (U56-A392 and G57-C391, which correspond to U55-A376 and G56-C375 in *B. subtilis*); Pb^{2+} was used to identify possible inner sphere Mg^{2+} binding sites. Although another Pb^{2+} binding site was seen in P4, its distance from the position of the modeled substrate prevented it from being chosen as part of the active site[37].

There are uncertainties present in both crystal structures that limit interpretation as well as evidence that the structures may not be of an active form of P RNA. The conformations of P15/L15/P16 in the A-type crystal and P15.2 in the B-type crystal are different from those predicted from *in vitro* studies, suggesting that the structures are not in the active form and may change upon substrate binding[37, 54]. The missing residues (25-30 % in A-type and 25 % in B-type) and the low resolution of the A-type (3.85 Å) crystal structure fail to give a complete picture of the structure of RNase P[54]. In the B-type crystal, although metal ions are mentioned, the need for further refinement prevented the authors from reporting them in the structure (PDB ID#2A64), so the locations of the bound metals in RNase P remain to be determined. Importantly, the active sites proposed by these authors are far from P4[55] (cross-link sites in green and P4 in blue; Fig. 1-5)

which has been shown to contain catalytically important metals by biochemical data. Thus, any direct involvement of P4 in catalysis would require a conformational change following substrate binding for which there is indirect evidence, as discussed below.

Structural models that have been proposed based on biochemical data for the location of the pre-tRNA substrate in relation to the enzyme are helpful for examining possible catalytic sites. Preliminary structure models of RNase P RNA were developed based on comparative photo-crosslinking analysis and comparative sequence analysis[57, 58]. After crystal structures had been solved for the P protein in *B. subtilis* and *T. maritima* (and confirmed by an NMR structure solved for *S. aureus)*[59-61], the protein and the crystal structure of tRNA[62] were docked onto the RNA by molecular modeling using the following tertiary interactions: (i) the base-pairing between the terminus of the pre-tRNA and loop L15 of M1 RNA (ii) functional groups in the T stem-loop of the pre-tRNA substrate that interact with the paired regions P9 and P11 of the RNA, and (iii) the binding of the pre-tRNA leader (nucleotides -4 to -8) in the cleft of the protein cofactor (Westhof model)[48]. A recent study calculated a new tertiary structure model with the addition of new cross-linking and affinity cleavage information[63] to the original structure model[57]. Then, new models of the complex were generated based on the solved crystal structures of *T.maritima* (Mondragon model)[53] and *B. stearothermophilus* (Pace model)[41] and the cross-linking data of the pre-tRNA to the RNA enzyme.

There are several common features between the models based on crystal structures and the Westhof model: the location of the pre-tRNA is on the same side of RNase P, the TΨC loop interacts with nucleotides in the S-domain, and the 5' end of the tRNA lies near the C-domain (Fig. 1-6). Differences between models include orientation

of the anticodon loop of the tRNA with respect to RNase P, the locations of the 5' and 3' ends, and different locations for the base of the acceptor stem. Importantly, one key feature that all three have in common is that P4 is shown running parallel to the acceptor stem of the pre-tRNA substrate (Fig. 1-7)[37, 48, 54, 56]. This implicates that the structural and metal binding properties of P4 could be essential for substrate binding. The fourth model, developed recently based on protein cross-linking and affinity cleavage, positions the -1 cleavage site in the pre-tRNA very near both the protein and P4[63]. This suggests a role in P4 as part of the structural scaffold of the active site. Despite the structural information and models for RNase P, lack of a substrate bound/active structure prevents direct

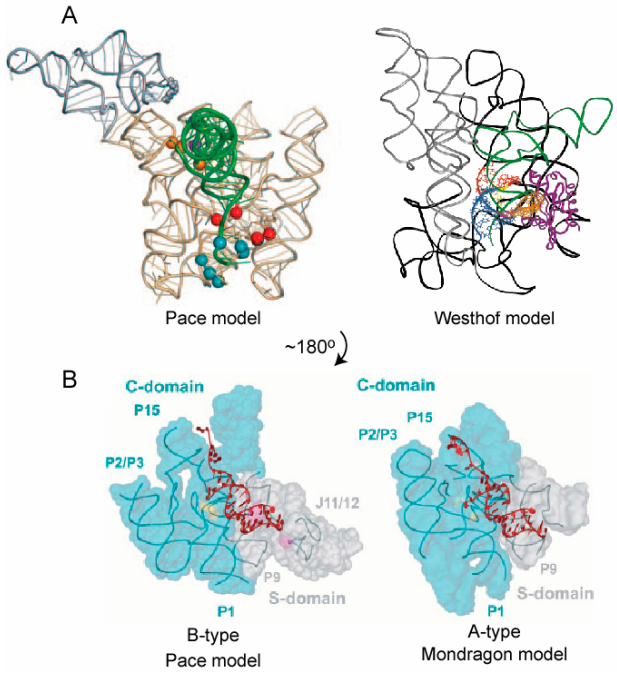

Figure 1-6. 3D structural models of RNase P holoenzyme. (A) Left: Pace structural model with the B-type crystal[41]. Catalytic domain is shown in yellow, specificity domain in grey, tRNA in green, colored dots: sites of photoaffinity cross-linking of tRNA to RNase P (different colors represent different sites of cross-linking) Right: Westhof model for *E. coli* RNase P based on biochemical data alone[48] and crystal structures of tRNA and protein[61]. Catalytic domain is shown in black, specificity domain in grey, P4 in red and blue, tRNA in green, 5' leader of pre-tRNA in orange, and protein in purple. (B) B-type (left)[41] and A-type (right)[53] structural models of RNase P (C-domain in blue, S-domain in grey) and the acceptor stem of the tRNA (red).

evidence for the location of the active site and the catalytic metal.

Another key functional area that remains to be fully characterized in RNase P is the presence of dynamics and its role in the catalytic cycle. Many enzymes undergo conformational changes during their catalytic cycles[64-67]. For RNase P there is indirect

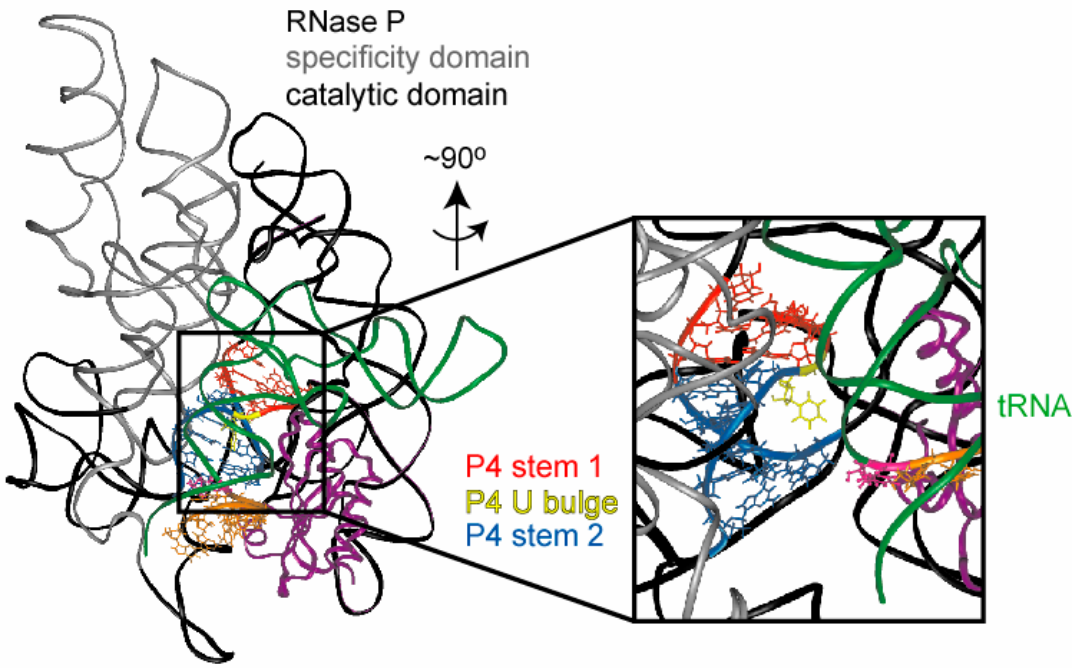

Figure 1-7. Structural model by Westhof and co-workers of bacterial RNase P[48] (black/grey) with protein (purple)[61] and pre-tRNA (green). The P4 sequence is highlighted in red (domain 1) and blue (domain 2).

evidence for the involvement of dynamics in catalysis. Both the large distance between cross-link sites on the RNA and lack of pre-tRNA and S-domain overlap which would be necessary for high-affinity substrate binding observed in *in vitro* assays, suggest that a conformational change is required for the active site to be fully formed upon substrate binding. It has been suggested that local structural changes may occur during the formation of the RNA-protein complex in *E. coli* since the association rate of the RNase P protein was reported to be 10- to 100-fold slower than expected for diffusion-controlled

binding[68, 69]. A third line of evidence for dynamics involves cross-linking studies done by Pomeranz Krummel and co-workers which revealed different substrates of RNase P that formed different cross-links and hence had different binding modes to the enzyme[70]. Future studies will reveal the structural basis for these transitions and their importance in the catalytic cycle.

II. RNA and metal ions

Role of metal ions in RNA folding

The home of RNA within an organism is in the interior of a cell which contains salt at around 150 mM. The intracellular concentration of Mg^{2+} is highly disputed but can be from 0.1 to 6 mM Mg^{2+}[71] or up to 10mM and can vary between cells and over time in response to signals or stresses[72]. RNA is a polyanionic polymer with nearly one negative charge (0.94 K^+) per residue/phosphate[73]. Formation of compact RNA structures leads to formation of unstable regions with high negative electrostatic potential. Metal cations provide a means for neutralizing this high electrostatic potential and therefore are essential to RNA folding. This was first demonstrated in studies of tRNA[62] and later extended to many other RNAs including catalytic RNAs such as the hammerhead ribozyme[74], group I intron[75], RNase P[37, 54] and the ribosome[76]. For example the loop E motif in the ribosome binds Mg^{2+} as a binuclear cluster that joins neighboring backbones and brings them into unusually close proximity[77]. Another example is in the P4-P6 domain of the Tetrahymena group 1 self-splicing intron where an adenine rich bulge and a GAAA tetraloop form an essential tertiary interaction which brings two helices into close proximity[78]. Mg^{2+} ions play a vital role in stabilizing these inter-domain

interactions by bridging backbone phosphates. Another mode for Mg^{2+} interactions with RNA is derived from the bases, specifically tandem purines in which one or more metal ions are bound to consecutive purines through interactions with the O6 and N7 atoms that form negative pockets in the major groove. This motif can be seen in a variety of RNAs such as the leadzyme[79] and ribosome[76].

Role of metal ions in RNA catalysis

Following the discovery of RNA catalysis, it was thought that all RNA enzymes required metals as an essential catalytic functional group. Then in the hairpin ribozyme it was shown that Mg^{2+} could be substituted by aminoglycosides, spermine, or monovalent ions and hence only played a structural role[80-83]. Similar observations were later reported for the hammerhead ribozyme[84]. In contrast, for the larger ribozymes, RNase P and the group I and II introns, divalent ions are absolutely required for activity[85-89].

Interactions between cations and RNA can be categorized as either diffusely bound or site bound[90]. Diffusely bound ions are often referred to as a "delocalized cation atmosphere" and can be modeled by the non-linear Poisson-Boltzmann equation[91, 92]. Site bound metal ions usually make two or more direct contacts to functional groups in the RNA either through outer or inner sphere interactions[93]. Outer sphere refers to a shell of hydration surrounding metal ions in solution (Fig. 1-8A). Outer sphere interactions are water-mediated contacts whereas inner sphere contacts involve direct interactions between the metal and functional groups on the RNA[90]. The ability of a metal to form inner sphere contacts with RNA (i.e. to replace one of the water ligands with an RNA functional group) can be correlated with the pK_a of the metal-bound water molecule[94] and

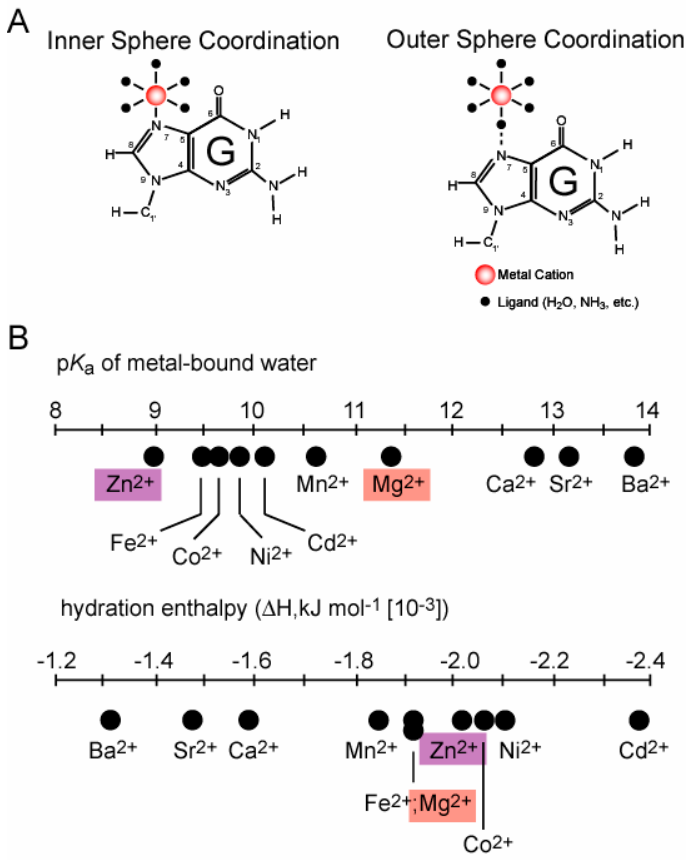

Figure 1-8. Types of RNA-metal coordination and metal cation properties. (A) Schematic representation of a six-coordinate metal cation bound to RNA. In this example, the metal cation is bound directly to the N7 of guanine (inner sphere) or to N7 through a water-mediated interaction (outer sphere). (B) Physicochemical properties of various metal cations. Shown here are the pK_a of the metal-bound water and the hydration enthalphy[94, 95].

its hydration enthalpy, calculated from the charge and ionic radius of the metal[96]. Hydration enthalpy is often used to compare properties of metals but the actual energy required for hydration includes an entropy term and is given by the free energy of hydration[93].

Magnesium is the most frequently utilized metal in RNA folding and this metal accelerates catalysis in some RNAs. Magnesium is considered a "hard" metal but it has a more negative hydration enthalpy than the other hard metals and can form inner sphere

contacts under the right conditions (Fig. 1-8B). Mg^{2+} can interact with RNA via outer or inner sphere interactions, and distinguishing these modes and their relative importance to RNA folding and catalysis is generally difficult and an important biophysical problem. Most approaches involve directly probing activity following metal and RNA substitutions. For example, in Mn^{2+} rescue experiments the "hard" backbone oxygen, which is prone to contact the "hard" Mg^{2+} metal, is replaced with the softer sulfur ligand, which prefers to bind the softer metal Mn^{2+}. In this way, one can monitor if an inner sphere metal is important for a given process[96]. Another approach is to examine outer sphere metal ion coordination using cobalt (III) hexamine $Co(NH_3)_6^{3+}$ which has a similar size as fully hydrated Mg^{2+} but which is much less likely to form inner-sphere interactions because its kinetically stable ammonia ligands are less likely to exchange with water[97]. One can also examine inner sphere binding sites using Zn^{2+} or Cd^{2+}, whose water protons have pK_a's of 9 and 10, respectively, compared to Mg^{2+}'s pK_a of 11.5 and so are more likely to become deprotonated at neutral pH[94]. Zn^{2+} is considered a borderline metal and Cd^{2+} a soft metal due to its favorable hydration enthalpy[95] (Fig. 1-8B). Inner sphere metals have been observed in the group I self-splicing intron[78], an RNA/DNA four-way junction[98], and human signal recognition particle[99].

Role of metal ions in RNase P

In RNase P, Mg^{2+} is required for proper folding of the enzyme, substrate binding, and catalysis[27, 100, 101]. There are most likely multiple ions involved, each of which can take on different roles. The proposed roles of Mg^{2+} ions in the catalytic cycle include: initiation of catalysis by activation of a nucleophilic water molecule, electrostatic

stabilization of the trigonal bipyramidal transition state, and aiding in tertiary structure formation of the enzyme-substrate complex[34]. Studies on the *E. coli* enzyme have shown that catalysis can occur also with Mn^{2+} and Ca^{2+}, but Mg^{2+} activates cleavage most efficiently[26, 28, 102-107]. The metals Mn^{2+}, Ca^{2+}, Sr^{2+}, Ba^{2+}, NH_4^+, and $Co(NH_3)_6^{3+}$, which mimic the fully hydrated outer shell of Mg^{2+}, can support proper folding of RNase P[108, 109]. There are other metals that can substitute for the catalytic role of Mg^{2+} such as Zn^{2+} and Cd^{2+}, which likely make inner-sphere, direct RNA contacts, but are inhibitory unless combined with one of the above folding metals[108]. While the types of metal ions required for catalysis are known, neither the exact location of the metals nor their exact roles have been determined.

II. History of and basic theory of NMR and applications to study ribonucleic acids

Early experiments and basic theory

The first nuclear magnetic resonance (NMR) experiments began in December of 1945 when Purcell, Torrey, and Pound detected weak radiofrequency signals generated by the nuclei of atoms in paraffin wax[110]. About the same time Bloch, Hansen, and Packard observed radiofrequency signals in water[111]. Nuclear magnetic resonance, as the name implies, is based on properties of the nuclei of atoms in a magnetic field, in particular the spin angular momentum of the nuclei which is an inherent quantum mechanical property. In order for the spin to be detectable by NMR, the nuclear spin must be nonzero. This occurs when the nucleus has either an odd mass number (the sum of protons and neutrons) or an even mass number and odd atomic number (number of

protons). The former have spin quantum numbers (I) of half-integers whereas the latter category have integer spin quantum numbers. The most commonly used NMR nuclei in biological applications are those with I = ½ : ^{1}H, ^{13}C, ^{15}N, ^{19}F, and ^{31}P and I = 1: ^{2}H. A nucleus with a spin of ½ in the presence of a magnetic field can exist in either of two states corresponding to two equally spaced energy levels which result from the projections of the angular momentum of the nuclei onto the z-axis of the laboratory frame, known as Zeeman levels. These energy levels are given by $E = -m\hbar\gamma B_o$ where m is the magnetic quantum number, which ranges from –I to +I in integer intervals, ħ is Plank's constant, γ is the gyromagnetic ratio of the nucleus and B_o is the magnetic field[112]. At equilibrium, the two states assume a Boltzmann distribution causing a net magnetic moment **M** to develop along the z-direction[112]. Typical NMR experiments involve the application of multiple radio frequency pulses designed to manipulate the magnetization in order to detect the chemical properties of interest.

Pulsed Fourier transform spectroscopy, developed by Ernst[113], was one of two great advancements that began the explosive growth of NMR that is continuing today. The other is the concept of multidimensional NMR spectroscopy developed by Jeener[114, 115] which has greatly increased the application of NMR to large complex macromolecules that are characterized by congested spectra. The ability to rapidly prepare NMR labeled ($^{15}N/^{13}C$) RNAs by *in vitro* transcription in the 1990s greatly expanded application of this technique to studies of RNA[116].

NMR is currently one of only two techniques for high resolution structure determination of biomolecules (X-ray crystallography being the other). In some cases, NMR structures can be more easily solved for a given RNA since many RNAs are

difficult to crystallize, often due to the presence of high flexibility areas. Also, crystal packing forces and high salt/metal conditions can force the RNA into non-physiologically relevant structures[116]. NMR has its limitations as well, size being the most significant. Large molecules have slower tumbling rates which lead to very broad resonances that make interpretation and/or detection difficult. However, a great advantage of NMR is that it can also be used to site-specifically probe dynamics on a variety of timescales: lineshape analysis[117] and ZZ-exchange spectroscopy[118] can be used to probe slow processes at second timescales, imino proton exchange can be used to probe base-opening motions at millisecond timescales[119], chemical exchange can be used to probe conformational transitions occurring at micro-to-millisecond timescales[120], spin relaxation measurements can be used to probe diffusive fluctuations at pico-to-nanosecond timescales[121] and residual dipolar couplings can be used to probe motions occurring at sub-millisecond timescales[122]. Also, NMR chemical shifts are extremely sensitive to changes in chemical environment which can be used to detect intermolecular interactions, including the interactions between RNA and metal cations.

Resonance assignment in nucleic acids by NMR

One of the most essential and often challenging parts of NMR studies of biomacromolecules is the assignment of resonances. Assignment methods utilize different techniques for unlabeled samples vs. labeled (^{13}C and/or ^{15}N) RNA samples. In unlabeled samples inter-residue NOEs (dipolar, through space interactions) are used to correlate sequential bases through the imino protons of uridine and guanine. The NOE interactions can also help identify hydrogen bond alignments. For example, an A-U base

pair has a strong NOE cross-peak between the uracil H3 imino proton and the adenine base H2 proton. In G-C base pairs the H1 imino proton of guanine has strong NOE cross-peaks to the H4 amino protons of cytosine[123]. Additionally, imino protons can be correlated to amino protons within the same base. NOE cross peaks can also be used to establish both intra- and inter-residue correlations between base and sugar protons. For example, in A-form helices, the base H6 proton in pyrimidines (or H8 in purines) can be correlated to its own sugar H1' and the proceeding H1' in the 5' direction. This gives rise to the so-called NOE walk which can be used to assign H2, H6, H8, and H1' protons from the 3' to the 5' direction in A-form helices.

Correlations can also be established based on through bond scalar couplings. For example homonuclear COSY (correlated spectroscopy, through bond) experiments can be used to establish correlations between protons that are three bonds or less apart, such as between H5 and H6 in purine bases and between the ribose H1'-H2', H2'-H3', H3'-H4', H4'H5' and H4'H5" (although H4', H5', and H5" usually have a high degree of overlap)[124]. Heteronuclear COSY experiments which involve the phosphorous in the backbone (^{1}H-^{31}P HETCOR), correlate the P to H3' and H5' which can then be used with the above sugar COSY experiment to connect the backbone and sugar protons through H4'[125, 126]. Longer range correlations can be established using homonuclear TOCSY experiments (total correlated spectroscopy) such as between H1' and H3' or heteronuclear TOCSY experiments such as an HCP experiment which allows correlations between phosphorous and H4' and H2' protons in addition to the usual H3' and H5' correlations[127].

There are three limitations in assigning resonances in unlabeled RNA that can be overcome using multidimensional heteronuclear NMR experiments on ^{13}C and/or ^{15}N

labeled RNA samples. This is particularly the case for larger RNAs in which spectra begin to suffer from severe overlap. For example, through a series of INEPT transfers, the 3D HCN experiment can be used to correlate base protons (H6/H8) and nitrogen atoms (N1/N9) to the intra-residue H1'[128]. This can significantly help lift ambiguities in distinguishing between intra- and inter-residue NOEs particularly since the nitrogen resonances are well resolved according to residue type[129]. A 3D HNCO experiment can be used to correlate imino protons with the C2 and C6 carbons in guanine and the C2 and C4 atoms in uracil. The chemical shifts of these carbons are uniquely sensitive to hydrogen bond alignment and can be used to confirm non-canonical hydrogen bond alignments[123]. Experiments that connect protons through more than two bonded carbons atoms are HCCH-TOCSY experiments. These can be used to correlate H2 to H8 protons[130] for example. Both homonuclear (C-C) and heteronuclear (C-N) transfers can be used to correlate atoms within the base[131]. One example is an HCCNH-TOCSY which correlates the base H6 in uracil to the imino H3. There are many examples of experiments that combine INEPT, COSY, and TOCSY transfers to correlate additional resonances within the base (see reviews[116, 123]). Finally, triple resonance 3D and 4D experiments combining NOESY and carbon or nitrogen HSQC type experiments, such as 3D NOESY-HSQC, HSQC-NOESY and nitrogen/carbon edited (or filtered) experiments can be used to greatly resolve ambiguities in NOE spectra.

Traditional NMR structure determination using short-range restraints

One of the most widely used applications of NMR is in structure determination. Traditionally, NMR structure determination relied heavily on distance constraints

obtained from NOEs[132]. NOE cross peaks can be observed between protons that are < 5 Å apart and their intensity can be related to $1/r^6$, where *r* is the inter-nuclear distance. For proteins, a very large number of these short-range distance constraints can be measured which greatly reduces the number of possible structures; NOEs are often observed between protons that are far apart in sequence[124]. However, such "long-range" NOEs are far less common in nucleic acids because nucleic acids have more extended conformations and have a lower proton density than proteins. Furthermore, propagation of errors in measured NOEs along the RNA polynucleotide chain can result in extremely ill-defined global conformations[133]. For example, changes in the orientation of helical stems can lead to only small differences in inter-proton distances and hence observed NOEs. Compounding this limitation is that residues at helical junctions are often highly flexible thus complicating the interpretation of measured NOEs. Measurement of ^3J scalar couplings can provide local constraints on a variety of angles including β ($^3J_{H5'P5'}$,$^3J_{H5''P5'}$, and $^3J_{H4'P5'}$), ε ($^3J_{H3'P3'}$ or $^3J_{H4'P3'}$ and $^3J_{H2'P3'}$), γ ($^3J_{H4'H5'}$ and $^3J_{H4'H5''}$ or many ^1H-^{13}C scalar couplings in the backbone such as $^3J_{C3'H5'}$ and $^3J_{C3'H5''}$), and χ ($^3J_{H1'C8/6}$ and $^3J_{H1'C4/2}$)[116, 134]. However, conformational averaging can complicate analysis of scalar couplings and their accurate measurements become increasing difficult in large RNAs. Further, these long range angular restraints do not remedy the problem of having a poorly defined global conformation. Hence, the aspect of RNA that is most sensitive to crystal packing forces has unfortunately proven to be the most difficult to define reliably based on traditional solution NMR techniques.

Use of RDCs in obtaining global information about structure and dynamics

Over the last decade, advances in NMR methodology have allowed the measurement of residual dipolar couplings (RDCs). Early applications included structure determination of small organic molecules in partially ordered liquid crystals[135]. Recently, they have been applied to biomolecules and used to determine structure and dynamics[136, 137]. They are particularly useful for providing long-range orientational constraints which are highly complementary to short-range distance constraints obtained by NOEs and hence have greatly facilitated structure determination of extended structures such as multi-domain proteins and nucleic acids[138].

RDC measurements make use of the dipolar coupling interaction and hence are orientation dependent by $(3\cos^2\theta-1)/2$ where θ is the angle between an inter-nuclear vector and the magnetic field. The dipolar interaction is rendered time-dependent due to variations in the angle θ caused by overall molecular tumbling and internal motions of biomolecules in solution. Motional averaging will generally reduce the value of the angular contribution and if the overall tumbling is random, the dipolar couplings will average to zero and are not measurable under normal solution conditions. However, if a degree of alignment can be imparted on the solute of interest, the angular term will no longer average to zero. The greater the degree of alignment the greater the value of the angular term and magnitude of observed dipolar couplings.

There are many different ways that one can choose to align biomolecules: bicelles[139, 140], rod-shaped viruses such as Pf1 phage and TMV[141-143], purple membrane[144, 145], and polyacrylamide gels[146, 147]. Usually the type of alignment media is chosen which has proven reliable at the desired temperature, pH, and salt concentration (for a list of

optimum conditions see the review[148]). The charge of the alignment media is also chosen in order to have the desired extent of interactions with the solute; as in the case of bicelles, the charge can be modified to be positive or negative with addition of CTAB or SDS, respectively[139, 140].

RDCs can be measured as new contributions to scalar couplings (J) that are observed under conditions of molecular alignment (J+D). Different types of experiments that have been developed for measuring one, two, and three bond RDCs in nucleic acids are listed in Table 1-1. Once a set of RDCs is measured, structural information can be obtained by two methods: the simulated annealing approach which incorporates RDCs into a penalty function along with NOEs and other restraints, and calculates a lowest energy minimum structure[149-151] and by order tensor analysis to determine the relative orientation of fragments[138, 152]. The former approach can be generally applied to any RNA target, provided that a sufficient number of experimental restraints (including RDCs) are measured and care has been taken to exclude RDCs that may have been attenuated by local motions. The latter approach involves using RDCs to determine order tensors describing the average alignment of molecular fragments relative to the applied magnetic field. Here, the relative orientation of RDC targeted bond vectors (α) in a

Table 1-1. Pulse sequences for the measurement of C-H, N-H, C-N, C-C, H-H RDCs in nucleic acids (courtesy of Qi Zhang)[148].

Pulse Sequence	Type of RDCs	Comments
HC[C](C) hd-TROSY-E.COSY[153]	$^1D_{C2H2}$, $^1D_{C5H5}$, $^1D_{C6H6}$, $^1D_{C8H8}$, $^1D_{C4C5}$, $^1D_{C5C6}$, $^2D_{C5H6}$, $^2D_{C6H5}$ and $^2D_{C4H5}$	-Pseudo-3D experiments for homonuclear decoupling employing TROSY and E.COSY elements.
CH_2-S^3E HSQC[154]	$^1D_{(C5'H5'+C5'H5'')}$ and $^2D_{(H5'H5'')}$ (in DNA only $^1D_{(C2'H2'+C2'H2'')}$ and $^2D_{(H2'H2'')}$)	-2D experiments with spin-state selection for detection of up- or downfield carbon components of CH_2 spin states.
3D S^3CT E.COSY[155]	$^1D_{C4'H4'}$, $^2D_{C5'H4'}$, $^1D_{(C5'H5'+C5'H5'')}$, ($^1D_{C5'H5'[']}$ - $^2D_{H5'H5''}$), $^2D_{C4'H5'+C4'H5''}$, and $^3D_{H4'H5'[']}$	-3D experiments for measuring RDCs in methine-methylene C-H pairs. One experiment yields 8 splittings.
H1C1C2 E.COSY[156, 157]	$^1D_{C1'H1'}$, $^1D_{C2'H2'}$, $^2D_{C1'H2'}$, $^2D_{C2'H1'}$, and $^3D_{H1'H2'}$	-3D experiment utilizing E.COSY for measuring five splittings in one experiment.
IPAP HN-HSQC, IPAP H(N)C-HSQC[158]	$^1D_{N1H1}$, $^1D_{N3H3}$, $^2D_{H1C2}$, $^2D_{H1C6}$, $^2D_{H3C2}$, and $^2D_{H3C4}$	-2D experiments yielding 1-2 couplings per experiment.
3D IPAP-HCcH-COSY 3D relay-HCcH-COSY[157, 159]	$^1D_{C2'H2'}$ and $^1D_{C3'H3'}$,	-Uses C1'H1' to alleviate spectral overcrowding in the C2'H2' and C3'H3' region.
MQ-HCN[160]	$^1D_{C1'H1'}$, $^1D_{C1'N1/N9}$, $^1D_{C1'C2'}$, $^2D_{H1'N1/9}$, $^2D_{H1'C2'}$, $^2D_{H1'N1/9}$, $^1D_{C6H6}$, $^1D_{C6N1}$, $^1D_{C6C5}$, $^1D_{C8H8}$, $^1D_{C8N9}$, $^2D_{H8N9}$, $^2D_{H6N1}$, and $^2D_{H6C5}$	-Suite of six MQ based 3D experiments. One - two splittings per experiment.
S^3E IS[T][161]	^1D and ^2D	-2D experiments for measuring most of the one and two bond splittings.
^{13}C-^1H TROSY[162]	$^1D_{C2H2}$, $^1D_{C5H5}$, $^1D_{C6H6}$, and $^1D_{C8H8}$	-Sensitivity enhanced using TROSY and native ^{13}C magnetization.
3D MQ/TROSY-HCN-QJ[163]	$^1D_{C1'N9}$, $^1D_{C8N9}$, $^1D_{C4N9}$, $^1D_{C1'N1}$, $^1D_{C6N1}$, and $^1D_{C2N1}$	-3D quantitative J-modulated experiments for measuring one bond C-N splittings.

fragment is assumed to be known. Thus, five or more independent RDCs can be used to compute the five elements of S_{ij} using the relation[164]:

$$D = -\frac{\mu_o \gamma_i \gamma_j h}{8\pi^3 r^3} \sum_{kl} S_{kl} \cos(\alpha_k) \cos(\alpha_l) \quad (1)$$

where μ_o is the magnetic permittivity of vacuum, γ is the gyromagnetic ratio, h is Planck's constant, r_{ij} is the distance between the spins, and α_n denotes the angle between the inter-nuclear vector and the n^{th} axis of the arbitrary molecular frame. The averages that describe the ordering of the molecule are represented by the terms S_{kl}, which form the elements of a Cartesian 3 X 3 matrix which describes the order tensor[165]. Two

principal order parameters[166] can be used to define the degree $\left(\vartheta = \sqrt{\frac{2}{3}(S_{xx}^2 + S_{yy}^2 + S_{zz}^2)}, |S_{zz}| \geq |S_{yy}| \geq |S_{zz}|\right)$ and asymmetry $\left(\eta = \frac{|S_{yy} - S_{xx}|}{S_{zz}}\right)$ of alignment; two angular parameters define the average orientation of the magnetic field relative to the chiral molecular frame (the principal direction, S_{zz}), and a third angular parameter defines the orientation of an orthogonal principal axis (S_{yy}) that specifies the asymmetry of alignment.

In the order tensor approach, order or alignment tensors are determined independently for locally rigid substructures in a target molecule. RNA has natural sub-structures consisting of locally stable A-form helices. The average orientation of helical domains can be obtained by superimposing their order tensor frames (Fig. 1-9)[152, 166, 167]. The analysis insists that helical fragments share, on average, a common view of the magnetic field direction when assembled into a proper structure. However, one cannot distinguish between ‘‘positive’’ and ‘‘negative’’ directions along the principal axes of the order tensor. In other words, RDCs are degenerate to 180° rotations around the principal directions of the order tensor (S_{xx}, S_{yy}, and S_{zz}). This results in 4^{n-1}-fold degeneracy in orienting n fragments, which can often be overcome either by measuring RDCs under at least two different alignments[168, 169] and/or more typically in nucleic acids, by incorporating additional experimental and non-experimental restraints[138, 170, 171]. The two principal order tensor parameters (ϑ and η) obtained for each helix can be compared to obtain information about relative helix motions over submillisecond timescales (Fig. 1-9).

RDCs can also give qualitative information about local and inter-helical motion in the values themselves. It has been shown that the domain with more motions has

uniformly smaller magnitude RDCs. In general, reorientation of bond vectors due to internal motions occurring at submillisecond timescales will lead to dynamical attenuation of the measured RDCs[122]. However, a near-zero RDC value can also arise from static orientation of the inter-nuclear vector relative to the order/alignment tensor, such as at the magic angle relative to the S_{zz} direction of an axially symmetric tensor. However, the observation of attenuated RDCs for many bond vectors in a given residue can, when combined with other structural information, be interpreted as evidence for local flexibility. Hence, RDCs can be used to both solve structures and characterize inter-helical and local dynamics in biomolecules.

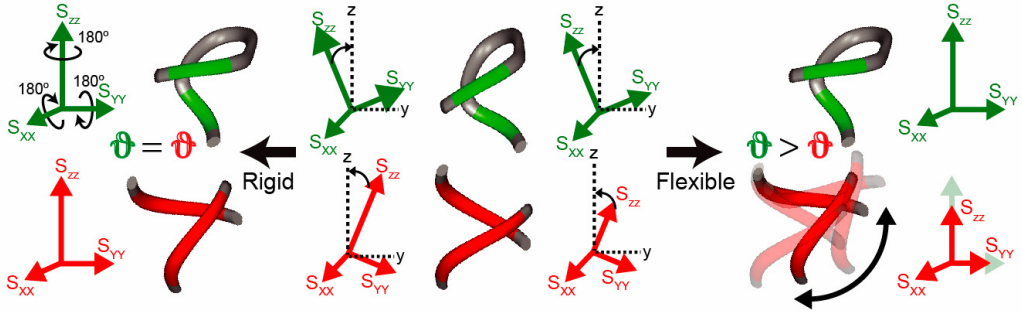

Figure 1-9 Order tensor analysis of RDCs in the determination of the relative orientation and dynamics of A-form helices in RNA. Order tensor frames (S_{xx}, S_{yy}, S_{zz}) are determined for individual helical fragments. Their average relative orientation is determined by superimposing their order tensor frames. Comparison of the degree of order determined for each helix allows characterization of inter-helix motional amplitudes (courtesy of M. Bailor)[172].

Dynamics in biomolecules by NMR

A great advantage of NMR is that it can also be used to site-specifically probe dynamics on a variety of timescales. One of the most widely used NMR approaches for characterizing dynamics on picosecond to nanosecond timescales involves the measurement of spin relaxation data. Three NMR parameters are usually measured for

individual nuclei within a molecule: the longitudinal relaxation rate constant R_1, (also known as spin-lattice relaxation) and the transverse relaxation rate constant R_2 (also known as spin-spin relaxation), and the heteronuclear NOE (cross-relaxation). These three parameters contain information about many of the motions experienced by the nucleus for which they are measured, and report on both the overall and internal motions of the molecule (they don't include translational motion, rotational motion around the bond vector, or a timescale for the motion) .

The imino nitrogens are particularly useful for obtaining dynamical information in nucleic acids since relaxation is primarily dominated by dipolar interactions to the directly bonded protons and to a lesser extent by chemical shift anisotropy (CSA). The two imino nitrogens in RNA are N1 in guanine and N3 in uridine which are hydrogen bonded to cytosine and adenine within helices. The standard NMR experiments for measuring R_1, R_2, and NOE include five parts: preparation, relaxation, frequency labeling, mixing and acquisition. The standard pulse sequences used to measure these parameters are shown in Figure 1-10[173-178]. For a ^{15}N spin bound to a ^{1}H spin the relaxation rate constants of the ^{15}N spin are as follows (eq. 2-4)[179, 180]:

$$R_1 = d^2[J(\omega_H - \omega_N) + 3J(\omega_N) + 6J(\omega_H + \omega_N)] + c^2 J(\omega_N), \quad (2)$$

$$R_2 = (d^2/2)[4J(0) + J(\omega_H - \omega_N) + 3J(\omega_N) + 6J(\omega_H) + 6J(\omega_H + \omega_N)] + (c^2/6)[4J(0) + 3J(\omega_N)], \quad (3)$$

$$NOE = 1 + [\gamma_H/\gamma_N)d^2\{6J(\omega_H + \omega_N) - J(\omega_H - \omega_N\}T_1] \quad (4)$$

in which d^2 is given by $= 0.1\gamma_N{}^2\gamma_H{}^2h^2/(4\pi^2)(1/r_{NH}^6); c^2 = (2/15)\gamma_N{}^2B_o{}^2(\sigma_{II} - \sigma_\perp)^2$; h is Planck's constant; γ_H and γ_N are the ^{1}H and ^{15}N gyromagnetic ratios; r_{NH} is the ^{15}N-H

inter-nuclear distance; the Larmor frequencies of ^{1}H and ^{15}N are given by ω_H and ω_X ; B_o is the magnetic field strength, $\sigma_{//}$ and $\sigma_{\perp}$ are the parallel and perpendicular components of the axially symmetric chemical shift tensor and $J(\omega_i)$ is the spectral density function. The chemical shift tensor is assumed to be axially symmetric and collinear with the NH bond[181].

The spectral density function $J(\omega)$ for a biomolecule in solution depends on the overall motion of the molecule as well as on the internal motions of the ^{1}H-^{15}N bond vector. A model function can be fit to the R_1 and R_2 rates and NOE data with the minimum number of unique motional parameters called the Model-free Lipari-Szabo formalism[182, 183], which assumes no model for the bond vector motion. In this analysis the internal correlation function is modeled by a single exponential function which takes the form

$$C_I(t) = S^2 + (1 - S^2)e^{-t/\tau} \qquad (5)$$

where S^2 is the Lipari-Szabo order parameter for which 0 represents the maximum amplitude of angular reorientation and 1 represents rigidity. The parameter τ is the timescale for the angular reorientation. For long helical elements of RNA, overall tumbling can be modeled as the diffusion of a rod, with the assumption of axial symmetry[184]. Combination of these two models yields a function from which both amplitudes and timescales of motions can be obtained[184]:

$$J(\omega) = \tfrac{2}{5}\sum_{j=0}^{2} A_j \left(\frac{S^2\tau_j}{1+(\omega\tau_j)^2} + \frac{(1-S^2)\tau`_j}{1+(\omega\tau`_j)^2} \right) \qquad (6)$$

where $A_1 = (1.5\cos^2\theta - 0.5)^2$, $A_2 = 3\sin^2\theta\cos^2\theta$, $A_3 = 0.75\sin^4\theta$, $\tau_1^{-1} = 6D_{\perp}$, $\tau_2^{-1} = D_{\parallel} + 5D_{\perp}$, $\tau_3^{-1} = 4D_{\parallel} + 2D_{\perp}$, with $D_{\perp} = D_x = D_y$ and $D_{\parallel} = D_z$, where D_x, D_y, and

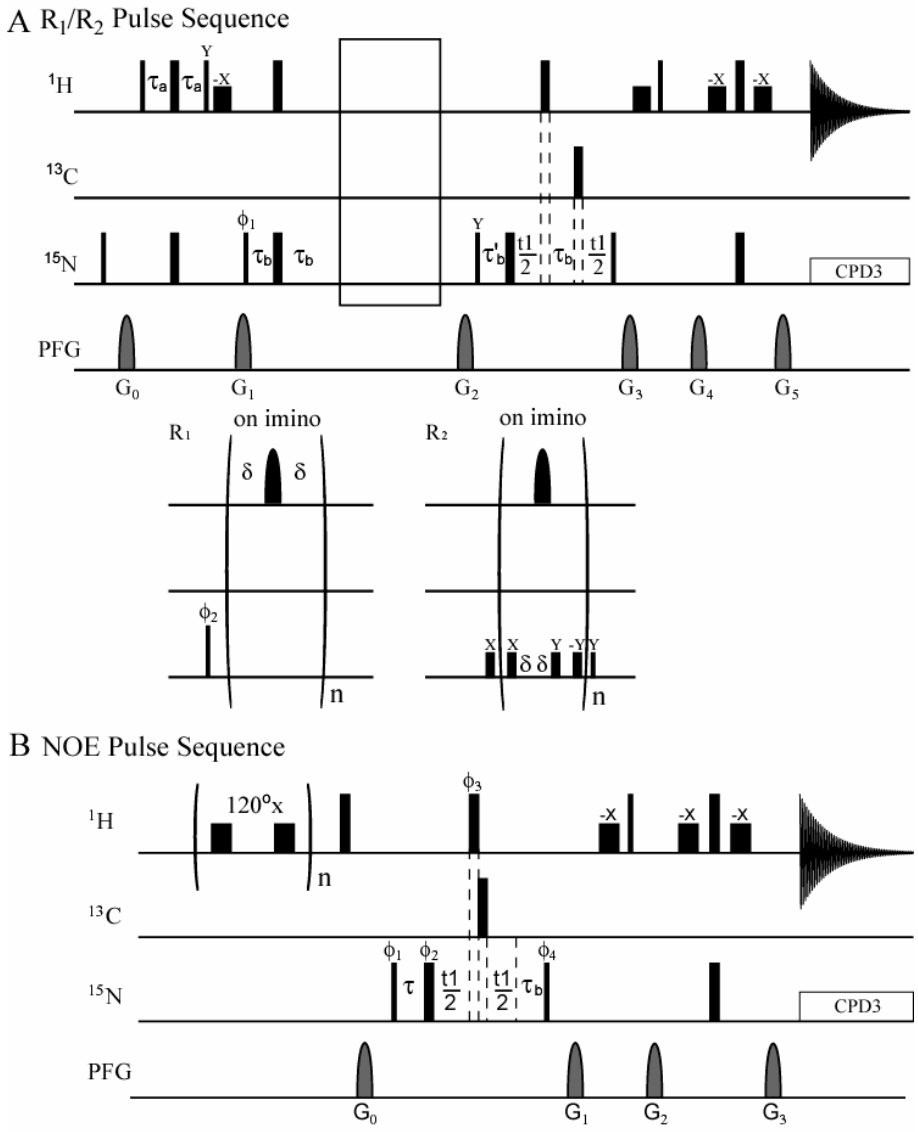

Figure 1-10 Experimental techniques for ^{15}N (A) R_1[174], R_2[175-177](B) {^{1}H}-^{15}N NOE[178] spin relaxation measurements using 2D proton detected pulse sequences[173]. The second dimension is achieved by varying the relaxation period n. The NOE is measured with and without the saturation pulse. Narrow bars are 90° pulses, wide bars are 180° pulses; all pulses are x-phase unless otherwise indicated.

D_z are the principal values of the axially symmetric rotational diffusion tensor, θ is the average angle between the bond vector and principle axis of the rotational diffusion tensor, $\tau'_j = \left(1/\tau_j + 1/\tau_e\right)^{-1}$, with τ_e being the internal motional time constant, and S^2 is the product of two order parameters, S_f^2 and S_s^2, for the amplitudes of fast and slow internal

motions. This function has been expanded to include two internal motional modes[185] by Clore *et al.* with the data fit to a double exponential decay function, from which equations for R_1, R_2, and *NOE*, can be derived and to which experimental data can be fit.

Only a few studies have used spin relaxation to characterize dynamics in RNA. Some fundamental assumptions implicit in the Model-free formalism including the assumption that internal and overall motions are not correlated to one another (the decoupling approximation) has not proven to hold for RNA. In particular, inter-helical motions in RNA can occur on timescales that approach that of overall tumbling (ns)[186], making their spectroscopic contributions difficult to resolve[187, 188]. A new approach has been developed in our laboratory that can help separate internal and overall motions[186]. In this strategy, the terminal domain is elongated by a stretch of Watson-Crick base pairs which slows down the tumbling in solution so it is not on the same timescale as the internal motions. For elongated RNA, the anisotropic diffusion tensor is assumed to be axially symmetric and oriented along the long axis of the extended helix[186].

Probing RNA interactions with metal ions by NMR

In addition to determining the structure and dynamics of macromolecules, another widely used application of NMR is the detection of molecular interactions. Of particular interest for our study is the ability to use NMR to probe interactions between RNA and metal cations.

The most widely used approach to detect RNA-metal interactions uses chemical shifts which are uniquely sensitive to changes in chemical environment and can be affected both by metal-induced structural changes and metal localization. In typical

titration experiments, NMR spectra are recorded as a function of increasing metal concentration. A major problem in this type of analysis is that chemical shift perturbations due to metal localization are very difficult to distinguish from metal-induced structural changes. Some have argued that chemical shift changes on the order of 0.1-0.2 ppm in ^{1}H likely correspond to metal localization, whereas greater shifts might indicate additional changes in structure[189, 190]. Apparent metal ion binding affinities are commonly measured assuming a two-state binding model even though diffusive metals do not obey stoichiometric binding[191]. The generally weak binding affinities and possible involvement of structural and localization effects also make it very difficult to establish how many metals bind a given RNA.

Another NMR approach for probing RNA-metal interactions is to measure paramagnetic relaxation enhancement (PRE) using a paramagnetic metal such as Mn^{2+}. PREs have been used for many years to study metalloproteins and were first used in RNA in 1993 to locate metal binding sites in tRNA[192]. The paramagnetic effect results from unpaired electrons (which have large magnetic moments) with relaxation times varying from 10^{-13}-10^{-8} s depending on the atomic number of the metal and the occupancy of the atomic orbitals[193]. Electron relaxation causes fluctuations in the magnetic fields which results in nuclear relaxation. This fast relaxation causes broadening of NMR resonances in a distant (r) dependent manner ($1/r^6$) in relation to the paramagnetic metal. For these studies, the PRE for ^{1}H transverse magnetization is often measured since the large gyromagnetic ratio of ^{1}H makes it a very sensitive probe. The transverse magnetization rate, Γ_2, is measured more often then the longitudinal PRE (^{1}H- Γ_1) since it is less susceptible to internal motions and cross relaxation[193]. The equation for Γ_2 at high

magnetic fields (^{1}H frequency > 500 MHz) resulting from the dipole-dipole interaction between a nucleus and unpaired electrons with an isotropic *g*-tensor is given by[194-196]:

$$\Gamma_2 = \frac{1}{15}\left(\frac{\mu_o}{4\pi}\right)^2 \gamma_I^2 g^2 \mu_B^2 S(S+1) r^{-6} \left\{ 4\tau_c + \frac{3\tau_c}{1+(\omega_H \tau_c)^2} \right\} \quad (7)$$

where μ_o is the permitivity of a vacuum, γ_I the nuclear gyromagnetic ratio, *g* the electron *g*-factor, μ_B the electron Bohr magneton, *S* the electron spin quantum number, *r* the distance between the paramagnetic center and the observed nucleus, and τ_c the PRE correlation time defined as $\tau_c^{-1} = \tau_r^{-1} + \tau_s^{-1}$; τ_r is the rotational correlation time, τ_s the electron relaxation time, and $\omega_H/2\pi$ the nuclear Larmor frequency. One can assign three zones around the metal: the inner zone where peaks are not detectable, a middle zone where peaks are slightly broadened, and an outer zone which is not affected by the presence of the metal[193]. An advantage of PRE is that it detects primarily metal localization whereas with chemical shift mapping, metal localization cannot be separated from metal induced structural changes.

Another method of detection for RNA bound metals is through inter-molecular NOEs. Metal complexes such as cobalt (III) hexamine ($Co(NH_3)_6^{3+}$) and ammonium NH_4^+ show NOE cross-peaks to nearby protons in the RNA molecule which can be detected by a traditional 2D NOESY experiment[191]. The NOEs are detectable in the t_1 (direct) dimension for $Co(NH_3)_6^{3+}$ at a chemical shift of 3.65 ppm. Cross-peaks are usually observable from $Co(NH_3)_6^{3+}$ to imino, amino, aromatic, H5, and sugar protons in RNA (the last two types are usually more difficult to resolve due to overlap and proximity to the suppressed water peak). The NOE cross-peak intensities can then be divided into groups corresponding to a range of distances. These are then used as input

into traditional NOE structure minimization programs using restrained molecular dynamics such as X-PLOR to calculate structures of the RNA and bound metal[197].

In this thesis, we applied a combination of residual dipolar couplings and motionally decoupled spin relaxation to characterize at atomic resolution the structural plasticity of both P4 (Chapter 2) and a functionally disruptive mutant ($P4_{G8C23}$) from *B. subtilis* (Chapter 4) in the absence and presence of Mg^{2+}. We used chemical shift mapping to identify Mg^{2+} binding sites and their affinities in P4 (Chapter 3). Metal ion substitution was used to determine sites of metal localization in P4 and to distinguish outer sphere and inner sphere metal binding sites (Chapter 3).

References

1. Fire, A.; Xu, S.; Montgomery, M. K.; Kostas, S. A.; Driver, S. E.; Mello, C. C., Potent and specific genetic interference by double-stranded RNA in Caenorhabditis elegans. *Nature* **1998,** *391*, (6669), 806-11.

2. Pace, N. R.; Brown, J. W., Evolutionary perspective on the structure and function of ribonuclease P, a ribozyme. *J. Bacteriol.* **1995,** *177*, (8), 1919-28.

3. Altman, S., RNA enzyme-directed gene therapy. *Proc. Natl. Acad. Sci.* **1993,** *90*, 10898–10900.

4. Frank, D. N.; Harris, M. E.; Pace, N. R., Remodeling active-site structure in a ribozyme: rational design of self-cleaving pre-tRNA-ribonuclease P conjugates. *Biochemistry* **1994,** *33*, 10800–10808.

5. Li, Z.; Deutscher, M. P., Maturation pathways for E. coli tRNA precursors: a random multienzyme process in vivo. *Cell* **1996,** *86*, (3), 503-12.

6. Callahan, C.; Neri-Cortes, D.; Deutscher, M. P., Purification and characterization of the tRNA-processing enzyme RNase BN. *J. Biol. Chem.* **2000,** *275*, (2), 1030-4.

7. Zuo, Y.; Deutscher, M. P., Mechanism of action of RNase T. I. Identification of residues required for catalysis, substrate binding, and dimerization. *J. Biol. Chem.* **2002,** *277*, (51), 50155-9.

8. Zuo, Y.; Deutscher, M. P., Mechanism of action of RNase T. II. A structural and functional model of the enzyme. *J. Biol. Chem.* **2002,** *277*, (51), 50160-4.

9. Zuo, Y.; Deutscher, M. P., The physiological role of RNase T can be explained by its unusual substrate specificity. *J. Biol. Chem.* **2002,** *277*, (33), 29654-61.

10. Zuo, Y.; Zheng, H.; Wang, Y.; Chruszcz, M.; Cymborowski, M.; Skarina, T.; Savchenko, A.; Malhotra, A.; Minor, W., Crystal structure of RNase T, an exoribonuclease involved in tRNA maturation and end turnover. *Structure* **2007,** *15*, (4), 417-28.

11. Li, Z.; Deutscher, M. P., RNase E plays an essential role in the maturation of Escherichia coli tRNA precursors. *RNA* **2002,** *8*, (1), 97-109.

12. Fredrik Pettersson, B. M.; Ardell, D. H.; Kirsebom, L. A., The length of the 5' leader of Escherichia coli tRNA precursors influences bacterial growth. *J. Mol. Biol.* **2005,** *351*, (1), 9-15.

13. Spath, B.; Kirchner, S.; Vogel, A.; Schubert, S.; Meinlschmidt, P.; Aymanns, S.; Nezzar, J.; Marchfelder, A., Analysis of the functional modules of the tRNA 3' endonuclease (tRNase Z). *J. Biol. Chem.* **2005,** *280*, (42), 35440-7.

14. Vogel, A.; Schilling, O.; Spath, B.; Marchfelder, A., The tRNase Z family of proteins: physiological functions, substrate specificity and structural properties. *Biol. Chem.* **2005,** *386*, (12), 1253-64.

15. Ezraty, B.; Dahlgren, B.; Deutscher, M. P., The RNase Z homologue encoded by Escherichia coli elaC gene is RNase BN. *J. Biol. Chem.* **2005,** *280*, (17), 16542-5.

16. Li de la Sierra-Gallay, I.; Mathy, N.; Pellegrini, O.; Condon, C., Structure of the ubiquitous 3' processing enzyme RNase Z bound to transfer RNA. *Nat. Struct. Mol. Biol.* **2006,** *13*, (4), 376-7.

17. Pellegrini, O.; Nezzar, J.; Marchfelder, A.; Putzer, H.; Condon, C., Endonucleolytic processing of CCA-less tRNA precursors by RNase Z in Bacillus subtilis. *EMBO J.* **2003,** *22*, (17), 4534-43.

18. Reich, C.; Olsen, G. J.; Pace, B.; Pace, N. R., Role of the protein moiety of ribonuclease P, a ribonucleoprotein enzyme. *Science* **1988,** *239*, (4836), 178-81.

19. Kole, R.; Baer, M. F.; Stark, B. C.; Altman, S., *E. coli* RNAase P has a required RNA component. *Cell* **1980,** *19*, (4), 881-7.

20. Guerrier-Takada, K.; Gardiner, T.; Marsh, N.; Pace, N. R.; Altman, S., The RNA moiety of ribonuclease P is the catalytic subunit of the enzyme. *Cell* **1983,** *35*, 849-857.

21. Kurz, J. C.; Fierke, C. A., Ribonuclease P: a ribonucleoprotein enzyme. *Curr. Opin. Chem. Biol.* **2000,** *4*, (5), 553-8.

22. Kikovska, E.; Svard, S. G.; Kirsebom, L. A., Eukaryotic RNase P RNA mediates cleavage in the absence of protein. *Proc. Natl. Acad. Sci. USA* **2007,** *104*, (7), 2062-7.

23. Mildvan, A. S., Mechanisms of signaling and related enzymes. *Proteins* **1997,** *29*, (4), 401-16.

24. Steitz, T. A.; Steitz, J. A., A general two-metal-ion mechanism for catalytic RNA. *Proc. Natl. Acad. Sci. USA* **1993,** *90*, (14), 6498-502.

25. Kazantsev, A. V.; Pace, N. R., Identification by modification-interference of purine N-7 and ribose 2'-OH groups critical for catalysis by bacterial ribonuclease P. *RNA* **1998,** *4*, 937-47.

26. Smith, D.; Pace, N. R., Multiple magnesium ions in the ribonuclease P reaction mechanism. *Biochemistry* **1993,** *32*, (20), 5273-81.

27. Beebe, J. A.; Kurz, J. C.; Fierke, C. A., Magnesium ions are required by *Bacillus subtilis* ribonuclease P for both binding and cleaving precursor $tRNA^{Asp}$. *Biochemistry* **1996,** *35*, 10493-10505.

28. Warnecke, J. M.; Furste, J. P.; Hardt, W. D.; Erdmann, V. A.; Hartmann, R. K., Ribonuclease P (RNase P) RNA is converted to a Cd^{2+}-ribozyme by a single R_p-phosphorothioate modification in the precursor tRNA at the RNase P cleavage site. *Proc. Natl. Acad. Sci. USA* **1996,** *93*, (17), 8924-8.

29. Warnecke, J. M.; Held, R.; Busch, S.; Hartmann, R. K., Role of metal ions in the hydrolysis reaction catalyzed by RNase P RNA from Bacillus subtilis. *J. Mol. Biol.* **1999,** *290*, (2), 433-45.

30. Hardt, W. D.; Schlegl, J.; Erdmann, V. A.; Hartmann, R. K., Gel retardation analysis of E. coli M1 RNA-tRNA complexes. *Nucleic Acids Res.* **1993,** *21*, (15), 3521-7.

31. Christian, E. L.; Smith, K. M. J.; Perera, N.; Harris, M. E., The P4 metal binding site in RNase P RNA affects active site metal affinity through substrate positioning. *RNA* **2006,** *12*, 1463-7.

32. Pomeranz Krummel, D. A.; Altman, S., Multiple binding modes of substrate to the catalytic RNA subunit of RNase P from Escherichia coli. *RNA* **1999,** *5*, (8), 1021-33.

33. Hardt, W. D.; Warnecke, J. M.; Erdmann, V. A.; Hartmann, R. K., Rp-phosphorothioate modifications in RNase P RNA that interfere with tRNA binding. *The EMBO J.* **1995,** *14*, (12), 2935-2944.

34. Harris, M. E.; Pace, N. R., Identification of phosphates involved in catalysis by the ribozyme RNase P RNA. *RNA* **1995,** *1*, (2), 210-8.

35. Crary, S. M.; Kurz, J. C.; Fierke, C. A., Specific phosphorothioate substitutions probe the active site of *Bacillus subtilis* ribonuclease P. *RNA* **2002,** *8*, (7), 933-47.

36. Chen, J. L.; Pace, N. R., Identification of the universally conserved core of ribonuclease P RNA. *RNA* **1997,** *3*, (6), 557-60.

37. Kazantsev, A. V.; Krivenko, A. A.; Harrington, D. J.; Holbrook, S. R.; Adams, P. D.; Pace, N. R., Crystal structure of a bacterial ribonuclease P RNA. *Proc. Natl. Acad. Sci. USA* **2005,** *102*, (38), 13392-13397.

38. Hardt, W. D.; Erdmann, V. A.; Hartmann, R. K., Rp-deoxy-phosphorothioate modification interference experiments identify 2'-OH groups in RNase P RNA that are crucial to tRNA binding. *RNA* **1996,** *2*, 1189-1198.

39. Siew, D.; Zahler, N. H.; Cassano, A. G.; Strobel, S. A.; Harris, M. E., Identification of adenosine functional groups involved in substrate binding by the ribonuclease P ribozyme. *Biochemistry* **1999,** *38*, 1873-83.

40. Kaye, N. M.; Christian, E. L.; Harris, M. E., NAIM and site-specific functional group modification analysis of RNase P RNA: Magnesium dependent structure within the conserved P1-P4 multihelix junction contributes to catalysis. *Biochemistry* **2002,** *41*, 4533-4545.

41. Heide, C.; Pfeiffer, T.; Nolan, J. M.; Hartmann, R. K., Guanosine 2-NH_2 groups of *Escherichia coli* RNase P RNA involved in intramolecular tertiary contacts and direct interactions with tRNA. *RNA* **1999,** *5*, 102-116.

42. Christian, E. L.; Kaye, N. M.; Harris, M. E., Helix P4 is a divalent metal ion binding site in the conserved core of the ribonuclease P ribozyme. *RNA* **2000,** *6*, 511-519.

43. Schmitz, M.; Tinoco, I. J., Solution structure and metal-ion binding of the P4 element from bacterial RNase P RNA. *RNA* **2000,** *6*, 1212-1225.

44. Frank, D. N.; Pace, N. R., In vitro selection for altered divalent metal specificity in the RNase P RNA. *Proc. Natl. Acad. Sci. USA* **1997,** *94*, (26), 14355-60.

45. Chen, J. L.; Pace, N. R., Identification of the universally conserved core of the ribonuclease P RNA. *RNA* **1997,** *3*, 557-560.

46. Kaye, N. M.; Zahler, N. H.; Christian, E. L.; Harris, M. E., Conservation of helical structure contributes to functional metal ion interactions in the catalytic domain of ribonuclease P RNA. *J. Mol. Biol.* **2002,** *324*, (3), 429-42.

47. Schmitz, M., Change of RNase P RNA function by single base mutation correlates with perturbation of metal ion binding in P4 as determined by NMR spectroscopy. *Nucleic Acids Res.* **2004,** *32*, 6358-6366.

48. Tsai, H. Y.; Masquida, B.; Biswas, R.; Westhof, E.; Gopalan, V., Molecular modeling of the three-dimensional structure of the bacterial RNase P holoenzyme. *J. Mol. Biol.* **2003,** *325*, (4), 661-75.

49. Williamson, J. R., Induced fit in RNA-protein recognition. *Nat. Struct. Biol.* **2000,** *7*, 834-7.

50. Leulliot, N.; Varani, G., Current topics in RNA-protein recognition: control of specificity and biological function through induced fit and conformational capture. *Biochemistry* **2001,** *40*, 7947-7956.

51. Al-Hashimi, H. M., Dynamics-based amplification of RNA function and its characterization by using NMR spectroscopy. *ChemBioChem* **2005,** *6*, 1506-1519.

52. Krasilnikov, A. S.; Yang, X.; Pan, T.; Mondragón, A., Crystal structure of the specificity domain of ribonuclease P. *Nature* **2003,** *421*, (6924), 760-4.

53. Krasilnikov, A. S.; Xiao, Y.; Pan, T.; Mondragon, A., Basis for structural diversity in homologous RNAs. *Science* **2004,** *306*, (5693), 104-7.

54. Torres-Larios, A.; Swinger, K. K.; Krasilnikov, A. S.; Pan, T.; Mondragón, A., Crystal structure of the RNA component of bacterial ribonuclease P. *Nature* **2005,** *437*, (7058), 584-7.

55. Christian, E. L.; McPheeters, D. S.; Harris, M. E., Identification of individual nucleotides in the bacterial ribonuclease P ribozyme adjacent to the pre-tRNA cleavage site by short-range photocrosslinking. *Biochemistry* **1998,** *37*, 17618-17628.

56. Torres-Larios, A.; Swinger, K. K.; Pan, T.; Mondragon, A., Structure of ribonuclease P—a universal ribozyme. *Curr. Opin. Struct. Biol.* **2006,** *16*, 327-335.

57. Massire, C.; Jaeger, L.; Westhof, E., Derivation of the three-dimensional architecture of bacterial ribonuclease P RNAs from comparative sequence analysis. *J. Mol. Biol.* **1998,** *279*, (4), 773-93.

58. Chen, J. L.; Nolan, J. M.; Harris, M. E.; Pace, N. R., Comparative photocross-linking analysis of the tertiary structures of *Escherichia coli* and *Bacillus subtilis* RNase P RNAs. *EMBO J.* **1998,** *17*, 1515-1525.

59. Stams, T.; Niranjanakumari, S.; Fierke, C. A.; Christianson, D. W., Ribonuclease P protein structure: evolutionary origins in the translational apparatus. *Science* **1998,** *280*, (5364), 752-5.

60. Kazantsev, A. V.; Krivenko, A. A.; Harrington, D. J.; Carter, R. J.; Holbrook, S. R.; Adams, P. D.; Pace, N. R., High resolution structure of RNase P protein from *Thermotoga maritima*. *Proc. Natl. Acad. Sci.* **2003,** *100*, (13), 7497-7502.

61. Spitzfaden, C.; Nicholson, N.; Jones, J. J.; Guth, S.; Lehr, R.; Prescott, C. D.; Hegg, L. A.; Eggleston, D. S., The structure of ribonuclease P protein from Staphylococcus aureus reveals a unique binding site for single-stranded RNA. *J. Mol. Biol.* **2000,** *295*, (1), 105-15.

62. Quigley, G. J.; Seeman, N. C.; Wang, A. H.; Suddath, F. L.; Rich, A., Yeast phenylalanine transfer RNA: atomic coordinates and torsion angles. *Nucleic Acids Res.* **1975,** *2*, (12), 2329-41.

63. Niranjanakumari, S.; Day-Storms, J. J.; Ahmed, M.; Hsieh, J.; Zahler, N. H.; Venters, R. A.; Fierke, C. A., Probing the architecture of the B. subtilis RNase P holoenzyme active site by cross-linking and affinity cleavage. *RNA* **2007,** *13*, (4), 521-35.

64. Hammes, G. G., Multiple conformational changes in enzyme catalysis. *Biochemistry* **2002,** *41*, (26), 8221-8.

65. Anderson, C. M.; Zucker, F. H.; Steitz, T. A., Space-filling models of kinase clefts and conformation changes. *Science* **1979,** *204*, (4391), 375-80.

66. Walter, N. G.; Hampel, K. J.; Brown, K. M.; Burke, J. M., Tertiary structure formation in the hairpin ribozyme monitored by fluorescence resonance energy transfer. *EMBO J.* **1998,** *17*, (8), 2378-91.

67. Eisenmesser, E. Z.; Bosco, D. A.; Akke, M.; Kern, D., Enzyme dynamics during catalysis. *Science* **2002,** *295*, 1520-1523.

68. Talbot, S. J.; Alman, S., Kinetic and thermodynamic analysis of RNA-protein interactions in the RNase P holoenzyme from *Escherichia coli*. *Biochemistry* **1994,** *33*, (6), 1406-11.

69. Buck, A. H.; Kazantsev, A. V.; Dalby, A. B.; Pace, N. R., Structural perspective on the activation of RNase P RNA by protein. *Nat. Struct. Biol. & Mol. Biol.* **2005,** *12*, 958-964.

70. Pomeranz Krummel, D. A.; Altman, S., Multiple binding modes of substrate to the catalytic RNA subunit of the RNase P from *Escherichia coli*. *RNA* **1999,** *5*, 1021-1033.

71. Komatsu, H.; Iwasawa, N.; Citterio, D.; Suzuki, Y.; Kubota, T.; Tokuno, K.; Kitamura, Y.; Oka, K.; Suzuki, K., Design and synthesis of highly sensitive and selective fluorescein-derived magnesium fluorescent probes and application to intracellular 3D Mg2+ imaging. *J. Am. Chem. Soc.* **2004,** *126*, (50), 16353-60.

72. Onoa, B.; Tinoco, I., Jr., RNA folding and unfolding. *Curr. Opin. Struct. Biol.* **2004,** *14*, (3), 374-9.

73. Record Jr., M. T.; Richey, B., *Physical chemical analysis of biopolymer self-assembly interactions. In ACS sourcebook for physical chemistry instructors (ed. E.T. Lippincott)*. American Chemical Society: Washington, D.C., 1988.

74. Ferre-D`Amare, A. R.; Zhou, K.; Doudna, J. A., Crystal structure of a hepatitis delta virus ribozyme. *Nature* **1998,** *395*, 567-574.

75. Stahley, M. R.; Strobel, S. A., Structural evidence for a two-metal-ion mechanism of group I intron splicing. *Science* **2005,** *309*, 1587-1590.

76. Ban, N.; Nissen, P.; Hansen, J.; Moore, P. B.; Steitz, T. A., The complete atomic structure of the large ribosomal subunit at 2.4A resolution. *Science* **2000,** *289*, (905-920).

77. Correll, C. C.; Freeborn, B.; Moore, P. B.; Steitz, T. A., Metals, motifs, and recognition in the crystal structure of a 5S rRNA domain. *Cell* **1997,** *91*, (5), 705-12.

78. Cate, J. H.; Gooding, A. R.; Podell, E.; Zhou, K.; Golden, B. L.; Kundrot, C. E.; Cech, T. R.; Doudna, J. A., Crystal structure of a group I ribozyme domain: principles of RNA packing. *Science* **1996,** *273*, (5282), 1678-85.

79. Wedekind, J. E.; McKay, D. B., Crystal structure of the leadzyme at 1.8Å resolution: metal ion binding and the implications for catalytic mechanism and allo site ion regulation. *Biochemistry* **2003,** *42*, 9554-9563.

80. Hampel, A.; Cowan, J. A., A unique mechanism for RNA catalysis: the role of metal cofactors in hairpin ribozyme cleavage. *Chem. Biol.* **1997,** *4*, (7), 513-7.

81. Murray, J. B.; Seyhan, A. A.; Walter, N. G.; Burke, J. M.; Scott, W. G., The hammerhead, hairpin and VS ribozymes are catalytically proficient in monovalent cations alone. *Chem. Biol.* **1998,** *5*, (10), 587-95.

82. Young, K. J.; Gill, F.; Grasby, J. A., Metal ions play a passive role in the hairpin ribozyme catalysed reaction. *Nucleic Acids Res.* **1997,** *25*, (19), 3760-6.

83. Lebruska, L. L.; Kuzmine, II; Fedor, M. J., Rescue of an abasic hairpin ribozyme by cationic nucleobases: evidence for a novel mechanism of RNA catalysis. *Chem. Biol.* **2002,** *9*, (4), 465-73.

84. O'Rear, J. L.; Wang, S.; Feig, A. L.; Beigelman, L.; Uhlenbeck, O. C.; Herschlag, D., Comparison of the hammerhead cleavage reactions stimulated by monovalent and divalent cations. *RNA* **2001,** *7*, 537-545.

85. Doudna, J. A.; Cech, T. R., The chemical repertoire of natural ribozymes. *Nature* **2002,** *418*, 222-228.

86. DeRose, V. J., Two Decades of RNA Catalysis. *Chem. and Biol.* **2002,** *9*, 961-969.

87. Fedor, M. J.; Westhof, E., Ribozymes: the first 20 years. *Mol. Cell.* **2002,** *10*, (4), 703-4.

88. Pyle, A. M., Metal ions in the structure and function of RNA. *J. Biol. Inorg. Chem.* **2002,** *7*, (7-8), 679-90.

89. Sigel, R. K.; Vaidya, A.; Pyle, A. M., Metal ion binding sites in a group II intron core. *Nat. Struct. Biol.* **2000,** *7*, (12), 1111-6.

90. Misra, V. K.; Draper, D. E., On the role of magnesium ions in RNA stability. *Biopolymers* **1998,** *48*, (2-3), 113-35.

91. Honig, B.; Nicholls, A., Classical electrostatics in biology and chemistry. *Science* **1995,** *268*, 1144–49.

92. Chen, S. W.; Honig, B., Monovalent and divalent salt effects on electrostatic free energies defined by the nonlinear Poisson-Boltzmann equation: application to DNA binding reactions. *J. Phys. Chem.* **1997,** *101*, 9113–18.

93. Draper, D. E.; Grilley, D.; Soto, A. M., Ions and RNA folding. *Annu. Rev. Biophys. Biomol. Struct.* **2005,** *34*, 221-43.

94. Richens, D. T., *The Chemistry of Aqua Ions: Synthesis, Structure, and Reactivity: A Tour Through the Periodic Table of Elements*. J. Wiley: New York, 1997.

95. Zivarts, M.; Liu, Y.; Breaker, R. R., Engineered allosteric ribozymes that respond to specific divalent metal ions. *Nucleic Acids Res.* **2005,** *33*, (2), 622-631.

96. Draper, D. E., A guide to ions and RNA structure. *RNA* **2004,** *10*, 335-343.

97. Cowan, J. A., Metallobiochemistry of RNA. Co(NH3)6(3+) as a probe for Mg2+(aq) binding sites. *J. Inorg. Biochem.* **1993,** *49*, (3), 171-5.

98. Nowakowski, J.; Shim, P. J.; Stout, C. D.; Joyce, G. F., Alternative conformations of a nucleic acid four-way junction. *J. Mol. Biol.* **2000,** *300*, (1), 93-102.

99. Wild, K.; Weichenrieder, O.; Leonard, G. A.; Cusack, S., The 2 A structure of helix 6 of the human signal recognition particle RNA. *Structure* **1999,** *7*, (11), 1345-52.

100. Guerrier-Takada, C.; Haydock, K.; Allen, L.; Altman, S., Metal ion requirements and other aspects of the reaction catalyzed by M1 RNA, the RNA subunit of ribonuclease P from *Escherichia coli*. *Biochemistry* **1986,** *25*, 1509-15.

101. Pan, T., Higher order folding and domain analysis of the ribozyme from Bacillus subtilis ribonuclease P. *Biochemistry* **1995,** *34*, (3), 902-9.

102. Kazakov, S.; Altman, S., Site-specific cleavage by metal ion cofactors and inhibitors of M1 RNA, the catalytic subunit of RNase P from *Escherichia coli*. *Proc. Natl. Acad. Sci. USA* **1991,** *88*, (20), 9193-7.

103. Smith, D.; Burgin, A. B.; Haas, E. S.; Pace, N. R., Influence of metal ions on the ribonuclease P reaction. *J. Biol. Chem.* **1992,** *267*, (4), 2429-2436.

104. Kufel, J.; Kirsebom, L. A., Cleavage site selection by M1 RNA the catalytic subunit of *Escherichia coli* RNase P, is influenced by pH. *J. Mol. Biol.* **1994,** *244*, (5), 511-21.

105. Kufel, J.; Kirsebom, L. A., Different cleavage sites are aligned differently in the active site of M1 RNA, the catalytic subunit of *Escherichia coli* RNase P. *Proc. Natl. Acad. Sci. USA* **1996,** *93*, (12), 6085-90.

106. Kufel, J.; Kirsebom, L. A., Residues in *Escherichia coli* RNase P RNA important for cleavage site selection and divalent metal ion binding. *J. Mol. Biol.* **1996,** *263*, (5), 685-98.

107. Chen, Y.; Li, X.; Gegenheimer, P., Ribonuclease P catalysis requires Mg^{2+} coordinated to the pro-R_P oxygen of the scissile bond. *Biochemistry* **1997,** *36*, (9), 2425-38.

108. Brannvall, M.; Mikkelsen, N. E.; Kirsebom, L. A., Monitoring the structure of *Escherichia coli* RNase P RNA in the presence of various divalent metal ions. *Nucleic Acids Res.* **2000,** *29*, (7), 1426-1432.

109. Cuzic, S.; Hartmann, R. K., Studies on *Escherichia coli* RNase P RNA with Zn^{2+} as the catalytic cofactor. *Nucleic Acids Res.* **2005,** *33*, 2464-2474.

110. Purcell, E. M.; Torrey, H. C.; Pound, R. V., *Phys. Rev.* **1946,** *69*, 37-38.

111. Bloch, F.; Hansen, W. W.; Packard, M., *Phys. Rev.* **1946,** *69*, 127.

112. Cavanagh, J.; Fairbrother, W. J.; Palmer, A. G. I.; Rance, M.; Skelton, N. J., *Protein NMR Spectroscopy: Principles and Practice Section Edition*. Elsevier: New York, 2007.

113. Ernst, R. R.; Anderson, W. A., *Rev. Sci. Instrum.* **1966,** *37*, 93-102.

114. Jeener, J. Ampere Summer School. Yugoslavia, Basko Polje, 1971.

115. Jeener, J., NMR and More. In Honour of Anatole Abragam. In M. Goldman, M. P., 'Ed."; Les Editions de Physique: Les Ulis, France, 1994; pp 1-379.

116. Wijmenga, S. S.; van Buuren, B. N. M., The use of NMR methods for conformational studies of nucleic acids. *Prog. Nuc. Magn. Reson. Spec.* **1998,** *32*, 287-387.

117. Rao, B. D., Nuclear magnetic resonance line-shape analysis and determination of exchange rates. *Methods Enzymol.* **1989,** *176*, 279-311.

118. Led, J. J.; Gesmar, H.; Abildgaard, F., Applicability of magnetization transfer nuclear magnetic resonance to study chemical exchange reactions. *Methods Enzymol.* **1989,** *176*, 311-29.

119. Gueron, M.; Leroy, J. L., Studies of base pair kinetics by NMR measurement of proton exchange. *Methods Enzymol.* **1995,** *261*, 383-413.

120. Palmer, A. G., NMR characterization of the dynamics of biomacromolecules. *Chem. Rev.* **2004,** *104*, 3623-3640.

121. Kay, L. E., Protein dynamics from NMR. *Nat. Struct. Biol.* **1998,** *5 Suppl*, 513-7.

122. Tolman, J. R.; Flanagan, J. M.; Kennedy, M. A.; Prestegard, J. H., NMR evidence for slow collective motions in cyanometmyoglobin. *Nat. Struct. Biol.* **1997,** *4*, (4), 292-297.

123. Furtig, B.; Richter, C.; Wohnert, J.; Schwalbe, H., NMR spectroscopy of RNA. *ChemBioChem* **2003,** *4*, (10), 936-62.

124. Wüthrich, K., *NMR of Proteins and Nucleic Acids*. John Wiley and Sons: New York, 1986.

125. Pardi, A.; Walker, R.; Rapoport, H.; Wider, G.; Wuthrich, K., Sequential assignments for the 1H and 31P atoms in the backbone of oligonucleotides by two-dimensional nuclear magnetic resonance. *J. Am. Chem. Soc.* **1983,** *105*, 1652-1653.

126. Kellog, G. W.; Schweitzer, B. I., Two- and three-dimensional 31P-driven NMR procedures for complete assignment of backbone resonances in oligodeoxyribonucleotides. *J. Biomol. NMR* **1993,** *3*, 577-595.

127. Kellogg, G. W., Proton-detected hetero-TOCSY experiments with application to nucleic acids. *J. Magn. Reson.* **1992,** *98*, 176-182.

128. Sklenar, V.; Rejante, M. R.; Peterson, R. D.; Wang, E.; Feigon, J., Two-dimensional triple-resonance HCNCH experiment for direct correlation of ribose H1' and base H8, H6 protons in 13C,15N-labeled RNA oligonucleotides. *J. Am. Chem. Soc.* **1993,** *115*, 12181-12182.

129. Sklenar, V.; Peterson, R. D.; Rejante, M. R.; Feigon, J., Two- and three-dimensional HCN experiments for correlating base and sugar resonances in $^{15}N,^{13}C$-labeled RNA oligonucleotides. *J. Biomol. NMR* **1993,** *3*, 721-7.

130. Legault, P.; Farmer, B. T.; Mueller, L.; Pardi, A., Through-Bond Correlation of Adenine Protons in a 13C-Labeled Ribozyme. *J. Am. Chem. Soc.* **1994,** *116*, 2203-2204.

131. Sklenar, V.; Dieckmann, T.; Butcher, S. E.; Feigon, J., Through-bond correlation of imino and aromatic resonances in 13C-, 15N-labeled RNA via heteronuclear TOCSY. *J. Biomol. NMR* **1996,** *7*, (1), 83-7.

132. Wuthrich, K., NMR studies of structure and function of biological macromolecules (Nobel lecture). *J. Biomol. NMR* **2003,** *27*, 13-39.

133. MacDonald, D.; Lu, P., Residual dipolar couplings in nucleic acid structure determination. *Curr. Opin. Struct. Biol.* **2002,** *12*, (3), 337-43.

134. Mooren, M. M.; Wijmenga, S. S.; van der Marel, G. A.; van Boom, J. H.; Hilbers, C. W., The solution structure of the circular trinucleotide cr(GpGpGp) determined by NMR and molecular mechanics calculation. *Nucleic Acids Res.* **1994,** *22*, (13), 2658-66.

135. Lohman, J. A. B.; MacLean, C., Alignment effects on high resolution NMR spectra, induced by the magnetic field. *Chemical Physics* **1978,** *35*, 269-274.

136. Prestegard, J. H.; Tolman, J. R.; Al-Hashimi, H. M.; Andrec, M., Protein structure and dynamics from field induced residual dipolar couplings. In *Biological Magnetic Resonance*, Krishna, N. R.; Berliner, L. J., 'Eds.' Plenum: New York, 1999; 'Vol.' 17, pp 311-355.

137. Prestegard, J. H.; Al-Hashimi, H. M.; Tolman, J. R., NMR structures of biomolecules using field oriented media and residual dipolar couplings. *Quart. Rev. Biophys.* **2000,** *33*, (4), 371-424.

138. Mollova, E. T.; Hansen, M. R.; Pardi, A., Global structure of RNA determined with residual dipolar couplings. *J. Am. Chem. Soc.* **2000,** *122*, (46), 11561-11562.

139. Ottiger, M.; Bax, A., Determination of relative N-H-N N-C ', C-alpha-C ', andC(alpha)-H-alpha effective bond lengths in a protein by NMR in a dilute liquid crystalline phase. *J. Am. Chem. Soc.* **1998,** *120*, (47), 12334-12341.

140. Tjandra, N.; Bax, A., Direct measurement of distances and angles in biomolecules by NMR in a dilute liquid crystalline medium. *Science* **1997,** *278*, (5340), 1111-1114.

141. Hansen, M. R.; Hanson, P.; Pardi, A., Filamentous bacteriophage for aligning RNA, DNA, and proteins for measurement of nuclear magnetic resonance dipolar coupling interactions. *Methods in Enzymol.* **2000,** *317*, 220-240.

142. Clore, G. M.; Starich, M. R.; Gronenborn, A. M., Measurement of residual dipolar couplings of macromolecules aligned in the nematic phase of a colloidal suspension of rod- shaped viruses. *J. Am. Chem. Soc.* **1998,** *120*, (40), 10571-10572.

143. Hansen, M. R.; Mueller, L.; Pardi, A., Tunable alignment of macromolecules by filamentous phage yields dipolar coupling interactions. *Nat. Struct. Biol.* **1998,** *5*, (12), 1065-1074.

144. Koenig, B. W.; Hu, J. S.; Ottiger, M.; Bose, S.; Hendler, R. W.; Bax, A., NMR measurement of dipolar couplings in proteins aligned by transient binding to purple membrane fragments. *J. Am. Chem. Soc.* **1999,** *121*, (6), 1385-1386.

145. Sass, J.; Cordier, F.; Hoffmann, A.; Cousin, A.; Omichinski, J. G.; Lowen, H.; Grzesiek, S., Purple membrane induced alignment of biological macromolecules in the magnetic field. *J. Am. Chem. Soc.* **1999,** *121*, (10), 2047-2055.

146. Sass, H. J.; Musco, G.; Stahl, S. J.; Wingfield, P. T.; Grzesiek, S., Solution NMR of proteins within polyacrylamide gels: Diffusional properties and residual alignment by mechanical stress or embedding of oriented purple membranes. *J. Biomol. NMR* **2000,** *18*, (4), 303-309.

147. Tycko, R.; Blanco, F. J.; Ishii, Y., Alignment of biopolymers in strained gels: A new way to create detectable dipole-dipole couplings in high resolution biomolecular NMR. *J. Am. Chem. Soc.* **2000,** *122*, 9340-9341.

148. Getz, M.; Sun, X.; Casiano-Negroni, A.; Zhang, Q.; Al-Hashimi, H. M., NMR studies of RNA dynamics and structural plasticity using NMR residual dipolar couplings. *Biopolymers* **2007,** *86*, 384-402.

149. Bewley, C. A.; Gustafson, K. R.; Boyd, M. R.; Covell, D. G.; Bax, A.; Clore, G. M.; Gronenborn, A. M., Solution structure of cyanovirin-N, a potent HIV-inactivating protein. *Nat. Struct. Biol.* **1998,** *5*, (7), 571-578.

150. Clore, G. M.; Starich, M. R.; Bewley, C. A.; Cai, M. L.; Kuszewski, J., Impact of residual dipolar couplings on the accuracy of NMR structures determined from a minimal number of NOE restraints. *J. Am. Chem. Soc.* **1999,** *121*, (27), 6513-6514.

151. Wang, Y. X.; Neamati, N.; Jacob, J.; Palmer, I.; Stahl, S. J.; Kaufman, J. D.; Huang, P. L.; Winslow, H. E.; Pommier, Y.; Wingfield, P. T.; Lee-Huang, S.; Bax, A.; Torchia, D. A., Solution structure of anti-HIV-1 and anti-tumor protein MAP30: Structural insights into its multiple functions. *Cell* **1999,** *99*, (4), 433-442.

152. Al-Hashimi, H. M.; Gosser, Y.; Gorin, A.; Hu, W.; Majumdar, A.; Patel, D. J., Concerted motions in HIV-1 TAR RNA may allow access to bound state conformations: RNA dynamics from NMR residual dipolar couplings. *J. Mol. Biol.* **2002,** *315*, (2), 95-102.

153. Boisbouvier, J.; Bryce, D. L.; O'Neil-Cabello, E.; Nikonowicz, E. P.; Bax, A., Resolution-optimized NMR measurement of (1)D(CH), (1)D(CC) and (2)D(CH) residual dipolar couplings in nucleic acid bases. *J. Biomol. NMR* **2004,** *30*, (3), 287-301.

154. Miclet, E.; O'Neil-Cabello, E.; Nikonowicz, E. P.; Live, D.; Bax, A., 1H-1H dipolar couplings provide a unique probe of RNA backbone structure. *J. Am. Chem. Soc.* **2003,** *125*, (51), 15740-1.

155. Miclet, E.; Boisbouvier, J.; Bax, A., Measurement of eight scalar and dipolar couplings for methine-methylene pairs in proteins and nucleic acids. *J. Biomol. NMR* **2005,** *31*, (3), 201-16.

156. O'Neil-Cabello, E.; Bryce, D. L.; Nikonowicz, E. P.; Bax, A., Measurement of five dipolar couplings from a single 3D NMR multiplet applied to the study of RNA dynamics. *J. Am. Chem. Soc.* **2004,** *126*, (1), 66-7.

157. Schwalbe, H.; Marino, J. P.; King, G. C.; Wechselberger, R.; Bermel, W.; Griesinger, C., Determination of a complete set of coupling constants in 13C-labeled oligonucleotides. *J. Biomol. NMR* **1994,** *4*, (5), 631-44.

158. Ottiger, M.; Delaglio, F.; Bax, A., Measurement of J and dipolar couplings from simplified two- dimensional NMR spectra. *J. Magn.Reson.* **1998,** *131*, (2), 373-378.

159. Vallurupalli, P.; Moor, P. B., Measurement of H2'-C2' and H3'-C3' dipolar couplings in RNA molecules. *J. Biomol. NMR* **2002,** *24*, (1), 63-6.

160. Yan, J.; Corpora, T.; Pradhan, P.; clore, J. H., MQ-hCN-based pulse sequences for the measurement of 13C1'-1H1', 13C1'-15N, 1H1'-15N, 13C1'-13C2', 1H1'-13C2',13C6/8-1H6/8, 13C6/8-15N, 1H6/8-15N, 13C6-13C5, 1H6-13C5 dipolar couplings in 13C, 15N-labeled DNA (and RNA). *J. Biomol. NMR* **2002,** *22*, (1), 9-20.

161. Zidek, L.; Wu, H.; Feigon, J.; Sklenar, V., Measurement of small scalar and dipolar couplings in purine and pyrimidine bases. *J. Biomol. NMR* **2001,** *21*, (2), 153-60.

162. Brutscher, B.; Boisbouvier, J.; Pardi, A.; Marion, D.; Simorre, J. P., Improved sensitivity and resolution in H-1-C-13 NMR experiments of RNA. *J. Am. Chem. Soc.* **1998,** *120*, (46), 11845-11851.

163. Jaroniec, C. P.; Boisbouvier, J.; Tworowska, I.; Nikonowicz, E. P.; Bax, A., Accurate measurement of 15N-13C residual dipolar couplings in nucleic acids. *J. Biomol. NMR* **2005,** *31*, (3), 231-41.

164. Saupe, A., Recent results in the field of liquid crystals. *Angew. Chem., Int. Ed. Engl.* **1968,** *7*, 97-112.

165. Tolman, J. R.; Al-Hashimi, H. M., NMR Studies of Biomolecular Dynamics and Structural Plasticity Using Residual Dipolar Couplings. In *Ann. Rep. NMR Spec.*, (Edt), G. A. W., 'Ed."; Academic Press: 2003; 'Vol.' In Press.

166. Tolman, J. R.; Al-Hashimi, H. M.; Kay, L. E.; Prestegard, J. H., Structural and dynamic analysis of residual dipolar coupling data for proteins. *J. Am. Chem. Soc.* **2001,** *123*, (7), 1416-1424.

167. Losonczi, J. A.; Andrec, M.; Fischer, M. W.; Prestegard, J. H., Order matrix analysis of residual dipolar couplings using singular value decomposition. *J. Magn. Reson.* **1999,** *138*, 334-342.

168. Al-Hashimi, H. M.; Valafar, H.; Terrell, M.; Zartler, E. R.; Eidsness, M. K.; Prestegard, J. H., Variation of molecular alignment as a means of resolving orientational ambiguities in protein structures from dipolar couplings. *J. Magn. Reson.* **2000,** *143*, (2), 402-6.

169. Ramirez, B. E.; Bax, A., Modulation of the alignment tensor of macromolecules dissolved in a dilute liquid crystalline medium. *J. Am. Chem. Soc.***1998,** *120*, (35), 9106-9107.

170. Al-Hashimi, H. M.; Gorin, A.; Majumdar, A.; Gosser, Y.; Patel, D. J., Towards structural genomics of RNA: rapid NMR resonance assignment and simultaneous RNA tertiary structure determination using residual dipolar couplings. *J. Mol. Biol.* **2002,** *318*, 637-649.

171. Bondensgaard, K.; Mollova, E. T.; Pardi, A., The global conformation of the hammerhead ribozyme determined using residual dipolar couplings. *Biochemistry* **2002,** *41*, 11532-11542.

172. Bailor, M. H.; Musselman, C.; Hansen, A. L.; Gulati, K.; Patel, D. J.; Al-Hashimi, H. M., Characterizing the relative orientation and dynamics of RNA A-form helices using NMR residual dipolar couplings. *Nat. Protoc.* **2007,** *2*, (6), 1536-46.

173. Palmer, A. G., 3rd, Nmr probes of molecular dynamics: overview and comparison with other techniques. *Annu. Rev. Biophys. Biomol. Struct.* **2001,** *30*, 129-55.

174. Vold, R. L.; Waugh, J. S.; Klein, M. P.; Phelps, D. E., Measurement of spin relaxation in complex systems. *J. Chem. Phys.* **1968,** *48*, 3831-32.

175. Carr, H. Y.; Purcell, E. M., Effects of diffusion on free precession in nuclear magnetic resonance experiments. *Phys. Rev.* **1954,** *94*, 630-38.

176. Meiboom, S.; Gill, D., Modified spin-echo method for measuring nuclear spin relaxation times. *Rev. Sci. Instrum.* **1958,** *29*, 688-91.

177. Peng, J. W.; Thanabal, V.; Wagner, G., 2D heteronuclear NMR measurements of spin-lattice relaxation times in the rotating frame of Xnuclei in heteronuclearHX spin systems. *J. Magn. Reson.* **1991,** *94*, 82-100.

178. Noggle, J. H.; Shirmer, R. E., *The Nuclear Overhauser Effect: Chemical Applications*. Academic: New York, 1971.

179. Kay, L. E.; Torchia, D. A.; Bax, A., Backbone dynamics of proteins as studied by 15N inverse detected heteronuclear NMR spectroscopy: application to staphylococcal nuclease. *Biochemistry* **1989,** *28*, (23), 8972-9.

180. Abragam, A., *The Principles of Nuclear Magnetism*. Clarendon Press: Oxford, 1961.

181. Hiyama, Y.; Niu, C.; Silverton, J. V.; Bavoso, A.; Torchia, D. A., *J. Am. Chem. Soc.* **1988,** *110*, 2378-2383.

182. Lipari, G.; Szabo, A., Model-free approach to the interpretation of nuclear magnetic resonance relaxation in macromolecules. 2. Analysis of experimental results. *J. Am. Chem. Soc.* **1982,** *104*, 4559-4570.

183. Lipari, G.; Szabo, A., Model-free approach to the interpretation of nuclear magnetic resonance relaxation in macromolecules. 1. Theory and range of validity. *J. Am. Chem. Soc.* **1982,** *104*, 4546-4559.

184. Woessner, D. E., Nuclear Spin Relaxation in Ellipsoids Undergoing Rotational Brownian Motion. *J. Chem. Phys.* **1962,** *37*, 647-654.

185. Clore, G. M.; Szabo, A.; Bax, A.; Kay, L. E.; Driscoll, P. C.; Gronenborn, A. M., Deviations from the simple two-parameter model-free approach to the interpretation of nitrogen-15 nuclear magnetic relaxation of proteins. *J. Am. Chem. Soc.* **1990,** *112*, 4989 - 4991.

186. Zhang, Q.; Sun, X.; Watt, E. D.; Al-Hashimi, H. M., Resolving the motional modes that code for RNA adaptation. *Science* **2006,** *311*, (5761), 653-6.

187. Tugarinov, V.; Liang, Z.; Shapiro, Y. E.; Freed, J. H.; Meirovitch, E., A structural mode-coupling approach to 15N NMR relaxation in proteins. *J. Am. Chem. Soc.* **2001,** *123*, (13), 3055-63.

188. Vugmeyster, L.; Raleigh, D. P.; Palmer, A. G., 3rd; Vugmeister, B. E., Beyond the decoupling approximation in the model free approach for the interpretation of NMR relaxation of macromolecules in solution. *J. Am. Chem. Soc.* **2003,** *125*, (27), 8400-4.

189. Legault, P.; Hoogstraten, C. G.; Metlitzky, E.; Pardi, A., Order, dynamics and metal-binding in the lead-dependent ribozyme. *J. Mol. Biol.* **1998,** *284*, (2), 325-35.

190. Butcher, S. E.; Allain, F. H.; Feigon, J., Determination of metal ion binding sites within the hairpin ribozyme domains by NMR. *Biochemistry* **2000,** *39*, 2174-82.

191. Gonzalez, R. L., Jr.; Tinoco, I., Jr., Identification and characterization of metal ion binding sites in RNA. *Methods Enzymol.* **2001,** *338*, 421-43.

192. Ott, L. G.; Arnold, L.; Limmer, S., Proton NMR studies of manganese ion binding to tRNAderived acceptor arm duplexes. *Nucleic Acids Res.* **1993,** *21*, (25), 5859-5864.

193. Bertini, I.; Luchinat, C.; Parigi, G.; Pierattelli, R., NMR spectroscopy of paramagnetic metalloproteins. *Chembiochem* **2005,** *6*, (9), 1536-49.

194. Solomon, I., Relaxation processes in a system of two spins. *Phys. Rev.* **1955,** *99*, 559-565.

195. Bloembergen, N.; Morgan, L. O., Proton relaxation times in paramagnetic solutions. Effects of electron spin relaxation. *J. Chem. Phys.* **1961,** *34*, 842-850.

196. Iwahara, J.; Tang, C.; Marius Clore, G., Practical aspects of (1)H transverse paramagnetic relaxation enhancement measurements on macromolecules. *J. Magn. Reson.* **2007,** *184*, (2), 185-95.

197. Brünger, A. T., *X-PLOR Version 3.1: A system for X-ray crystallography and NMR*. Yale University Press: New Haven, Connecticut, 1993.

Chapter 2

Structure and dynamics of P4 in the absence and presence of Mg^{2+}[1]

Introduction

The highly conserved P4 helix in RNase P is a structural element that is important for function since mutations in this region have dramatic effects on catalysis[1]. Studies suggest that P4 binds to catalytically important metals but the location and binding of these metals and their effects on the P4 conformational dynamics is not known. Given its central location near the substrate, it is likely that the P4 conformation undergoes structural changes during the course of RNase P folding, substrate recognition, catalysis, and/or product release. However, at the onset of our studies, no information was available regarding the flexibility of P4 and its potential role in metal binding and catalysis.

To gain insights into the structural dynamics of P4 in solution we applied an integrated NMR strategy to comprehensively and quantitatively characterize local and global motions in the presence and absence of Mg^{2+}. Our NMR studies involved (i) resonance assignments, (ii) characterization of hydrogen bond alignment via $^{2h}J_{NN}$-COSY

[1] Reproduced in part from Getz M.M., Andrews, A.J., Fierke, C.A., and Al-Hashimi, H.M., *RNA*, **2006**, *13*, 251-266. In collaboration with Professor Carol A. Fierke and Dr. John Hsieh who supplied T7 polymerase used for RNA synthesis.

experiments[2, 3] (iii) RDCs for characterizing the average inter-helical structure and dynamics at sub-millisecond timescales[4-6] and (iv) domain-elongation in conjunction with spin relaxation measurements to characterize amplitudes and time constants for local and collective motional modes at picosecond-nanosecond timescales[7]. This NMR approach has allowed us to identify structural plasticity in P4 both in the presence and absence of Mg^{2+} that may play a role in various steps of RNase P catalysis.

I. Construct design and validation of P4

Our NMR studies targeted a P4 construct derived from *B. subtilis* enzyme which contains all of the universally conserved P4 residues (Fig. 2-1A). The *B. subtilis* sequence was chosen because this form of the enzyme can perform catalysis under high monovalent and divalent cation conditions, simplifying kinetics studies. Our specific P4 construct was also chosen to allow comparison with previous NMR studies on the *E. coli* sequence which employed a similar construct design[8].

At the start of this project, no high resolution structural information was known for RNase P and its secondary structure had been determined by comparative sequence analysis[9, 10]. In this technique sequences from a wide variety of organisms (that are thought to have a common ancestor) are aligned and any regions with a change in sequence but conserved base pairing are considered helices in the secondary structure. In the case of RNase P, both the A and B-type bacterial secondary structures were determined in this manner from comparing over 100 sequences of diverse organisms[11, 12]. A vast majority of the secondary structure was proven correct by the crystal structures,

however in the P4 region, the *B. stearothermophilus* crystal (which is in the same class as *B. subtilis*) shows a bulged A residue in domain 1 below the U bulge which was not

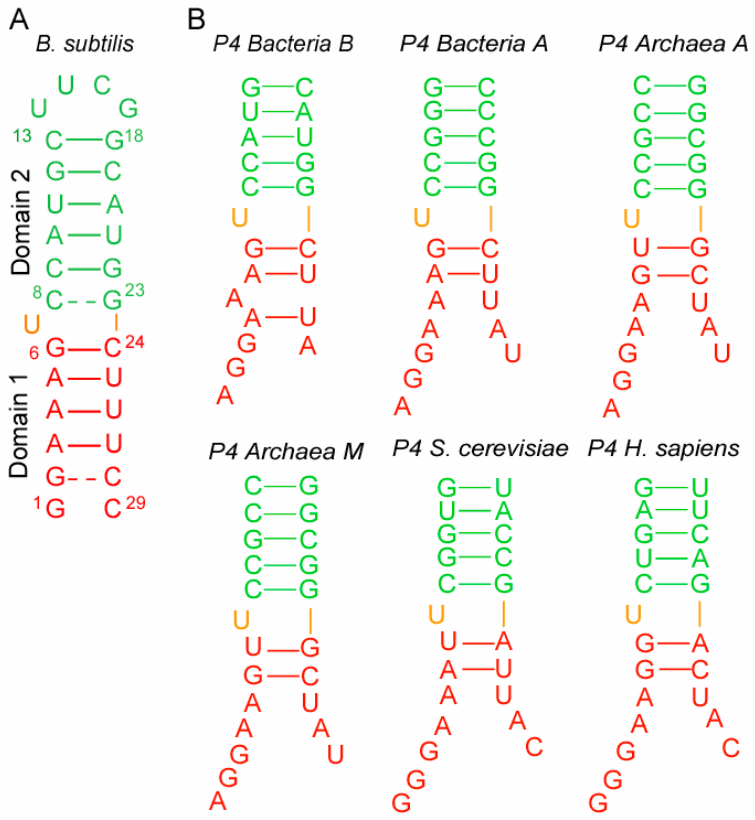

Figure 2-1. Secondary sequences of P4 in a variety of organisms. (A) The P4 construct from *B. subtilis*. (B) Sequences for the P4 helix in many organisms (Bacteria B[13], Bacteria A[14], Archaea A, Archaea M[15], *S. cerevisiae and H. sapiens*[16-21]) showing the conserved AA region in domain 1.

predicted by phylogenetic analysis[22].

We therefore explored how variations in secondary structure in the adenine region below the uridine bulge might impact the other regions of P4 by comparing the NMR spectra of an alternate P4 construct which is designed to have bulged out adenines (Fig. 2-2). Designing a construct with the middle adenine specifically bulged out while maintaining Watson-Crick A-U base-pairs above and below the adenine bulge as seen in

the X-ray structure was not feasible using our relatively small construct. Nevertheless, simply deleting a uridine in the lower helix led to a P4 sequence which based on Mfold [23] folds into two secondary structures with either of two adenines bulge out (Fig. 2-2). This sequence provided an opportunity to explore how variations in the lower helix impact the bulged uridine, its flanking base-pairs, and the upper helix.

Comparison of chemical shifts between the two constructs show the expected differences near the site of the U deletion in the lower helix (Fig. 2-2). However, very good agreement was observed for the uridine bulge and upper helix noting that small variations on the order of 0.04 ppm in ^{1}H are often seen from different sample preparations. Even for the G6-C24 base-pair below the bulge, good agreement is seen for some of the resonances (Fig. 2-2). Moreover, similar chemical shift perturbations were observed for the two constructs in 15 mM Mg^{2+} (data not shown). As shown in Figure 2.2, very good agreement is also observed between the site-specific Mg^{2+} binding affinities in the two constructs.

These experiments together with results that follow provide support for the functional relevance of our chosen P4 constructs.

II. Resonance assignment and hydrogen bond alignment of P4

Our initial NMR characterization focused on *B. subtilis* P4 under low ionic strength conditions in the absence of divalent ions (buffer conditions: 10 mM sodium chloride, 10 mM sodium phosphate, pH ~6.2). The ^{1}H, ^{13}C, and ^{15}N resonances were assigned using standard NMR experiments employing uniformly $^{13}C/^{15}N$ labeled or

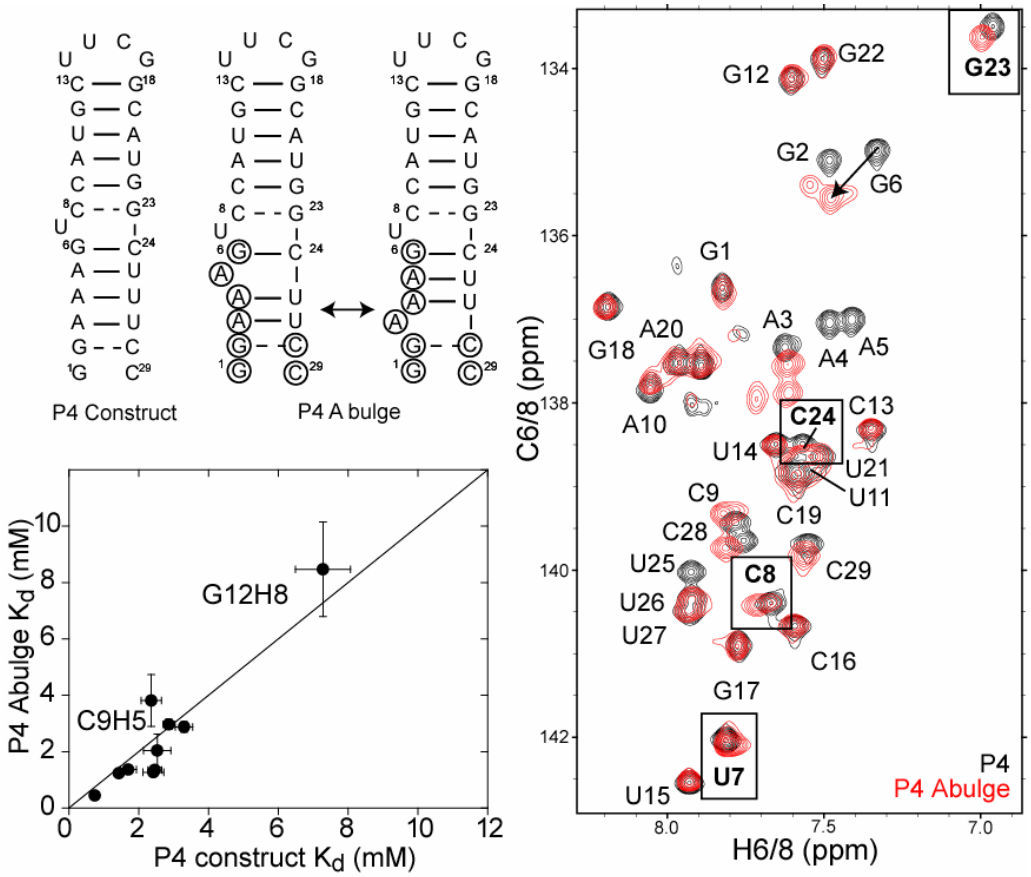

Figure 2-2. Comparison of P4 and A bulge P4 constructs. The P4 construct from *B. subtilis* used in our NMR studies with hydrogen bond alignments derived from the $^{2h}J_{NN}$-COSY experiment[2, 3] and the hypothesized secondary structures of the A bulge construct showing the two possible secondary structures. Residues with chemical shifts that are significantly different (> 0.04 ppm) from the original P4 construct are highlighted by circles. 2D HSQC spectrum showing C8H8/C6H6 resonances. In bold and boxes are sites around the bulge that are not significantly affected by the A bulge. Original P4 construct is in black, A bulge construct in red. Plot of P4 A bulge K_ds vs. original P4 construct K_ds. Error bars represent least squared fits to the two-state model K_d equation for ligand binding to RNA[24].

unlabeled P4[25]. The NOE walk between exchangeable protons was traced from U27 to G18 without interruption to assign all detected imino resonances of guanines and uridines (G1 was not detected and G2 slightly exchange broadened due to end-fraying effects, Fig. 2-3A)[26]. The NOE walk between nonexchangeable protons[26] was also uninterrupted from G18 to U25, indicating a continuous helical conformation. While the NOE walk was

interrupted at the U7–C8 junction on the opposite strand, observation of a weak NOE cross-peak between H1' of G6 and H6 of C8 is consistent with a pseudo- continuous helical conformation involving an unstacked looped out uridine bulge (Fig. 2-3B). No or weak NOE connectivities were observed between terminal residues G1/G2 and C28/C29 as in the exchangeable protons, due to end-fraying effects. In addition, the NOE cross-peaks between C8 and C9 and between G23 and C24 were comparatively weak, suggesting that the C8–G23 base pair is not fully formed. 2D HCN experiments were also used to assign sugar and base resonances (Fig. 2-3C)[27]. The proton assignments were then correlated with the carbon and nitrogen spins using 2D HSQC experiments. The H5 resonances were assigned with a 2D COSY experiment correlating H5 and H6 protons[28] (Fig. 2-3D).

The Watson-Crick hydrogen bond alignment was determined using a $^{2h}J_{NN}$-COSY experiment[2, 3] (Fig. 2-3E). Auto peaks (guanine and uridine residues) appear for hydrogen bond donors and cross-peaks appear for hydrogen bond acceptors (adenine and cytosine residues). Asymmetric Watson-Crick hydrogen bond alignments were revealed above and below the bulge. In particular, an anomalously weak *trans*-hydrogen bond cross peak was observed for the C8-G23 base-pair ($^2J_{NN}$ = 4.8 Hz) above the bulge but not for the G6-C24 base-pair ($^2J_{NN}$ = 5.2 Hz) below the bulge (Fig. 2-3E). These results suggest that the bulge introduces deviations from ideality in its flanking G–C base pairs, with the deviations being greater for the base pair above the bulge.

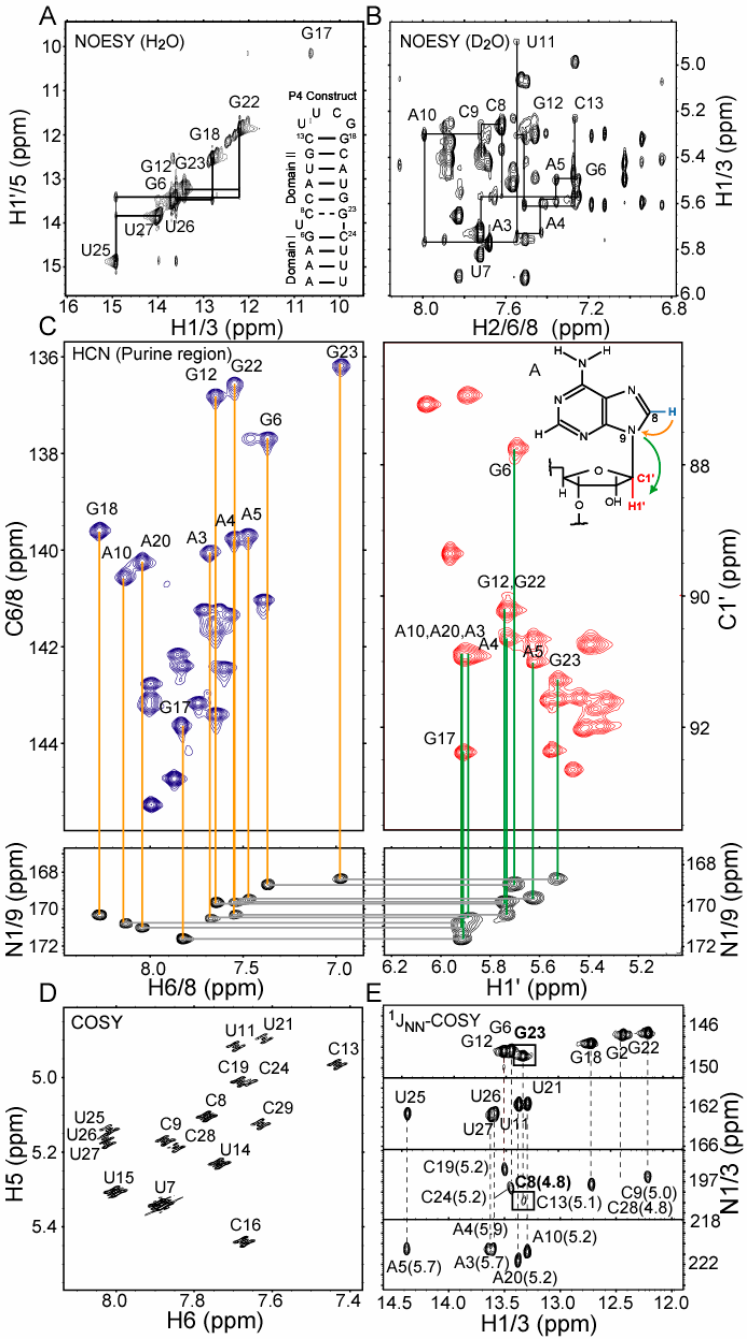

Figure 2-3. NMR assignments and hydrogen bond alignment of P4 in the absence of Mg^{2+}. (A) Expanded region of exchangeable NOESY of P4 showing walk from U27 to G18. P4, *B. subtilis* secondary structure, inset. (B) Expanded region of the NOESY spectrum of P4 for non-exchangeable protons showing the NOE walk for the A3-C13 strand. (C) 2D HSQC spectra showing aromatic and C1'H1' carbon/proton peaks and HCN spectra showing their corresponding intra-residue N1/9 peaks. (D) 2D COSY experiment displaying cross-peaks for H5 and H6 protons[28]. (E) Detection of hydrogen bond alignments using the $^{2h}J_{NN}$-COSY experiment[2, 3]. The measured $^{2h}J_{NN}$ coupling constants are shown adjacent to each cross peak[29].

III. Global structural dynamics of P4 by RDCs

Comparison of one bond C–H RDCs [C1'H1', C2H2, C5H5, C6H6, and C8H8] measured in P4 in the absence of divalent ions using 15 mg/mL of Pf1-phage[5, 6, 30, 31] provided qualitative insight into the structural dynamics of P4. As expected from a pseudo-continuous helical conformation, RDCs measured for a given type of vector fall within a relatively narrow range (Fig. 2-4A). The small RDCs observed for G1 likely reflect dynamical averaging due to end fraying. Most notable are the much smaller RDCs (near zero values) observed in base and sugar moieties of the U7 bulge (Fig. 2-4A). Though an unusual static conformation could not be ruled out, these attenuated RDCs suggest a high degree of local mobility at U7 occurring at submillisecond timescales. The comparatively smaller RDCs in the nucleobases of C8 and G23 are also indicative of an unusual conformation and/or flexibility that may explain their perturbed hydrogen bond alignment (Fig. 2-4A).

We determined the relative orientation and dynamics of the two P4 helical domains in the absence of divalent ions by subjecting RDCs measured in nonterminal residues to an order tensor analysis (Table 2.1)[32-34]. Watson–Crick regions of the two domains were modeled using an idealized A-form helix geometry, whereas the UUCG loop in domain 2 was modeled using an X-ray structure[35] as previously described for TAR[36]. The idealized A-form geometry has been validated for non-terminal Watson–Crick base pairs using RDCs in a number of different contexts[37, 38 34, 39-42]. Shown in Figure 2-4B is the correlation between measured and back-calculated RDCs (16 and 17 for domains 1 and 2, respectively) when independently fitting each domain to an order tensor. Owing to potential deviations from ideality, RDCs from G1-C29, G2-C28, and

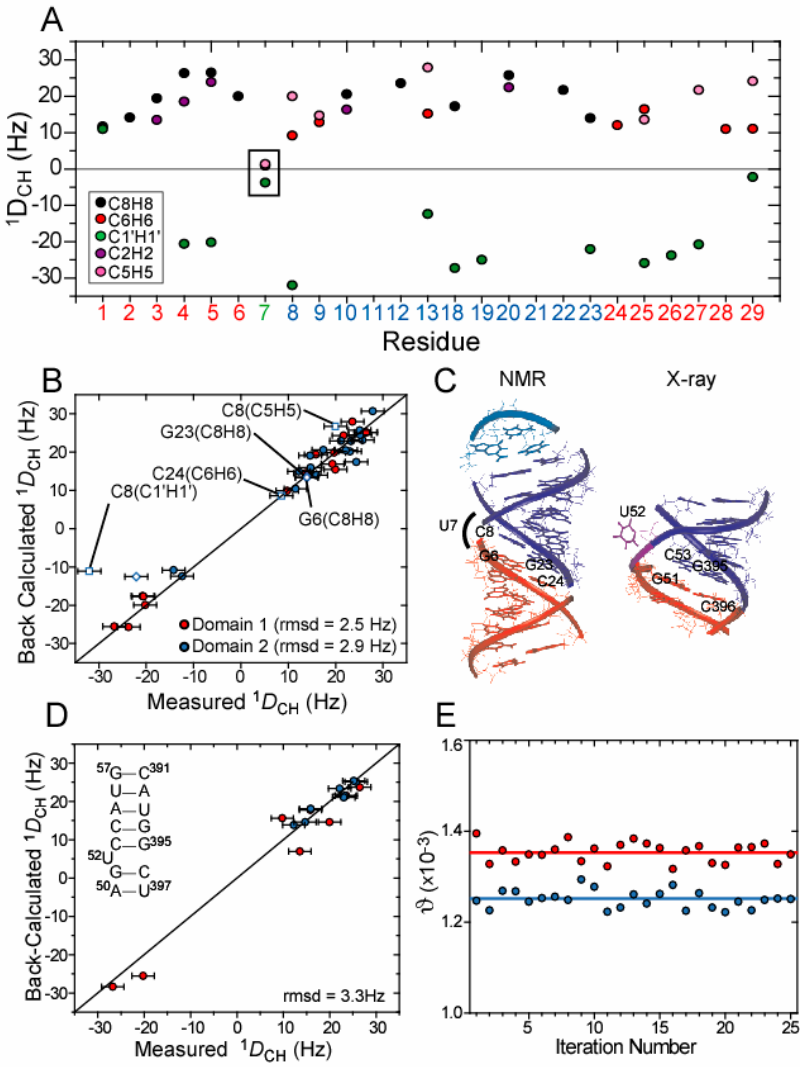

Figure 2-4. P4 order tensor analysis in the absence of Mg^{2+}. (A) One bond C-H RDCs measured in P4 as a function of residue. (B) Correlation plot between measured RDCs and back calculated values when independently fitting order tensors to an idealized A-form geometry for domains 1 (red) and 2 (blue). Error bars represent the RDC measurement uncertainty (2.4 Hz). RDCs from residues C8 (open squares) and G23 (open diamonds) are shown but were not included in the svd fit. (C) The RDC derived average inter-helical orientation obtained from superimposing order tensor frames (left). For comparison the X-ray structure of P4 in *B. stearothermophilus*[22] is also shown (right). (D) Correlation plot between measured and back-calculated RDCs when fitting RDCs against the X-ray structure of P4[22]. RDCs from domains 1 and 2 are shown in red and blue respectively. Inset shows residues common to both the NMR construct and crystal structure[22]. (E) The best-fit ϑ's for domains 1 (red) and 2 (blue) as a function of input RDCs over 25 iterations (circles) upon the removal of two random RDCs. Best-fit values when using all RDCs in each domain are shown as horizontal lines.

Table 2.1 P4 RDCs in 15 mg/mL phage in the absence of Mg^{2+}.

Residue(Domain1)	RDC (Hz)
3(C2H2)	14.5
3(C8H8)	19.3
4(C1'H1')	-20.6
4(C2H2)	19.7
4(C8H8)	26.3
5(C1'H1')	-20.2
5(C2H2)	23.6
5(C8H8)	26.5
6(C8H8)	19.9
24(C6H6)	9.8
25(C1'H1')	-20.8
25(C6H6)	15.8
25(C5H5)	13.6
26(C1'H1')	-23.7
27(C1'H1')	-26.8
27(C5H5)	21.7

Residue(Domain2)	RDC (Hz)
9(C5H5)	14.7
9(C6H6)	12.3
10(C8H8)	22.1
10(C2H2)	15.9
12(C8H8)	25.2
13(C1'H1')	-12.4
13(C5H5)	27.9
13(C6H6)	14.6
14(C1'H1')	-14.2
14(C5H5)	24.4
14(C6H6)	11.5
17(C1'H1')	21.1
17(C8H8)	25.1
18(C8H8)	17.4
20(C8H8)	25.7
20(C2H2)	23.0
22(C8H8)	23.3

C8-G23 were not included in this analysis. A very good fit is observed with the root-mean-square deviation (RMSD = 2.5 and 2.9 Hz for domains 1 and 2/loop, respectively) approaching the RDC measurement uncertainty (2.4 Hz) estimated from duplicate measurements[39]. This indicates that the targeted Watson–Crick residues in the two domains adopt the expected local A-form helix geometry. Importantly, significant deviations (~9.3 Hz) were observed between the sugar and base RDCs measured in residue C8 and values back-calculated assuming the idealized A-form helix and the above order tensor obtained from a fit that excludes the G23 and C8 RDCs (Fig. 2-4B, open symbols). The better agreement observed for the base RDCs in G23 suggests that its base moiety behaves as expected for an ideal Watson–Crick base pair. Thus, local structural perturbations in C8, which is adjacent to the flexible U7 bulge (see below), may explain

the anomalous hydrogen bonding observed in the C8–G23 base pair (Fig. 2-3E). Such RDC deviations were not observed in the G6–C24 base pair below the bulge (Fig. 2-4B).

The order tensor analysis of RDCs yields an order tensor frame for each helical domain (S_{xx}, S_{yy}, S_{zz}), which describes the average domain orientation relative to the applied magnetic field. The average orientation of domains relative to one another can be determined by superimposing their respective order tensor frames[32-34]. The latter amounts to insisting that the two domains have, on average, an equivalent view of the magnetic field direction when assembled into a proper average conformation. The relative orientation of the two P4 domains obtained by superimposing their respective RDC-derived order tensor frames is shown in Figure 2-4C. Consistent with the NOE data, the inter-helical conformation only slightly deviates from coaxial alignment. The average inter-helical bend and twist angles are 10° ± 5° and from -15° to 45°, respectively. This P4 conformation falls within the distribution of conformations reported in the previous NOE-based NMR structures of *E. coli* P4 (inter-helical bend and twist angles ranging between 12° and 34° and -42° and 43°, respectively)[8]. The P4 inter-helical angle of 10° is also in excellent agreement with that determined using transient electric birefringence for double helices containing a single uridine bulge (10° ± 5°)[43].

Comparison of the isolated P4 conformation derived by RDCs with that observed in the context of the 3.3 Å X-ray structure of the 417-nt RNA component of RNase P from the related bacteria *B. stearothermophilus* allowed us to evaluate the relevance of our P4 construct as well as assess possible differences arising from interactions present in the larger RNA context[22] (Fig. 2-4C). While the P4 inter-helical twist observed in the X-ray structure (~15°) is in excellent agreement with that obtained by RDCs (~15°), the X-

ray structure has a slightly more bent inter-helical angle (~17° compared to ~10°) (Fig. 2-4C). Due to the latter difference and the presence of inter-helical motions (see below), slightly less favorable agreement is observed when directly fitting the RDCs to matching regions on the P4 X-ray structure (RMSD = 3.3 Hz) (Fig. 2-4D). This difference cannot be attributed to the presence of divalent ions in the crystallization conditions since our results indicate that Mg^{2+} binding does not alter the P4 inter-helical alignment significantly (see below). Small differences in the inter-helical angle may arise from tertiary contacts between the upper stem of P4 and L8 that are present in the X-ray structure (Fig. 1-3) but not in the isolated P4 construct[22]. Another point of agreement between the X-ray structure and NMR data is the looped out U7 bulge conformation in which the nucleobase is not sterically forbidden from freely rotating around the χ angle[22]. Thus, the internal motions observed in U7 by RDCs (Fig. 2-4A) and motional narrowing (see below) also likely occur in the larger RNA context.

While the mean P4 inter-helical angle derived by RDCs in the absence of divalent ions differs only slightly from the X-ray structure, the RDCs provide evidence for dynamical excursions about the mean angle that would allow access to the conformation observed in the X-ray structure. The order tensor analysis of RDCs also yields a generalized degree of order (GDO, ϑ)[33, 34], which describes the degree of alignment experienced by each domain. Rigidly held domains will experience a common degree of alignment and therefore report identical ϑ's[33, 34]. However, inter-helical motions can result in different levels of domain alignment and hence different domain ϑ's. In the latter case, the ratio of the domain ϑ's, referred to as the internal generalized degree of order (ϑ_{int}) can be used to assess the amplitude of inter-helical motions varying between 1

for inter-helical rigidity and 0 for maximum inter-helical motions[33, 34]. In P4, the ϑ value obtained for domain 2 (1.25 x 10^{-3} ± 8%) was smaller than that obtained for domain 1 (1.35 x 10^{-3} ± 3%) (Fig. 2-4E, horizontal lines) yielding a ϑ_{int} value of ~0.93 ± 9%. The ϑ uncertainties reflect both RDC measurement uncertainty and structural noise in the A-form geometry as implemented in the program Aform- RDC[42]. Although the difference in the domain ϑ's is comparable to their experimental uncertainty, it was consistently observed regardless of the input RDCs used in the order tensor determination (Fig. 2-4E). More importantly, independent evidence for domain motions was obtained using motionally decoupled spin relaxation data (see below). The smaller level of order observed for domain 2 may be attributed to the location of the disordered C8–G23 base pair, and therefore the hinge point is closer to domain 2 than to domain 1. Assuming isotropic motions in a cone[34, 44], the observed ϑ_{int} value translates into domain motional amplitudes of 18°, yielding a P4 conformation in which the inter-helical angle varies dynamically between -8° and 28°. The P4 conformation observed in the X-ray structure of *B. stearothermophilus* (Fig. 2-4C) falls within this dynamical envelope. Thus, it is possible that tertiary contacts between the upper domain of P4 and L8 capture one of many possible P4 inter-helical conformations during folding of RNase P.

IV. Pico-to-nanosecond motions by motionally decoupled ^{15}N relaxation

To obtain further insight into both librational motions and collective dynamics, we used a recently described domain-elongation strategy to decouple internal motions in P4 from overall reorientation[7]. The elongation is accomplished by extending the size of the terminal domain 1 using a stretch of 22 Watson–Crick base pairs (Fig. 2-5A). This

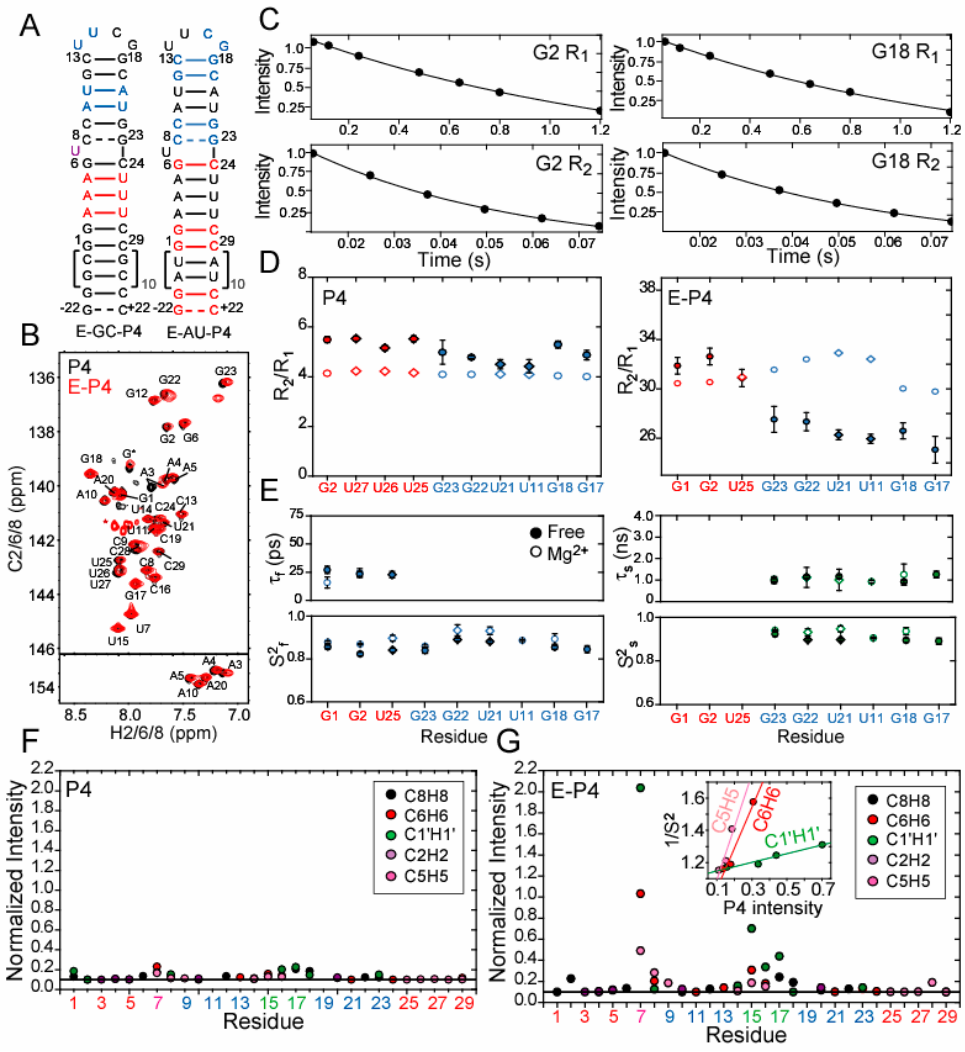

Figure 2-5. Measurement and extended Model-free analysis of E-P4 ^{15}N relaxation data in the absence of Mg^{2+}. (A) Secondary structure of E-GC-P4 and E-AU-P4. ^{13}C/^{15}N labeled and unlabeled residues are shown in color and black respectively. (B) 2D ^{1}H-^{13}C HSQC spectra of aromatic region of E-GC-P4 + E-AU-P4 (red) overlaid on non-elongated P4 (black). Natural abundance signals from elongation residues are indicated with an asterisk. (C) Examples of ^{15}N R_1 and R_2(CPMG) mono-exponential decays in E-P4. (D) The measured R_2/R_1 values for guanine (filled circles) and uridine (filled diamonds) residues in domains 1 (red) and 2 (blue) of P4 (left) and E-P4 (right). Values predicted using hydrodynamic calculations are shown as open symbols. (E) Dynamical parameters for E-P4 derived from extended model free analysis[45, 46]. Shown are the time constants/amplitudes for fast (τ_f / S^2_f) and slow (τ_s /S^2_s) internal motions in the absence of divalent ions (filled symbols) and in the presence of 15 mM $MgCl_2$ (open symbols). Shown are the normalized resonance intensities as a function of residue in (F) P4 and (G) E-P4 obtained from non-constant time ^{1}H-^{13}C HSQC experiments. Intensities for a given type of C-H vector are normalized relative to a minimum value of 0.1 indicated by a horizontal line[7]. Inset: $1/S^2$ (as determined by ^{2}H relaxation[47]) of the UUCG tetraloop as a function of P4 normalized intensity.

slows down overall rotational diffusion, allowing its separation from internal motions occurring at timescales comparable to overall molecular tumbling of non-elongated P4[45]. To avoid increasing NMR spectral overlap, two RNA constructs were prepared that are elongated using stretches of either unlabeled A–U (E-AU-P4) or G–C (E-GC-P4) base pairs in a background of uniformly $^{13}C/^{15}N$-labeled G–C or A–U nucleotides, respectively (Fig. 2-5A, colored residues).

We obtained high quality NMR spectra for E-P4 that exhibit excellent overlap with spectra of non-elongated P4 with minor chemical shift differences observed near the site of elongation (Fig. 2-5B). Folding of elongation residues into their predicted helical structure was confirmed based on a number of factors, including observation of intense imino proton peaks at the expected Watson–Crick chemical shift region (data not shown). The successful elongation of P4 supports the general applicability of this technique in studies of RNA dynamics.

Imino nitrogen (^{15}N) relaxation data were measured for guanine and uridine residues in both non-elongated and elongated P4 in the absence of divalent ions[7] (Fig. 2-5C, Table 2.2). As shown in Figure 2-5D, the transverse (R_2) to longitudinal (R_1) relaxation rate ratios (R_2/R_1) measured in the two domains of P4 are very similar. Given the expected isotropic overall tumbling of non-elongated P4, these data would normally be interpreted as evidence that the two domains are held rigid relative to one another. However, these data do not rule out the presence of domain motions that cannot be separated from overall molecular tumbling because they occur at similar timescales. Indeed, the corresponding data measured in E-P4 provides evidence for domain motions.

Table 2.2 ^{15}N Relaxation data for P4 and E-P4 and Model-free results for E-P4 in the absence of Mg^{2+}

P4	R_1 (Hz)	R_2 (Hz)
G2	1.294±0.158	8.880±0.125
U11	1.182±0.130	6.463±0.474
G17	1.326±0.166	8.050±0.251
G18	1.192±0.123	7.953±0.210
U21	1.195±0.136	6.679±0.324
G22	1.263±0.132	7.556±0.090
G23	1.292±0.136	8.027±0.750
U25	1.138±0.138	7.959±0.096
U26	1.163±0.141	7.565±0.124
U27	1.148±0.139	8.074±0.080

E-P4	R_1 (Hz)	R_2 (Hz)	NOE
G1	0.746±0.013	23.78±0.28	0.677±0.014
G2	0.709±0.010	23.13±0.35	0.661±0.013
U11	0.779±0.007	20.22±0.22	0.596±0.014
G17	0.853±0.032	21.39±0.47	0.636±0.023
G18	0.808±0.018	21.50±0.21	0.563±0.012
U21	0.779±0.011	20.47±0.13	0.589±0.014
G22	0.808±0.009	22.09±0.54	0.640±0.012
G23	0.828±0.016	22.80±0.75	0.647±0.022
U25	0.685±0.013	21.16±0.26	0.662±0.018

	Model	S^2_f	S^2_s	τ_f(ps)	τ_s(ns)	Γ_i
G1	2	0.857±0.008		27.295±3.314		0.253
G2	2	0.826±0.009		23.662±2.377		0.378
U11	5	0.881±0.007	0.898±0.005		1.163±0.065	0.000
G17	5	0.849±0.017	0.891±0.015		1.260±0.158	0.000
G18	5	0.850±0.009	0.900±0.009		0.872±0.073	0.000
U21	5	0.890±0.006	0.897±0.006		1.145±0.064	0.000
G22	5	0.869±0.015	0.901±0.009		1.258±0.092	0.000
G23	5	0.892±0.022	0.910±0.013		1.197±0.156	0.000
U25	2	0.841±0.009		22.756±3.270		0.000

As shown in Figure 2-5D, significantly smaller R_2/R_1 values are observed for the smaller domain 2 as compared to the elongated domain 1. This is despite the fact that for a rigid conformation, near minimum R_2/R_1 values are expected for domain 1 given that its N–H

bonds are oriented perpendicular to the long principal axis of anisotropic rotational diffusion[7]. Rather, the uniformly smaller domain 2 R_2/R_1 values are exactly as would be expected if domain 2 reoriented semi-independently at timescales faster than overall E-P4 tumbling. The excellent agreement between the domain 1 R_2/R_1 values and those predicted based on the RDC-derived E-P4 conformation and hydrodynamic calculations provides further support that elongation residues adopt the expected helical conformation[48] (Fig. 2-5D, open symbols).

We subjected the E-P4 ^{15}N relaxation data to an extended Model-free analysis[7, 45, 46, 49]. This yielded a time constant for overall E-P4 rotational diffusion in the absence of divalent ions (τ_M = 19.7 ± 0.2 and 19.1 ± 0.2 ns for E-AU-P4 and E-GC-P4, respectively) that is in very good agreement with hydrodynamic predictions (18.5 ns at 298 K)[48]. Similar N–H librations were observed throughout the two helices with time constants (τ_f) in the 23–27 ps range and amplitudes ranging between S^2_f = 0.83–0.89, where S^2_f is the Lipari–Szabo[45] spin relaxation order parameter, which varies between 0 and 1 for maximum and minimum motions (Fig. 2-5E, filled symbols, Table 2.2). The N–H sites in domain 2 experience an additional slower motional mode characterized by uniform amplitudes ($S^2_s \sim 0.90$) and time constants in the near nanosecond range (τ_s = 0.9–1.3 ns) (Fig. 2-5E, filled symbols). This is as expected if all of the N–H sites moved together as part of a common collective dynamical process. Remarkably, the amplitude of domain motions observed by relaxation ($S_s = 0.9^{1/2} = 0.95$) is in very good agreement with that obtained independently by RDCs (ϑ_{int} = 0.93). This suggests that the domain motions sensed by RDCs occur at nanosecond timescales and that little to no motions occur at micro- to millisecond timescales.

The E-P4 resonance intensities exposed local motions that evade detection in non-elongated P4 because they occur at timescales approaching overall molecular tumbling. Ignoring chemical exchange, the resonance intensity for a given C–H bond reports on the net bond vector reorientational dynamics relative to the applied magnetic field. In P4, very similar intensities were observed for various C–H sites (Fig. 2-5F). In contrast, significantly higher intensities indicative of fast internal motions were observed for a number of sites in E-P4, the most notable being the U7 bulge and UUCG loop (Fig. 2-5G). These motions escape detection in nonelongated P4 likely because they occur at timescales slower than overall tumbling (~5.6 ns). The motional narrowing at U7 confirms that the near zero RDCs measured at U7 reflect extensive dynamical averaging (Fig. 2-5G), painting a picture for the U7 bulge, which counter to previous NMR studies of P4[8], is essentially unstructured. Interestingly, slightly higher than average intensities were also observed for the neighboring C8, indicating that its unusual RDCs and hydrogen bond alignment may arise from dynamical disorder. Together, the locally mobile U7 and C8 provide a flexible hinge and thus a molecular basis for the observed domain motions. The virtually identical chemical shifts observed for U7 and C8 in E-P4 and P4 (Fig. 2-5B) underscore the point that the observed dynamics in E-P4 are not induced by elongation, but rather escape detection in non-elongated P4. As expected, the relative intensities for the UUCG loop are in excellent agreement with those reported for the UUCG loop in E-TAR[7], which are in turn in excellent agreement with motional amplitudes reported previously by ^{2}H relaxation[47] (Fig. 2-5G inset).

V. Global structural dynamics by RDCs of P4 in the presence of Mg^{2+}

To examine if and how Mg^{2+} affects the P4 structural dynamics, we repeated the NMR characterization in the presence of 15–20 mM Mg^{2+} (Mg^{2+} binding was initially confirmed in P4 as discussed in Chapter 3). Assuming a simple two state model, these Mg^{2+} concentrations are expected to lead to up to 89% of P4 being in the Mg^{2+} associated state. Results are summarized in Figure 2-6. Consistent with the relatively small Mg^{2+}-induced chemical shift perturbations, our results indicate that Mg^{2+} binding does not significantly alter the structure or dynamics of P4. This is in good agreement with previous studies on *E. coli* P4, in which NOESY data also argued that neither Mg^{2+} nor $Co(NH_3)_6^{3+}$ binding led to detectable changes in the P4 conformation[8]. The $^{2h}J_{NN}$-COSY spectrum recorded in the presence of Mg^{2+} shows hydrogen bond alignments very similar to those observed in free P4 (Fig. 2-3E), including diminished auto- and cross-peak intensities as well as $^{2h}J_{NN}$ coupling constants for the C8– G23 base pair above the bulge (Fig. 2-6A). Interestingly, however, Mg^{2+} binding does result in an increase in all of the measured $^{2h}J_{NN}$ coupling constants, consistent with greater stabilization of the helical structure relative to the low ionic strength conditions.

Order tensor analysis of P4 RDCs measured in the presence of Mg^{2+} also showed very little change in the local conformation of domains or their average relative orientation (Table 2.3). The two domains exhibit an equally good fit to the idealized A-form geometry (Fig. 2-6B) as observed for the RDCs measured in the absence of Mg^{2+} (Fig. 2-4B). The RDCs also show that deviations of C8 from ideality persist in the presence of Mg^{2+} (Fig. 2-6B). The average inter-helical alignment obtained from the RDCs measured in Mg^{2+} (inter-helical bend and twist angles of 11° ± 5° and from -15° to

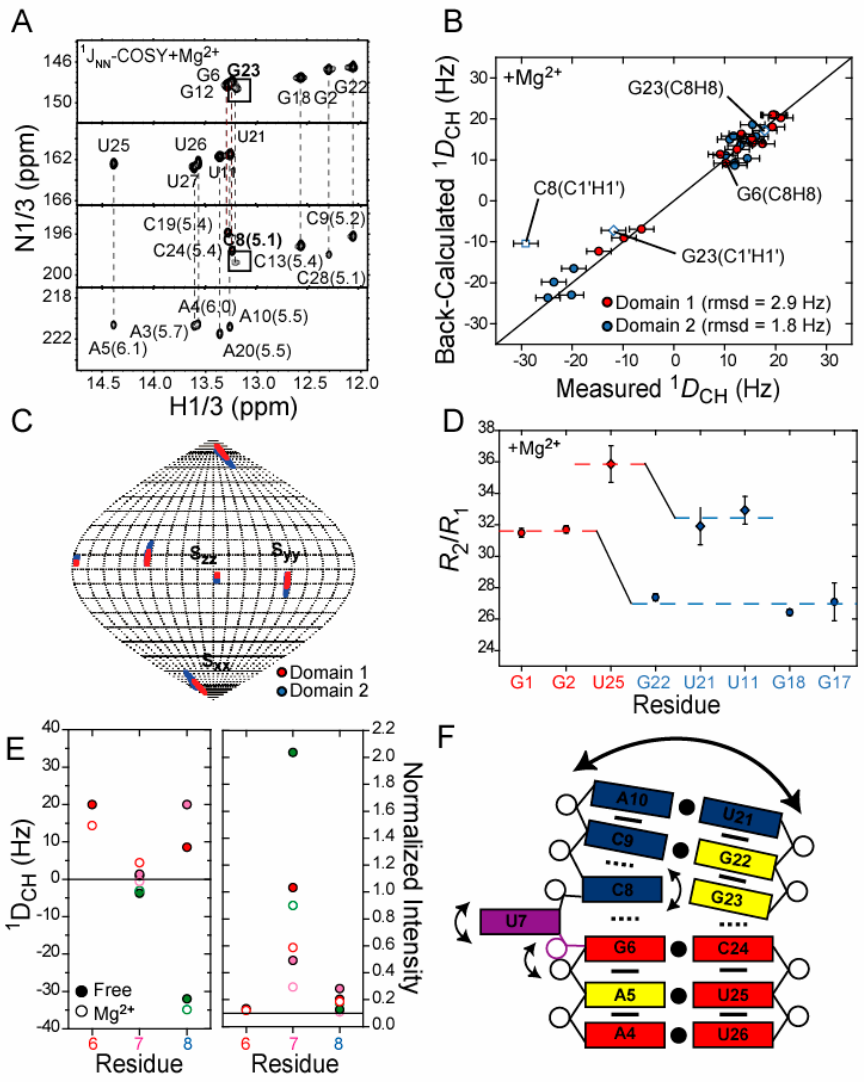

Figure 2-6. Structural dynamics of P4 in the presence of Mg^{2+}. (A) $^{2h}J_{NN}$-COSY spectrum of P4 in Mg^{2+}. The $^{2h}J_{NN}$ coupling constants (in Hz) are shown next to each cross peak[29]. (B) Correlation plot between P4 RDCs measured in 20 mM Mg^{2+} and values back-calculated when independently fitting order tensors to an idealized A-form geometry for domains 1 (red) and 2 (blue). Error bars represent measurement uncertainty (2.4 Hz as for free, Fig. 2-4B)). RDCs from residues C8 (open squares) and G23 (open diamonds) are shown but were not included in the analysis. (C) Sanson-Flamsteed[50] projection map shows orientation of order tensor frames (S_{xx}, S_{yy}, and S_{zz}) for domains 1 (in red) and 2 (in blue) determined in the presence of Mg^{2+}. Results are shown relative to the free P4 inter-helical conformation determined using RDCs in the absence of Mg^{2+}. (D) ^{15}N R_2/R_1 values for guanine (circles) and uridine (diamonds) residues measured in P4 in the presence of 15 mM Mg^{2+}. Average values for each domain are shown as dotted lines. (E) One-bond C-H RDCs in P4 (left) and normalized intensities in E-P4 (right) in the bulge and flanking residues measured in the absence (filled symbols) and presence (open symbols) of $MgCl_2$. (F) Schematic diagram of local and global motions in P4 and Mg^{2+} association (yellow residues).

Table 2.3 P4 RDCs in 15 mg/mL phage in 15 mM Mg^{2+}.

Residue(Domain1)	RDC (Hz)	Residue(Domain2)	RDC (Hz)
3(C2H2)	12.0	9(C6H6)	19.4
3(C8H8)	14.5	10(C8H8)	21.0
4(C1'H1')	-23.6	11(C1'H1')	-9.8
4(C2H2)	13.0	11(C5H5)	19.9
4(C8H8)	16.2	12(C8H8)	15.3
5(C1'H1')	-24.8	13(C1'H1')	-6.4
5(C2H2)	15.5	13(C5H5)	19.5
5(C8H8)	15.0	13(C6H6)	9.1
6(C8H8)	12.0	14(C1'H1')	-14.8
25(C6H6)	10.1	14(C5H5)	10.3
25(C5H5)	11.7	17(C1'H1')	13.3
26(C1'H1')	-19.7	18(C8H8)	12.4
26(C5H5)	13.8	20(C8H8)	17.5
27(C1'H1')	-20.1	21(C5H5)	15.5
27(C5H5)	11.0	22(C8H8)	19.7

45°) is virtually identical to that obtained in the absence of Mg^{2+} (inter-helical bend and twist angles of 10° ± 5° and from -16° to 44°, respectively). This result is illustrated in Figure 2-6C, on a Sanson-Flamsteed projection map[50], which is a projection of a sphere onto a plane where the horizontal lines run from -90° to 90° in 10° increments and vertical lines run from -180° to 180° in 20° increments. The domain 1 and 2 order tensor frames for Mg^{2+} and free P4 overlap one another about all three principal directions (S_{xx}, S_{yy}, and S_{zz}), indicating that Mg^{2+} binding does not alter the average P4 inter-helical alignment. Interestingly, the same order tensor analysis yields a ratio for the domain order (ϑ_{int} = 0.80 ± 8%), which is smaller than that observed in the absence of Mg^{2+} (ϑ_{int} = 0.93 ± 9%). Thus, Mg^{2+} binding does not arrest domain motions in P4.

VI. Pico-to-nanosecond motions by motionally decoupled ^{15}N relaxation of P4 in the presence of Mg^{2+}

The persistence of domain motions in the presence of Mg^{2+} was also confirmed by the ^{15}N relaxation data measured in E-P4 in 20 mM Mg^{2+} (Table 2.4). As shown in Figure 2-6D, the R_2/R_1 values measured in domain 2 exhibit a similar level of attenuation (~12%) relative to values measured in domain 1 as is observed in free E-P4 (~15%) (Fig. 2-5D). Model-free analysis of the Mg^{2+} relaxation data yielded dynamical parameters that are very similar to those obtained in free E-P4 (Fig. 2-5E, open symbols). It is important to note that the Mg^{2+}-induced chemical shift perturbations observed in E-P4 were virtually identical to those observed in non-elongated P4, further confirming that elongation does not disturb the integrity of P4 (data not shown). Slightly higher Mg^{2+} concentrations were required to induce the chemical shift perturbations observed in small P4, likely due to the presence of competing sites in the elongation residues of E-P4. Interestingly however, unlike for free E-P4, we observe systematically higher R_2/R_1 values for E-GC-P4 compared to E-AU-P4 in the presence of Mg^{2+} (Fig. 2-6D). This systematic difference reflects the slightly reduced overall tumbling rate for E-GC-P4 (τ_M = 20.2 ns) compared to E-AU-P4 (τ_M = 19.2 ns) in the presence of Mg^{2+}. This may arise from greater association of Mg^{2+} ions with long stretches of alternating GCs in the E-GC-P4 construct, which may modify the overall hydrodynamic properties of the RNA.

Finally, results also indicate the persistence of significant local motions in the U7 bulge in the presence of Mg^{2+}. As shown in Figure 2-6E, the U7 RDCs remain near zero and are hardly affected by Mg^{2+} binding. Although a small reduction in the U7 resonance intensities in E-P4 is observed relative to the free form, they remain significantly

Table 2.4 ^{15}N Relaxation data for E-P4 and Model-free results in Mg^{2+}

E-P4+Mg^{2+}	R_1 (Hz)	R_2 (Hz)	NOE
G1	0.762±0.005	23.99±0.16	0.760±0.024
G2	0.754±0.005	23.91±0.09	0.693±0.020
U11	0.726±0.013	23.90±0.48	0.661±0.097
G17	0.859±0.026	23.27±0.76	0.703±0.061
G18	0.839±0.005	22.18±0.10	0.587±0.018
U21	0.742±0.011	23.68±0.80	0.644±0.094
G22	0.827±0.005	22.65±0.13	0.687±0.019
U25	0.672±0.018	24.10±0.45	0.685±0.108

	Model	S^2_f	S^2_s	τ_f(ps)	τ_s(ns)	Γ_i
G1	2	0.874±0.005		14.582±4.677		0.941
G2	2	0.867±0.003		23.783±3.787		0.980
U11	5	0.931±0.018	0.947±0.014		1.006±0.498	
G17	5	0.891±0.024	0.935±0.017		1.264±0.506	0.000
G18	5	0.876±0.004	0.909±0.004		0.868±0.056	0.000
G22	5	0.887±0.005	0.917±0.004		1.420±0.137	0.000
U21	5	0.933±0.026	0.932±0.016		1.124±0.466	
U25	1	0.897±0.014				

elevated relative to the reference value of 0.1. The observed decrease in resonance intensities may also reflect exchange broadening due to nonspecific Mg^{2+} association and not necessarily a reduction in motional amplitudes.

Discussion

Our study illuminates dynamical aspects and metal binding properties of P4 that may be relevant to its function. It also provides new insight into the dynamical nature of RNA and how it can be studied using a combination of NMR techniques. We have validated the P4 construct by comparison with the A bulge P4 (secondary sequence found in the crystal structures) based on identical chemical shifts for the regions of interest,

identical locations of significant chemical shift changes upon addition of Mg^{2+}, and correlated binding affinities.

The combined application of RDCs and motionally decoupled spin relaxation data allowed us to better define the overall dynamics of P4 both in providing complementary information as well as in affording a unique opportunity to cross-validate results. The domain elongation proved to be absolutely critical for the spin relaxation studies[7], without which little to no information would have been obtained about the dynamics of P4. Our ability to observe small amplitude (~ 18°) domain motions in P4 in the presence and absence of Mg^{2+} ions was greatly aided by independent observation of the motions using RDCs and spin relaxation. This also afforded an opportunity to probe the amplitude of motions at two different timescale regimes, namely, pico- to nanosecond and pico- to millisecond. The similar domain motional amplitudes obtained by RDCs and spin relaxation in the absence of Mg^{2+} suggest that the domain motions occur at nanosecond timescales and that few to no domain motions occur at nano- to millisecond timescales. In contrast, the presence of slower domain motions at nano- to millisecond timescales cannot be ruled out in the presence of Mg^{2+}, given that the RDCs report slightly larger domain motional amplitudes compared to the ^{15}N relaxation data. There is precedence for such small amplitude domain motions across the single uridine bulge in P4. The P4 domain motional amplitudes in the absence of Mg^{2+} are roughly one-third those observed across the trinucleotide TAR bulge under nearly identical salt conditions[7] and about half those observed across dinucleotide symmetric uridine bulges by electric birefringence[51]. The combination of RDCs and spin relaxation also proved critical in deciphering the local dynamics of P4. While the near zero RDCs measured in the U7

bulge in the presence and absence of Mg^{2+} provided evidence for extensive local mobility, an unusual conformation with bond vectors oriented along the magic angle could not be ruled out. The motional narrowing of U7 observed in both the presence and absence of Mg^{2+} provided independent support for local mobility at this site, allowing interpretation of the RDCs in terms of an unstructured U7 conformation. It is remarkable that the mobility at U7 seems to entirely escape detection in nonelongated P4. This is likely because the motions occur at timescales approaching overall molecular tumbling. Taken together, our results reinforce the existence of a universe of nanosecond motions that has so far been difficult to probe using conventional NMR relaxation methods because motions occur at timescales slower than overall tumbling of the non-elongated RNA[7].

We propose that the functional role of the newly discovered P4 flexibility plays an important part in substrate binding and/or the catalytic cycle. It is increasingly recognized that RNA residues involved in intermolecular recognition are often flexible in the unbound state[52-54]. Such structural plasticity allows for dynamic optimization of induced fit intermolecular interactions with diverse targets. In this context, the inter-helical mobility observed in P4 may play a role in facilitating changes in domain orientation that lead to tertiary interactions between the upper domain of P4 and L8 during RNase P folding. It is also possible that the P4 inter-helical alignment undergoes further changes during the course of catalysis especially to allow recognition and cleavage of the diverse set of pre-tRNA molecules. In this regard, our results uncover a high degree of local mobility in two highly conserved residues, U7 and C8, which have been shown to be important in binding pre-tRNA[1, 55]. In addition to phosphorothioate

substitution studies[56] (Fig. 1-4), cross-linking data suggest that U7 directly interacts with the tRNA acceptor stem five residues from the cleavage site[57]. Available models show this interaction with the P4 domain running parallel to the acceptor stem of the pre-tRNA substrate[22, 58-60](Fig. 1-7). Dynamics at U7 is consistent with its looped out conformation observed in the larger RNase P context (Fig. 2-4C). These local motions, together with fluctuations at C8 and inter-helical flexibility, may allow for adaptive conformational changes that allow induced-fit interaction with diverse pre-tRNA substrates.

It is instructive to try to explain the motions observed in P4 in terms of its sequence. The NOE, $^{2h}J_{NN}$-COSY, RDC, and resonance intensity data all suggest that the presence of the uridine bulge leads to greater perturbation of the C8–G23 base pair, and specifically C8 above the bulge compared to the G6–C24 base pair below the bulge (Fig. 2-6F). This is likely due to the more flexible nature of the U7–C8 versus G6–U7 stack. Thus, the P4 sequence appears to code for a flexible U7/C8 pivot point and concomitant inter-helical flexibility. These are subtle features determined by the P4 sequence that are difficult to visualize on the basis of static structures (Fig. 2-6F). In addition to changing the relative orientation of the two helical domains, movement of the bulge, which has been shown to have deleterious consequences on RNase P activity[1], will likely disrupt this dynamical network.

Most biochemical studies have shown that catalytically important metals bind to P4 in the adenine stretch below the bulge[61-63]. Our results show that Mg^{2+} binding does not significantly alter the structure and/or dynamics of P4 and thus does not seem to play the role of changing the isolated P4 conformation. Rather, the association of Mg^{2+} ions near a site of flexibility (U7 and C8) that is known to interact with the pre-tRNA

substrate suggests a possible role in substrate binding. It is possible that the P4-associated metals form nonspecific intermolecular backbone bridging interactions with the tRNA substrate. Such Mg^{2+} intermolecular bridges have been observed between 16S and 30S ribosomal subunits[64] and between the thiamine pyrophosphate riboswitch and its cognate ligand TPP (thiamine pyrophosphate)[65]. These interactions could aid in positioning the pre-tRNA substrate relative to the active site[57].

Materials and Methods

Preparation and purification of $^{13}C/^{15}N$ labeled RNA

P4, E-AU-P4, and E-GC-P4 RNA samples (Figs. 2-1A, 2-5A) for NMR studies were prepared by *in vitro* transcription reactions using T7 RNA polymerase[66], uniformly $^{13}C/\ ^{15}N$ labeled (Spectra Stable Isotopes, Inc. and ISOTEC, Inc.) or unlabeled (Sigma) nucleotide triphosphates, and synthetic DNA templates (Integrated DNA Technologies, Inc.) containing the T7 promoter and sequence of interest. A second P4 NMR sample for measurement of RDCs was prepared containing 15 mg/mL of Pf1 phage[31] (Asla Biotech). For details see Appendix. Final buffer conditions for NMR samples were: 10 mM NaCl, 10 mM sodium phosphate, pH 6.2, 10 % D_2O. For nonexchangeable NOE assignment, precipitated RNA was dissolved in D_2O and repeatedly exchanged into the above NMR buffer made with 99.96% D_2O (Cambridge Isotope Laboratories, Inc.). The final RNA concentration in the NMR samples ranged between 0.6 and 1 mM.

NMR spectroscopy

Resonance assignments and relaxation experiments were carried out on an Avance Bruker 600 MHz NMR spectrometer equipped with a triple-resonance 5-mm cryogenic probe at 298 K (288 K for nonexchangeable NOESY). The RDCs for P4 and P4-Mg were measured on an Avance Bruker 600 MHz NMR spectrometer equipped with a triple-resonance 5-mm cryogenic probe and an 800 MHz Varian Inova spectrometer equipped with a triple-resonance Z-gradient probe, respectively. Sample volumes of ~300 μL in Shigemi tubes were used in all experiments. Carrier frequencies for HSQC experiments were as follows: ^{1}H 4.69 ppm, ^{13}C1' 89.50 ppm, ^{13}C5 99.00 ppm, and ^{15}N 154 ppm. NMR spectra were processed using NMRPipe/NMRDraw[67] or Felix[68], analyzed using NMRView[69], and overlaid using SPARKY 3[70]. The $^{2h}J_{NN}$-COSY experiment was used to determine hydrogen bond alignment at 298K with a mixing time of 15 ns[2, 3]. The following formula was used to calculate the scalar coupling constant between nitrogen atoms: $I_c / I_d = \tan^2(2\pi J_{NN} T)$ where I_c is the intensity of the cross peak, I_d is the intensity of the diagonal peak, T is the transfer time (here 15 ns), and J_{NN} is the scalar coupling[2]. The ^{1}H–^{13}C splittings were measured in the divalent ion-free P4 sample as the difference in the upfield and downfield components of the ^{13}C–^{1}H doublet along the ^{1}H and ^{13}C dimension, which were measured in separate subspectra using 2D ^{13}C–^{1}H S^{3}CT HSQC experiments[40, 71, 72]. The two sets of RDCs computed from the differences in splittings measured in the presence and absence of phage (15 mg/mL) yielded an RMSD of 2.4 Hz (data not shown). The average value from the two independent measurements was used whenever possible. The RDCs for P4 in the presence of 20 mM Mg^{2+} were obtained using splittings measured in the ^{13}C dimension.

In all cases, spectra of P4 in the presence and absence of the phage medium were nearly identical (barring the expected small perturbations from residual chemical shift anisotropies), indicating that phage does not directly or indirectly (e.g., by sequestering Mg^{2+}) affect the P4 conformation. In all cases, RDCs from base pairs G1–C29, G2–C28, and C8–G23, which based on the $^{2h}J_{NN}$-COSY experiment have partial or no hydrogen bonding, were excluded from analysis. All resonance intensities were measured using 2D $^{1}H–^{13}C$ HSQC experiments as previously described[7]. The intensity for each type of C–H spin was normalized to a minimum value of 0.1 independently for G–C and A–U residues (Fig. 2-5F,G, and 2-6E).

All of the ^{15}N relaxation data were measured in free (P4 and E-P4) and Mg^{2+} (E-P4) samples closely following the procedure described previously[7]. Briefly, imino ^{15}N longitudinal (R_1) and transverse ($R_{2(CPMG)}$) relaxation rates and $^{1}H–^{15}N$ NOEs were measured using well-established 2D experiments[73]. The R_1 experiment incorporated a recently described heat compensation element[74]. The relaxation delays for free P4 were 0.02, 0.06, 0.12, 0.24, 0.48, 0.64, and 0.80 sec and for E-P4, and E-P4-Mg were 0.02, 0.06, 0.12, 0.24, 0.48, 0.64, 0.80, and 1.2 sec. The $R_{2(CPMG)}$ experiment employed a recently described $[0013]^N$ phase cycle in the Carr– Purcell–Meiboom–Gill (CPMG) pulse train for suppressing artifacts arising from off-resonance effects[75]. The following relaxation delays were used for P4, E-P4, and E-P4- Mg: 0.0062, 0.0124, 0.0248, 0.0372, 0.0496, 0.0620, and 0.0744 sec. The final R_2 values were corrected to account for off-resonance effects as previously described[75]. The uncertainties were also verified based on duplicate measurements of relaxation data. The $^{1}H–^{15}N$ NOEs were measured from pairs

of spectra recorded with and without proton saturation during the recycle delay. The NOE uncertainty was estimated from the standard deviation of the baseline in the spectra.

Detection of Mg^{2+} association by chemical shift mapping

Changes in chemical shift upon addition of Mg^{2+} were quantified using the equation $\Delta\delta = \sqrt{(\Delta\delta_H)^2 + (\alpha\Delta\delta_X)^2}$, where $\Delta\delta_H$ and $\Delta\delta_X$ are the changes in proton and carbon/nitrogen chemical shift and α is the ratio of the C/N and H gyromagnetic ratio. The terminal residues were excluded from the analysis. The most significant changes (> 0.08 ppm, using the above equation) for each vector type are highlighted on the A bulge secondary structure (Figure 2-2). To measure site-specific binding affinities for P4 and the A bulge constructs, 2D HSQC spectra were recorded following incremental addition of $MgCl_2$ (0.5, 1, 3, 5, 10, and 15 mM). The apparent K_d values were obtained using the following equation[24]:

$$\delta_{obs} = \frac{\Delta\delta_T\{([Mg^{2+}]_T + [RNA]_T + K_d) - \sqrt{([Mg^{2+}]_T + [RNA]_T + K_d)^2 + (4[Mg^{2+}]_T[RNA]_T)}\}}{2[RNA]_T},$$

where δ_{obs} is the observed chemical shift, $\Delta\delta_T$ is the chemical shift difference between the free and fully bound state, $[Mg^{2+}]_T$ is the amount of added $MgCl_2$, and $[RNA]_T$ is the RNA concentration obtained from its absorbance at 260 nm. The data were fitted using Origin (Origin Lab Corp.) in which the unknown values $\Delta\delta_T$ and K_d are optimized during the fit (Figure 2-2).

Order tensor analysis of RDCs

Watson–Crick residues in domains 1 and 2 were modeled using idealized A-form helices constructed using the program Insight II (Molecular Simulations, Inc), noting that the propeller twist angles had to be corrected from +15° to the standard A-form value of -15°. An X-ray structure of the UUCG loop[35] was appended to domain 2 by superimposing the common closing base pairs as previously described[36]. RDCs from the highly flexible U15 and C16 loop residues were also excluded from analysis[47]. The 16/17 and 15/15 RDCs measured in domains 1/2 in the absence and presence of Mg^{2+}, respectively, together with the above domain structures were used to obtain best-fit order tensors for each domain using singular value decomposition implemented in the program RAMAH (an in-house modified version of ORDERTEN_SVD[32]). The overall structure of P4 was assembled by rotation of each domain into the principal axis system of its best-fit order tensor and fixing the translational disposition of the two domains by setting the distance between C24(P) and G23(O3') equal to ~1.59 Å (Fig. 2-4C). Three of four degenerate domain–domain orientations involving rotation of 180° about the three order tensor principal axes were omitted: two solutions (180° S_{xx} and 180° S_{yy}) because they yielded anti-parallel helical alignments and a third (180° S_{zz}) because it yielded a G6(O3')–C8(P) distance (~28 Å) that could not be linked using a single U7 residue. The program PALES[76] (http://spin.niddk.nih.gov/bax/) was used to compare the experimental order tensor frame for P4 with its counterpart predicted based on its overall molecular shape (difference in the S_{zz} orientation was ~4° and ~3° for the free and Mg^{2+} bound P4, respectively). Inter-helical angles were calculated using in-house written software[77]. In all cases, the uncertainty in the order tensor parameters was computed using the program

Aform-RDC, which takes into account both RDC uncertainty and parameterized deviations in the assumed idealized A-form helix geometry[42]. An order tensor fit was also carried out against the X-ray structure of P4 from *B. stearothermophilus*[22] (PDB ID #2A64; Fig. 2-4B) using 16 [A5 ($^1D_{C1'H1'}$, $^1D_{C2H2}$, $^1D_{C8H8}$), G6 ($^1D_{C8H8}$), C9 ($^1D_{C5H5}$, $^1D_{C6H6}$), A10 ($^1D_{C2H2}$, $^1D_{C8H8}$), G12 ($^1D_{C8H8}$), A20 ($^1D_{C2H2}$, $^1D_{C8H8}$), G22 ($^1D_{C8H8}$), and C24 ($^1D_{C6H6}$), U25 ($^1D_{C1'H1'}$, $^1D_{C5H5}$, $^1D_{C6H6}$)] and 14 [A5 ($^1D_{C1'H1'}$, $^1D_{C2H2}$, $^1D_{C8H8}$), G6 ($^1D_{C8H8}$), C9 ($^1D_{C6H6}$), A10 ($^1D_{C8H8}$), U11 ($^1D_{C1'H1'}$, $^1D_{C5H5}$), G12 ($^1D_{C8H8}$), A20 ($^1D_{C8H8}$), U21($^1D_{C5H5}$), G22 ($^1D_{C8H8}$), U25 ($^1D_{C5H5}$, $^1D_{C6H6}$)] RDCs measured in free and Mg^{2+}-bound P4, respectively, that correspond to bond vectors in common sequence regions in the two domains (i.e., residues 50, 51, 54, 55, 57, 392, 394, 396, and 397).

Inter-helical bend and twist angles for the *E. coli* NMR structure[8] and the *B. stearothermophilus*[22] and *T. maritime*[59] crystal structures were determined by superimposing phosphate backbone and sugar atoms of elongated (by 20 base pairs) A-form helices generated by InsightII (Molecular Simulations, Inc.) and modified slightly to match RDC data[42], then the χ tensor values[77] for each domain and thus their inter-helical orientation were calculated.

Model-free analysis of relaxation data

Insight II (Molecular Simulations, Inc.) was used to *in silico* elongate domain 1 of the RDC-derived P4 structure using a stretch of 22 base pairs. The E-P4 and P4 structures were subjected to hydrodynamic calculations using the program HYDRONMR[48] as previously described[7]. The HYDRONMR computed diffusion tensor parameters and P4/E-P4 structure were then used to compute ^{15}N R_2/R_1 values using in-house-written

software. The R_1 and R_2 values and their uncertainties measured from ^{15}N relaxation data were determined by nonlinear least-squares fitting of experimental data to the monoexponential function, $I(t) = I(0)e^{(-Rxt)}$ based on the Levenberg–Marquardt (LM) algorithm implemented in the software Origin (Origin Lab Corp.; Fig. 2-5C). The final R_2 values were corrected to account for off-resonance effects as previously described[75]. The R_1, R_2, and NOE values measured in E-P4 and E-P4- Mg were subjected to an extended Model-free analysis[45, 46] (Fig. 2-5E) using the software Model-free (Version 4.16 for Linux) provided by Palmer and coworkers[49] closely following the procedure described previously[7]. This analysis assumed (1) the decoupling approximation[45, 46], (2) an axially symmetric overall diffusion tensor, and (3) a diffusion tensor with D_{ratio} ($D_{//}D_{\perp} = 5.3$) and orientation computed using HYDRONMR[48] and the RDC derived average P4 inter-helical conformation. Model selection of the ^{15}N relaxation data was carried out following the procedure recommended by Palmer and coworkers[49] as recently described in detail[7]. The final model selections comprised models 2 and 5 for residues in domains 1 and 2, respectively, in E-P4. With the exception of residue U25 in domain 1 (model 1), the model selections for E-P4-Mg were also models 2 and 5 for residues in domains 1 and 2, respectively.

References

1. Kaye, N. M.; Zahler, N. H.; Christian, E. L.; Harris, M. E., Conservation of helical structure contributes to functional metal ion interactions in the catalytic domain of ribonuclease P RNA. *J. Mol. Biol.* **2002,** *324*, (3), 429-42.

2. Dingley, A. J.; Grzesiek, S., Direct observation of hydrogen bonds in nucleic acid base pairs by internucleotide $^{2}J_{NN}$ couplings. *J. Am. Chem. Soc.* **1998,** *120*, (33), 8293-8297.

3. Pervushin, K.; Ono, A.; Fernandez, C.; Szyperski, T.; Kainosho, M.; Wüthrich, K., NMR scalar couplings across Watson-Crick base pair hydrogen bonds in DNA observed by transverse relaxation-optimized spectroscopy. *Proc. Natl. Acad. Sci. USA* **1998,** *95*, (24), 14147-51.

4. Tolman, J. R.; Flanagan, J. M.; Kennedy, M. A.; Prestegard, J. H., Nuclear magnetic dipole interactions in field-oriented proteins - information for structure determination in solution. *Proc. Natl. Acad. Sci. USA* **1995,** *92*, (20), 9279-9283.

5. Tjandra, N.; Bax, A., Direct measurement of distances and angles in biomolecules by NMR in a dilute liquid crystalline medium. *Science* **1997,** *278*, (5340), 1111-1114.

6. Prestegard, J. H.; Al-Hashimi, H. M.; Tolman, J. R., NMR structures of biomolecules using field oriented media and residual dipolar couplings. *Quart. Rev. Biophys.* **2000,** *33*, (4), 371-424.

7. Zhang, Q.; Sun, X.; Watt, E. D.; Al-Hashimi, H. M., Resolving the motional modes that code for RNA adaptation. *Science* **2006,** *311*, (5761), 653-6.

8. Schmitz, M.; Tinoco, I. J., Solution structure and metal-ion binding of the P4 element from bacterial RNase P RNA. *RNA* **2000,** *6*, 1212-1225.

9. Fox, G. W.; Woese, C. R., 5S RNA secondary structure. *Nature* **1975,** *256*, (5517), 505-7.

10. Brown, J. W.; Nolan, J. M.; Haas, E. S.; Rubio, M. A.; Major, F.; Pace, N. R., Comparative analysis of ribonuclease P RNA using gene sequences from natural microbial populations reveals tertiary structural elements. *Proc Natl Acad Sci USA* **1996,** *93*, (7), 3001-6.

11. Pace, N. R.; Brown, J. W., Evolutionary perspective on the structure and function of ribonuclease P, a ribozyme. *J. Bacteriol.* **1995,** *177*, (8), 1919-28.

12. Haas, E. S.; Brown, J. W., Evolutionary variation in bacterial RNase P RNAs. *Nucleic Acids Res.* **1998,** *26*, (18), 4093-9.

13. Reich, C.; Gardiner, K. J.; Olsen, G. J.; Pace, B.; Marsh, T. L.; Pace, N. R., The RNA component of the Bacillus subtilis RNase P. Sequence, activity, and partial secondary structure. *J. Biol. Chem.* **1986,** *261*, (17), 7888-93.

14. Reed, R. E.; Baer, M. F.; Guerrier-Takada, C.; Donis-Keller, H.; Altman, S., Nucleotide sequence of the gene encoding the RNA subunit (M1 RNA) of ribonuclease P from Escherichia coli. *Cell* **1982,** *30*, (2), 627-36.

15. Haas, E. S.; Armbruster, D. W.; Vucson, B. M.; Daniels, C. J.; Brown, J. W., Comparative analysis of ribonuclease P RNA structure in Archaea. *Nucleic Acids Res.* **1996,** *24*, (7), 1252-9.

16. Altman, S.; Wesolowski, D.; Puranam, R. S., Nucleotide sequences of the RNA subunit of RNase P from several mammals. *Genomics* **1993,** *18*, (2), 418-22.

17. Chen, J. L.; Pace, N. R., Identification of the universally conserved core of ribonuclease P RNA. *RNA* **1997,** *3*, (6), 557-60.

18. Frank, D. N.; Adamidi, C.; Ehringer, M. A.; Pitulle, C.; Pace, N. R., Phylogenetic-comparative analysis of the eukaryal ribonuclease P RNA. *RNA* **2000,** *6*, (12), 1895-904.

19. Marquez, S. M.; Harris, J. K.; Kelley, S. T.; Brown, J. W.; Dawson, S. C.; Roberts, E. C.; Pace, N. R., Structural implications of novel diversity in eucaryal RNase P RNA. *RNA* **2005,** *11*, (5), 739-51.

20. Piccinelli, P.; Rosenblad, M. A.; Samuelsson, T., Identification and analysis of ribonuclease P and MRP RNA in a broad range of eukaryotes. *Nucleic Acids Res.* **2005,** *33*, (14), 4485-95.

21. Pitulle, C.; Garcia-Paris, M.; Zamudio, K. R.; Pace, N. R., Comparative structure analysis of vertebrate ribonuclease P RNA. *Nucleic Acids Res.* **1998,** *26*, (14), 3333-9.

22. Kazantsev, A. V.; Krivenko, A. A.; Harrington, D. J.; Holbrook, S. R.; Adams, P. D.; Pace, N. R., Crystal structure of a bacterial ribonuclease P RNA. *Proc. Natl. Acad. Sci. USA* **2005,** *102*, (38), 13392-13397.

23. Zuker, M., Mfold web server for nucleic acid folding and hybridization prediction. *Nucleic Acids Res.* **2003,** *31*, (13), 3406-15.

24. Gonzalez, R. L. J.; Tinoco, I. J., Solution structure and thermodynamics of a divalent metal ion binding site in an RNA pseudoknot. *J. Mol. Biol.* **1999,** *289*, 1267-1282.

25. Getz, M. M.; Andrews, A. J.; Fierke, C. A.; Al-Hashimi, H. M., Structural plasticity and Mg2+ binding properties of RNase P P4 from combined analysis of NMR residual dipolar couplings and motionally decoupled spin relaxation. *RNA* **2007,** *13*, 251-266.

26. Wüthrich, K., *NMR of Proteins and Nucleic Acids*. John Wiley and Sons: New York, 1986.

27. Sklenar, V.; Peterson, R. D.; Rejante, M. R.; Feigon, J., Two- and three-dimensional HCN experiments for correlating base and sugar resonances in $^{15}N,^{13}C$-labeled RNA oligonucleotides. *J. Biomol. NMR* **1993,** *3*, 721-7.

28. Rance, M.; Sørensen, O. W.; Bodenhausen, G.; Wagner, G.; Ernst, R. R.; Wüthrich, K., Improved spectral resolution in COSY ^{1}H NMR spectra of proteins via double quantum filtering. *Biochem. Biophys. Res. Commun.* **1983,** *117*, 479-485.

29. Dingley, A. J.; Masse, J. E.; Peterson, R. D.; Barfield, M.; Feigon, J.; Grzesiek, S., Internucleotide scalar couplings across hydrogen bonds in Watson-Crick and Hoogsteen base pairs of a DNA triplex. *J. Am. Chem. Soc.* **1999,** *121*, (25), 6019-6027.

30. Clore, G. M.; Starich, M. R.; Gronenborn, A. M., Measurement of residual dipolar couplings of macromolecules aligned in the nematic phase of a colloidal suspension of rod- shaped viruses. *J. Am. Chem. Soc.* **1998,** *120*, (40), 10571-10572.

31. Hansen, M. R.; Mueller, L.; Pardi, A., Tunable alignment of macromolecules by filamentous phage yields dipolar coupling interactions. *Nat. Struct. Biol.* **1998,** *5*, (12), 1065-1074.

32. Losonczi, J. A.; Andrec, M.; Fischer, M. W.; Prestegard, J. H., Order matrix analysis of residual dipolar couplings using singular value decomposition. *J. Magn. Reson.* **1999,** *138*, 334-342.

33. Tolman, J. R.; Al-Hashimi, H. M.; Kay, L. E.; Prestegard, J. H., Structural and dynamic analysis of residual dipolar coupling data for proteins. *J. Am. Chem. Soc.* **2001,** *123*, (7), 1416-1424.

34. Al-Hashimi, H. M.; Gosser, Y.; Gorin, A.; Hu, W.; Majumdar, A.; Patel, D. J., Concerted motions in HIV-1 TAR RNA may allow access to bound state conformations: RNA dynamics from NMR residual dipolar couplings. *J. Mol. Biol.* **2002,** *315*, (2), 95-102.

35. Ennifar, E.; Nikulin, A.; Tishchenko, S.; Serganov, A.; Nevskaya, N.; Garber, M.; Ehresmann, B.; Ehresmann, C.; Nikovov, S.; Dumas, P., The crystal structure of UUCG tetraloop. *J. Mol. Biol.* **2000,** *304*, 35-42.

36. Al-Hashimi, H. M.; Gorin, A.; Majumdar, A.; Gosser, Y.; Patel, D. J., Towards structural genomics of RNA: rapid NMR resonance assignment and simultaneous RNA tertiary structure determination using residual dipolar couplings. *J. Mol. Biol.* **2002,** *318*, 637-649.

37. Mollova, E. T.; Hansen, M. R.; Pardi, A., Global structure of RNA determined with residual dipolar couplings. *J. Am. Chem. Soc.* **2000,** *122*, (46), 11561-11562.

38. Sibille, N.; Pardi, A.; Simorre, J. P.; Blackledge, M., Refinement of local and long-range structural order in theophylline-binding RNA using ^{13}C-^{1}H residual dipolar

couplings and restrained molecular dynamics. *J. Am. Chem. Soc.* **2001,** *123*, 12135-12146.

39. Pitt, S. W.; Majumdar, A.; Serganov, A.; Patel, D. J.; Al-Hashimi, H. M., Argininamide binding arrests global motions in HIV-1 TAR RNA: Comparison with Mg^{2+} induced conformational stabilization. *J. Mol. Biol.* **2004,** *338*, 7-16.

40. Pitt, S. W.; Zhang, Q.; Patel, D. J.; Al-Hashimi, H. M., Evidence that electrostatic interactions dictate the ligand-induced arrest of RNA global flexibility. *Angew. Chem. Int. Ed. Engl* **2005,** *44*, 3412-5.

41. Hansen, A. L.; Al-Hashimi, H. M., Insight into the CSA tensors of nucleobase carbons in RNA polynucleotides from solution measurements of residual CSA: Towards new long-range orientational constraints. *J. Magn. Reson.* **2006,** *179*, 299-307.

42. Musselman, C.; Pitt, S. W.; Gulati, K.; Foster, L. L.; Andricioaei, I.; Al-Hashimi, H. M., Impact of static and dynamic A-form heterogeneity on the determination of RNA global structural dynamics using NMR residual dipolar couplings. *J. Biomol. NMR* **2006,** *36*, 235-249.

43. Zacharias, M.; Hagerman, P. J., Bulge-induced bends in RNA: quantification by transient electric birefringence. *J. Mol. Biol.* **1995,** *247*, (3), 486-500.

44. Tolman, J. R.; Flanagan, J. M.; Kennedy, M. A.; Prestegard, J. H., NMR evidence for slow collective motions in cyanometmyoglobin. *Nat. Struct. Biol.* **1997,** *4*, (4), 292-297.

45. Lipari, G.; Szabo, A., Model-free approach to the interpretation of nuclear magnetic resonance relaxation in macromolecules. 1. Theory and range of validity. *J. Am. Chem. Soc.* **1982,** *104*, 4546-4559.

46. Clore, G. M.; Szabo, A.; Bax, A.; Kay, L. E.; Driscoll, P. C.; Gronenborn, A. M., Deviations from the simple two-parameter model-free approach to the interpretation of nitrogen-15 nuclear magnetic relaxation of proteins. *J. Am. Chem. Soc.* **1990,** *112*, 4989 - 4991.

47. Vallurupalli, P.; Kay, L. E., A suite of ^{2}H NMR spin relaxation experiments for the measurement of RNA dynamics. *J. Am. Chem. Soc.* **2005,** *127*, 6893-6901.

48. Garcia de la Torre, J.; Huertas, M. L.; Carrasco, B., HYDRONMR: prediction of NMR relaxation of globular proteins from atomic-level structures and hydrodynamic calculations. *J. Magn. Reson.* **2000,** *147*, 138-146.

49. Mandel, A. M.; Akke, M.; Palmer, A. G., Backbone dynamics of *Escherichia coli* ribonuclease HI: correlations with structure and function in an active enzyme. *J. Mol. Biol.* **1995,** *246*, 144-163.

50. Bugayevskiy, L. M.; Snyder, J. P., *Map Projections: A Reference Manual*. Taylor & Francis: London, 1995.

51. Zacharias, M.; Hagerman, P. J., The influence of symmetric internal loops on the flexibility of RNA. *J. Mol. Biol.* **1996,** *257*, 276-289.

52. Williamson, J. R., Induced fit in RNA-protein recognition. *Nat. Struct. Biol.* **2000,** *7*, 834-7.

53. Leulliot, N.; Varani, G., Current topics in RNA-protein recognition: control of specificity and biological function through induced fit and conformational capture. *Biochemistry* **2001,** *40*, 7947-7956.

54. Al-Hashimi, H. M., Dynamics-based amplification of RNA function and its characterization by using NMR spectroscopy. *ChemBioChem* **2005,** *6*, 1506-1519.

55. Frank, D. N.; Pace, N. R., In vitro selection for altered divalent metal specificity in the RNase P RNA. *Proc. Natl. Acad. Sci. USA* **1997,** *94*, (26), 14355-60.

56. Hardt, W. D.; Warnecke, J. M.; Erdmann, V. A.; Hartmann, R. K., Rp-phosphorothioate modifications in RNase P RNA that interfere with tRNA binding. *EMBO J.* **1995,** *14*, (12), 2935-2944.

57. Christian, E. L.; Smith, K. M. J.; Perera, N.; Harris, M. E., The P4 metal binding site in RNase P RNA affects active site metal affinity through substrate positioning. *RNA* **2006,** *12*, 1463-7.

58. Tsai, H. Y.; Masquida, B.; Biswas, R.; Westhof, E.; Gopalan, V., Molecular modeling of the three-dimensional structure of the bacterial RNase P holoenzyme. *J. Mol. Biol.* **2003,** *325*, (4), 661-75.

59. Torres-Larios, A.; Swinger, K. K.; Krasilnikov, A. S.; Pan, T.; Mondragón, A., Crystal structure of the RNA component of bacterial ribonuclease P. *Nature* **2005,** *437*, (7058), 584-7.

60. Torres-Larios, A.; Swinger, K. K.; Pan, T.; Mondragon, A., Structure of ribonuclease P—a universal ribozyme. *Curr. Opin. Struct. Biol.* **2006,** *16*, 327-335.

61. Harris, M. E.; Pace, N. R., Identification of phosphates involved in catalysis by the ribozyme RNase P RNA. *RNA* **1995,** *1*, (2), 210-8.

62. Christian, E. L.; Kaye, N. M.; Harris, M. E., Helix P4 is a divalent metal ion binding site in the conserved core of the ribonuclease P ribozyme. *RNA* **2000,** *6*, 511-519.

63. Crary, S. M.; Kurz, J. C.; Fierke, C. A., Specific phosphorothioate substitutions probe the active site of *Bacillus subtilis* ribonuclease P. *RNA* **2002,** *8*, (7), 933-47.

64. Ghosh, S.; Joseph, S., Nonbridging phosphate oxygens in 16S rRNA important for 30S subunit assembly and association with the 50S ribosomal subunit. *RNA* **2005,** *11*, 657-667.

65. Serganov, A.; Polonskaia, A.; Phan, A. T.; Breaker, R. R.; Patel, D. J., Structural basis for gene regulation by a thiamine pyrophosphate-sensing riboswitch. *Nature* **2006,** *441*, 1167-1171.

66. Milligan, J. F.; Uhlenbeck, O. C., Synthesis of small RNAs using T7 RNA polymerase. *Methods Enzymol.* **1989,** *180*, 51-62.

67. Delaglio, F.; Grzesiek, S.; Vuister, G. W.; Zhu, G.; Pfeifer, J.; Bax, A., NMRPipe: a multidimensional spectral processing system based on UNIX pipes. *J. Biomol. NMR* **1995,** *6*, (3), 277-93.

68. Accelrys; Inc., *FELIX User Guide*. San Diego, CA, 2002.

69. Johnson, B. A.; Blevins, R. A., NMR View- A computer program for the visualization and analysis of NMR data. *J. Biomol. NMR* **1994,** *4*, (5), 603-614.

70. Goddard, T. D.; Kneller, D. G., *SPARKY 3*. University of California, San Franscisco: 2004.

71. Meissner, A.; Duus, J. O.; Sorensen, O. W., Spin-state-selective excitation. Application for E.COSY-type measurement of J_{HH} coupling constants. *J. Magn. Reson.* **1997,** *128*, 92-97.

72. Meissner, A.; Sorensen, O. W., The role of coherence transfer efficiency in design of TROSY-type multidimensional NMR experiments. *J. Magn. Reson.* **1999,** *139*, 439-442.

73. Palmer, A. G., NMR characterization of the dynamics of biomacromolecules. *Chem. Rev.* **2004,** *104*, 3623-3640.

74. Yip, G. N.; Zuiderweg, E. R., Improvement of duty-cycle heating compensation in NMR spin relaxation experiments. *J. Magn. Reson.* **2005,** *176*, 171-8.

75. Yip, G. N.; Zuiderweg, E. R., A phase cycle scheme that significantly suppresses offset-dependent artifacts in the R_2-CPMG ^{15}N relaxation experiment. *J. Magn. Reson.* **2004,** *171*, (1), 25-36.

76. Zweckstetter, M.; Hummer, G.; Bax, A., Prediction of charge-induced molecular alignment of biomolecules dissolved in dilute liquid-crystalline phases. *Biophys. J.* **2004,** *86*, 3444-60.

77. Zhang, Q.; Throolin, R.; Pitt, S. W.; Serganov, A.; Al-Hashimi, H. M., Probing motions between equivalent RNA domains using magnetic field induced residual dipolar couplings: accounting for correlations between motions and alignment. *J. Am. Chem. Soc.* **2003,** *125*, 10530-10531.

Chapter 3

Metal Binding Modes of P4[2]

Introduction

Our results from RDC and relaxation analysis of elongated P4 (Chapter 2) show that added Mg^{2+} ions have virtually no effect on the structure and dynamics of P4; the average inter-helical orientation remains the same and inter-helical motions, as detected by domain elongation and ^{15}N relaxation, persist along with the locally flexible uridine bulge. Here we examine the Mg^{2+} binding sites in P4 and determine the metal binding mode for the associated metals. The metal binding mode is relevant given that metals important for RNase P catalysis and folding are expected to have different binding modes (inner and outer sphere), as seen in other RNAs[1]. For example, early work with phosphorothioate substitution experiments[2-4] where activity was rescued with Mn^{2+} suggests the presence of inner sphere coordinated metals below the bulge in P4 which have roles in facilitating both substrate binding[2] and catalysis[3-5]. As mentioned previously, the exact roles of the metals bound in RNase P have yet to be determined. In particular, there is no direct evidence for the location of the catalytic metal(s). In addition to its applications with P4 of RNase P, distinguishing among these different modes of metal binding is a general biophysical problem that we sought to address using a combination of NMR methods.

[2] Magnesium results reproduced from Getz M.M., Andrews, A.J., Fierke, C.A., and Al-Hashimi, H.M., *RNA*, **2006**, *13*, 251-266. Magnesium binding affinity titration points were performed as suggested by Dr. Andrew J. Andrews.

In our approach, we first characterized the Mg^{2+} binding sites and their affinities for the stem-loop by chemical shift mapping experiments. One of the problems in interpreting chemical shift perturbations as sites for metal localization is that the observed shifts could arise due to changes in the RNA structure as a result of interactions with metals in other regions. In this regard, our ability to independently show that the metals do not induce major changes in the P4 structure using RDCs suggests that sites of chemical shift perturbations likely correspond to sites of metal localization. In addition, electrostatic calculations were used to determine if these proposed metal sites correspond to solvent accessible sites with negative electrostatic potential in P4 in the context of the RNA component of RNase P. To further localize the position of the metal binding site, we investigated Mn^{2+} binding due to its paramagnetic properties which induce line broadening in a distance dependent manner in the resonances located near the metal[6]. To distinguish outer from inner sphere binding sites in P4 we observed chemical shifts in P4 in the presence of two metals with unique modes of binding RNA: $Co(NH_3)_6^{3+}$ which can only form outer sphere interactions and Zn^{2+} which has a preference for forming inner sphere complexes. It has been shown that the two metal ions combined can functionally substitute for Mg^{2+} in RNase P (5 mM $Co(NH_3)_6^{3+}$, 20 mM Zn^{2+})[7]. RNase P has essentially no activity in the presence of $Co(NH_3)_6^{3+}$ while the activity in Zn^{2+} only is also decreased[7].

I. Mapping site-specific chemical shift changes and apparent dissociation constants of Mg^{2+}: Relation to electrostatic potential

To characterize the Mg^{2+} binding properties of P4, we recorded 2D HSQC spectra following incremental addition of Mg^{2+} up to 15 mM. The chemical shift differences in

increasing the Mg^{2+} from 10 to 15 mM are minimal indicating that the fraction occupancy of the metal site(s) are calculated to be > 90 %. Relative to previously published NMR chemical shift mapping data on the *E. coli* P4 stem-loop[8], we employed a lower background of monovalent ions (10 mM compared to 100 mM NaCl) and used a combination of N–H and C–H chemical shift probes. Consistent with the published data, our initial studies with 100 mM monovalent cations required > 30 mM $MgCl_2$ to induce significant chemical shift changes. Relatively small chemical shift perturbations were observed throughout P4 upon addition of 15 mM $MgCl_2$ to P4 in NMR buffer (10 mM sodium chloride, 10 mM sodium phosphate, pH 6.2); this behavior is indicative of nonspecific interactions with diffusive counterions. Large perturbations are observed for a small number of sites, one of which is A5 (Fig. 3-1A). Phosphorothioate rescue experiments have previously suggested that a catalytically important metal ion binds at this site in P RNA[3]. In the P4 helix we also observe Mg^{2+} association within a region above the bulge around the perturbed C8–G23 base pair (Figure 3-1A) in agreement with previous NMR Mg^{2+} mapping data[8]. Chemical shift perturbations report on changes in the chemical environment of an atom which can result from metal ion localization and/or local structural changes. In the case of P4, we have shown that the structure does not change upon addition of Mg^{2+}, suggesting no local structural changes. Note however that this does not include RDCs from the C8-G23 base pair, so Mg^{2+} induced structural changes cannot be ruled out at this site (although a $^{2h}J_{NN}$-COSY experiment[9, 10] revealed identical scalar couplings for hydrogen bonds in both free and Mg^{2+} bound forms of P4).

To obtain further insight into metal binding, we measured apparent K_d values by fitting the chemical shift titration data to a two-state binding model at each site (Figure 3-

1B)[11]. The apparent K_d values range between 0.7 and 7.3 mM. These values are on the same order of magnitude as measured previously for *E. coli* P4[8]; however, with the measurement of the chemical shift change at many different sites we were able to identify a broader range of K_ds (Figure 3-1B). The tightest Mg^{2+} affinity was measured at G22 (0.7 mM), followed by A5 (1.7 mM) and U27 (1-2 mM). The large range of K_d values suggests more than one binding site and likely reflects some diffusive interactions.

To aid interpretation of the chemical shift mapping data, we used the X-ray structure of *B. stearothermophilus* P4 from the 417-nt RNA component to compute the electrostatic potential surface employing the Delphi (Accelrys) module of Insight II (Molecular Simulations, Inc). Results revealed a strong surface accessible electrostatic potential precisely around residues exhibiting the largest Mg^{2+}-induced chemical shift perturbations and tight Mg^{2+} association, namely, residues A5, G22, and G23 above and below the bulge that reside together in the major groove of P4 (Figure 3-1C). The electrostatic potential for the same region is weaker for an idealized coaxial A-form helix containing the P4 sequence without the bulge (Figure 3-1C). Thus, the distortion in the inter-helical alignment and the C8–G23 base pair induced by the U7 bulge appear to promote formation of strong electrostatic potentials in regions where Mg^{2+} association is observed.

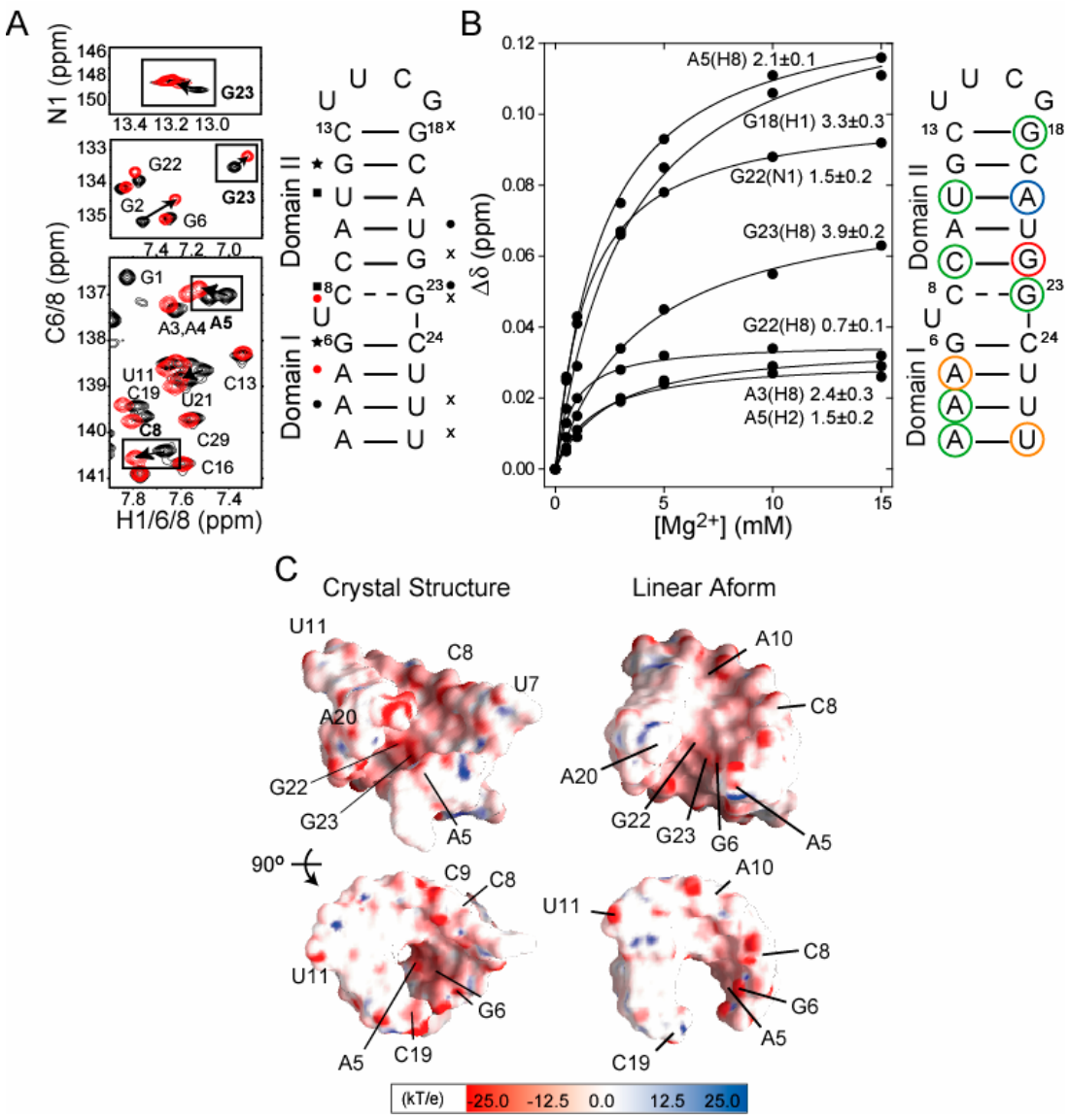

Figure 3-1. Mg^{2+} association with P4 and surface accessible potential maps. (A) Selected regions of 2D $^{13}C/^{15}N/^{1}H$ HSQC spectra of P4 in the presence (red) and absence (black) of 15 mM $MgCl_2$. Significant chemical shifts (> 0.08 ppm) are highlighted. Mg^{2+} induced chemical shift perturbations in P4 (> 0.08 ppm) observed for C6H6/C8H8 (circles), C5H5 (squares), C1'H1' (stars), and N1H1/N3H3 ("x"). The most significant changes across all vectors are in red. (B) Representative K_d curves for various sites in P4 (not all shown for clarity). Secondary structure showing K_ds; red < 1.0 mM, orange 1-2 mM, green 2-4 mM, and blue > 4 mM. Chemical shift mapping data were available in certain cases without corresponding K_ds because titration spectra were recorded with reduced resolution in the indirect dimension. (C) Left is the electrostatic surface representation (using the program GRASP) of P4 computed using the B-type crystal structure[12, 13] with negative and positive surfaces indicated in red and blue respectively (residue labels were changed to correspond to the P4 construct), right a coaxial A-form P4 helix lacking the bulged uridine generated in Insight II (Molecular Simulations, Inc.).

II. Probing P4 metal localization using Mn^{2+} paramagnetic line broadening

Since it was impossible to rule out that the chemical shift changes observed in Mg^{2+} are due to local structural changes, we sought to confirm sites of metal localization by a method that relies on detection of resonance linewidths/intensities rather than chemical shifts. Therefore we recorded spectra after addition of the paramagnetic metal Mn^{2+}, which causes broadening of resonances in a distance dependent (r^{-6}) manner[14]. 2D HSQC experiments were recorded on $^{13}C/^{15}N$ labeled P4 samples in the presence of 3 μM, 6 μM, 12 μM, 24 μM, and 60 μM Mn^{2+} which were added to NMR buffer (10 mM sodium chloride, 10 mM sodium phosphate, pH 6.2). The degree of line broadening was qualitatively computed from the 1- (I_M/ I_F) in which I_M and I_F are the resonance intensities observed in the presence and absence of Mn^{2+}. Increasing the concentration of Mn^{2+} (6 μM) resulted in a gradual increase in the line broadening at G22 and G23, which showed the greatest broadening of any resonance. These data likely represent a Mg^{2+} binding site. A secondary site appears at higher (12 μM) Mn^{2+} concentrations at residues A3-A5 and to a lesser extent G6 (Fig. 3-2A). These two groups of broadened resonances correspond to where the Mg^{2+} ions bind based on the chemical shift perturbations. Weak broadening was also observed at higher Mn^{2+} concentrations (60 μM) at residues C9, U11, U21, C24, U25, U26, and U27 which correspond to sites adjacent to the proposed binding sites that are as expected affected to a lesser extent by localization of the paramagnetic metal.

III. $Co(NH_3)_6^{3+}$/ Zn^{2+} induced chemical shift changes: Resolving inner from outer-sphere interactions

With the final goal of distinguishing inner from outer sphere metals and identifying their precise location, we conducted chemical shift titrations using either $Co(NH_3)_6^{3+}$ or Zn^{2+} or both. Further comparison of $Co(NH_3)_6^{3+}$ chemical shifts revealed two sites that initially suggested different binding modes for $Co(NH_3)_6^{3+}$ and Mg^{2+}.

Significantly less $Co(NH_3)_6^{3+}$ (0.5 mM) was needed compared to Mg^{2+} (15 mM) to induce similar magnitudes of chemical shift changes. This is expected since $Co(NH_3)_6^{3+}$ has a higher charge than Mg^{2+} [8]. While Mg^{2+} has two distinct binding regions, one above and one below the bulge, additionally $Co(NH_3)_6^{3+}$ induces shifts in a continuous region that includes both domains and the bulge in P4 (Fig. 3-3A,B). In order to determine if the mode of binding is different for Mg^{2+} and $Co(NH_3)_6^{3+}$, the directions of the chemical shift changes in the 2D HSQC spectra were carefully compared. Remarkably, the same sites where we observe the largest Mg^{2+} chemical shift perturbations and Mn^{2+} line broadening are the same sites that exhibit clear differences in the chemical shift directions, namely $A10_{C8H8}$, $G23_{C8H8}$, and $G23_{N1H1}$ (Fig. 3-3C). These results suggest different modes of metal binding at these sites. One possibility is that Mg^{2+} interacts at these sites via inner shell interactions that cannot be accomplished by $Co(NH_3)_6^{3+}$.

To test the above hypothesis, we examined if we could "rescue" the Mg^{2+} shifts by adding 1 mM Zn^{2+} to the P4-$Co(NH_3)_6^{3+}$ sample. The enzyme has been shown to be active under similar conditions[7] (1:4 $Co(NH_3)_6^{3+}$ to Zn^{2+}; Figure 3-4). Significant chemical shift changes are observed at a number of sites, including G23. Interestingly, a

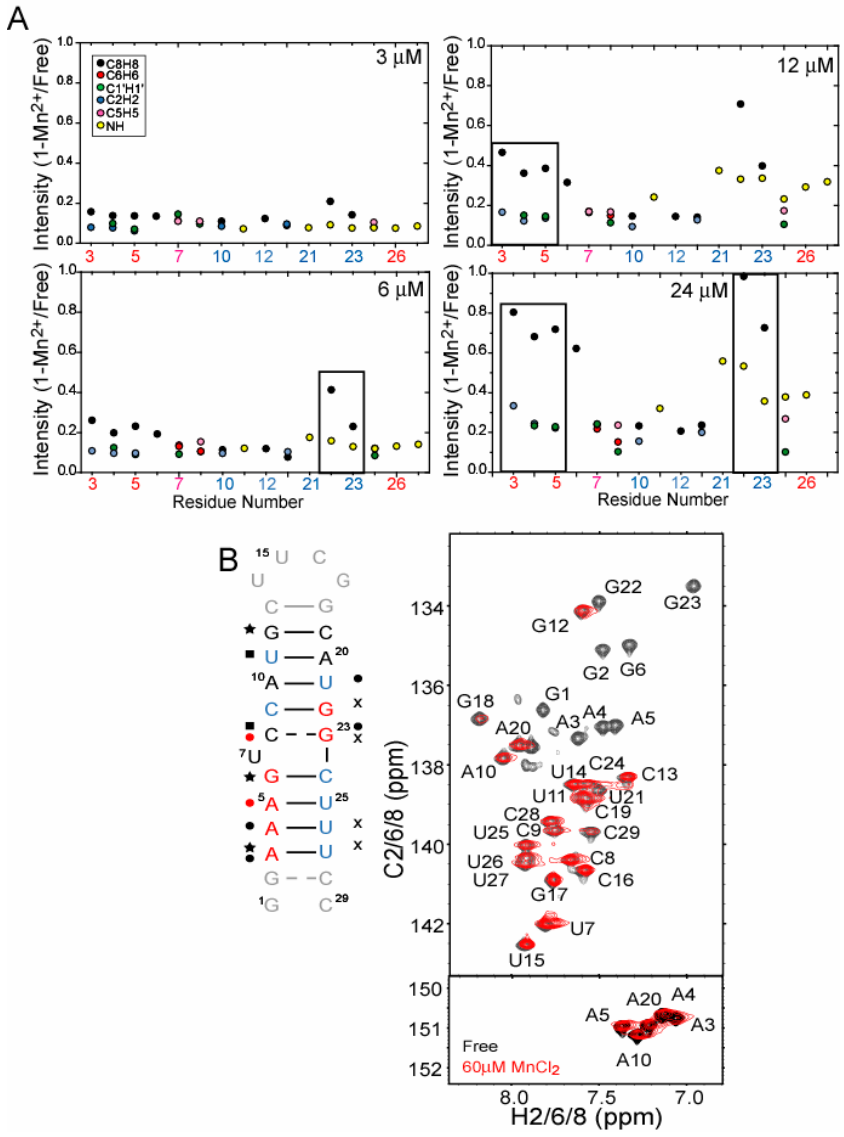

Figure 3-2. Metal localization in P4 detected by Mn^{2+}. (A) Normalized intensities (=1-I_M/I_F) of C8H8 (black), C6H6 (red), C1'H1' (green), C2H2 (blue), C5H5 (pink), and N1H1/N3H3 (yellow) atom pairs in 3 µM, 6 µM, 12 µM, and 24 µM Mn^{2+} as a function of residue number. The sites that are proposed Mg^{2+} binding sites are highlighted by black boxes. (B) Secondary structure of P4 construct showing the largest changes in chemical shift in 15 mM Mg^{2+} for the following atom pairs: C6H6/C8H8 (circles), C5H5 (squares), C1'H1' (stars), and N1H1/N3H3 ("x"). Red symbols indicate the largest chemical shift changes across all vectors. Also shown are peaks that were: not detectable (red) in 60 µM Mn^{2+}, reduced between 85 and 99 % reduction in intensity compared to without Mn^{2+} (blue) and unaffected residues (black). Residues in gray were excluded from the analysis. The aromatic region of a 2D HSQC experiment on the P4 construct both in the absence (black) and in the presence of 60 µM Mn^{2+} (red).

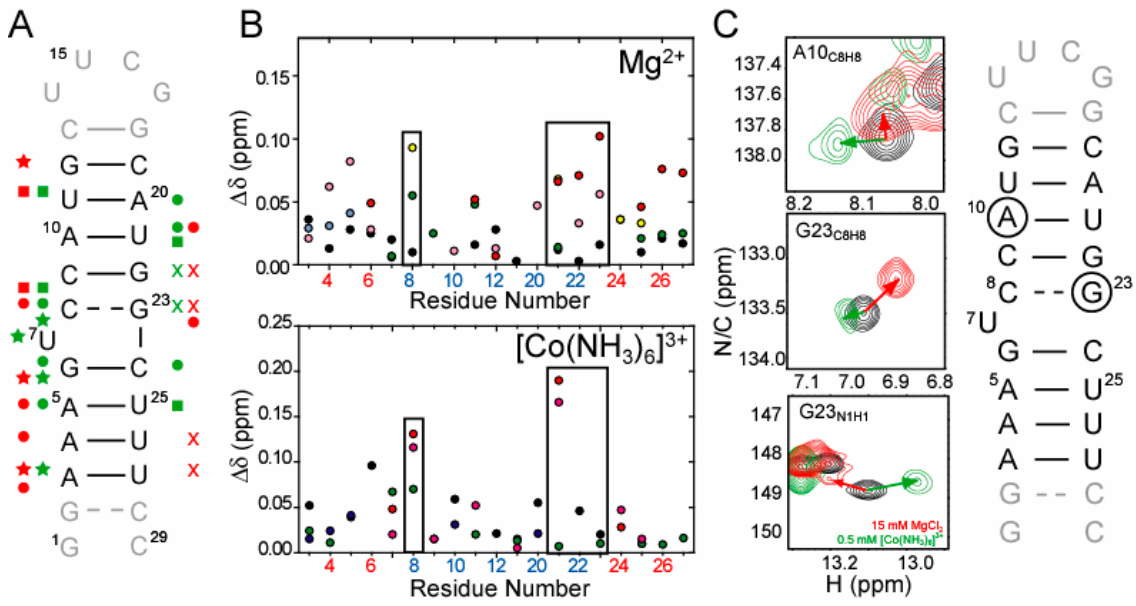

Figure 3-3. Comparison of Mg^{2+} and $Co(NH_3)_6^{3+}$ chemical shifts. (A) Secondary structure of P4 showing the sites of significant chemical shift changes in 15 mM Mg^{2+} (red, ~15:1) and 0.5 mM $Co(NH_3)_6^{3+}$ (green, ~5:1) for a variety of vectors: C8H8/C6H6 (circles), C5H5 (squares), C1'H1' (stars), N1H1/N3H3 ("x"). (B) Changes in chemical shift as a function of residue in P4 after adding Mg^{2+} and $Co(NH_3)_6^{3+}$. Significant changes are highlighted by black boxes; vectors measured are C8H8 (black), C6H6 (green), C1'H1' (red), C5H5 (blue) and C2H2 (pink). (C) Select sites are shown where the chemical shift environment is different in Mg^{2+} and $Co(NH_3)_6^{3+}$; shown are A10(C8H8), G23(C8H8), and G23 (N1H1) with 15 mM Mg^{2+} in red and 0.5 mM $Co(NH_3)_6^{3+}$ in green, as determined by 2D HSQC experiments. These sites are circled on the secondary structure of the P4 construct.

majority of the chemical shift changes upon addition of Zn^{2+} cause the peaks to shift back toward their "free" position, indicating that Zn^{2+} is displacing $Co(NH_3)_6^{3+}$ at these positions. At two sites, G23 (N1H1) and G22 (C8H8), the addition of Zn^{2+} causes chemical shift changes from a unique state in $Co(NH_3)_6^{3+}$ towards that observed in Mg^{2+} (Figure 3-4).

In order to determine where Zn^{2+} binds in the absence of $Co(NH_3)_6^{3+}$, 16 mM $ZnCl_2$ was added to a sample of 0.1 mM P4 RNA. In contrast to the many sites of change seen for Mg^{2+} and $Co(NH_3)_6^{3+}$, a majority of the peaks do not shift significantly upon

addition of Zn^{2+} with the exception of residue G22 which has > 0.05 ppm changes in chemical shifts (Fig. 3-4). These shifts in the nucleobase resonances are particularly

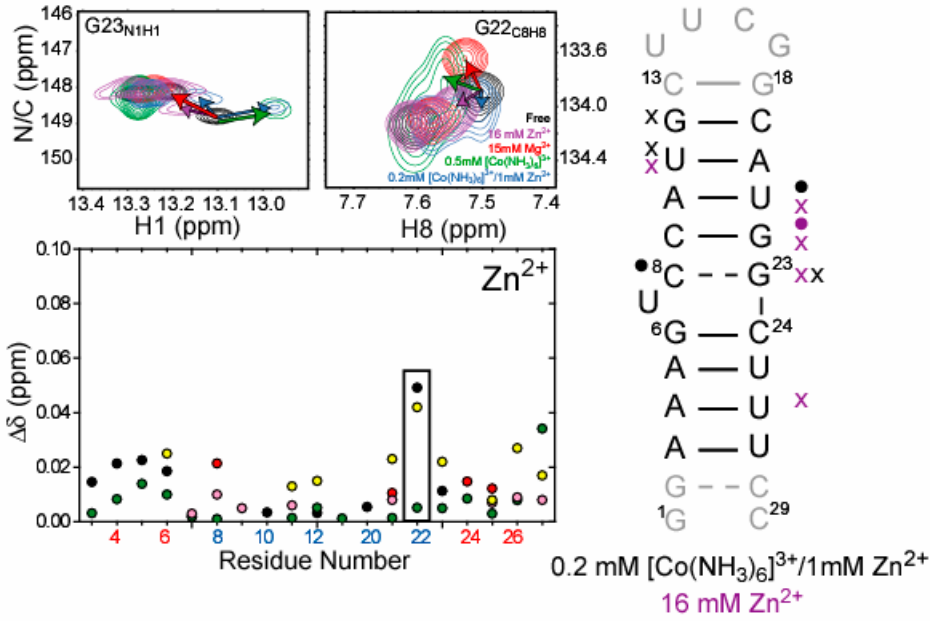

Figure 3-4. Detection of inner sphere binding sites in P4 in $Co(NH_3)_6^{3+}/Zn^{2+}$. Sites in P4 with unique chemical shift environments measured in 15 mM Mg^{2+} (red), 0.5 mM $Co(NH_3)_6^{3+}$ (green), 0.2 mM $Co(NH_3)_6^{3+}$/1 mM Zn^{2+} (blue), and 16 mM Zn^{2+} (purple). The chemical shift changes upon addition of 16 mM Zn^{2+} are shown as a function of residue number for the following vectors: C8H8 (black), C6H6 (green), C1'H1' (red), C5H5 (blue) and C2H2 (pink). Secondary structure of P4 showing the sites of significant (> 0.08 ppm) changes when 1 mM Zn^{2+} is added to 0.2 mM $Co(NH_3)_6^{3+}$ (black) and 16 mM Zn^{2+} (> 0.05 ppm) is added to free P4 (purple) for aromatic atom pairs (circles) and imino atom pairs ("x").

significant since they are close to the functional groups usually involved in metal binding, namely O6 and N7 in purines. Smaller changes are seen in the imino peaks of U11, U21, G23 and U26, perhaps due to secondary binding effects of neighboring residues (Fig. 3-4). In summary, the sites that shift the most in both $Co(NH_3)_6^{3+}/Zn^{2+}$ and Zn^{2+} alone are G22 and G23 suggesting inner sphere coordination at this site and outer sphere interactions at the adenine site below the bulge.

Discussion

We have shown by chemical shift titrations that Mg^{2+} binds P4 with high affinity primarily in two regions: G22-G23 (domain 2) and A3-A5 (domain 1). These sites form a region of solvent accessible high electrostatic potential in the distorted major groove of P4 (Fig. 3-1C). The interpretation of chemical shift changes in terms of Mg^{2+} binding was greatly aided by a control experiment in which we used RDCs to show that Mg^{2+} has small effects on the structural dynamics of P4. We have confirmed metal localization at these sites by Mn^{2+} dependent line broadening. Unique combinations of metals allowed us to probe outer and inner sphere modes of binding in P4. Slight changes in the direction of chemical shifts between Mg^{2+} and $Co(NH_3)_6^{3+}$ gave an initial hint of different binding modes at A10 and G23 in domain 2. Both chemical shift mapping upon addition of Zn^{2+} to $Co(NH_3)_6^{3+}$ and Zn^{2+} alone strongly suggest the existence of inner sphere binding at G22 and G23. This in turn allowed us to characterize the A3-A5 stretch in domain 1, previously highlighted as a Mg^{2+} binding site, as an outer sphere binding site.

The inner sphere binding region includes the tandem G22 and G23 aromatic bases. There are many examples of crystal structures of tandem purines binding divalent metals such as the leadzyme[15], hammerhead ribozyme[16], and the 50S subunit of the ribosome[17]. There are also a few examples of inner sphere metals binding tandem guanine residues[18-20]. For example, a crystal structure of the RNA from the human signal recognition particle shows a Mg^{2+} ion with coordination at two tandem guanines[20] (G19, and G20, Fig. 3-5). The structure was solved at 2.0 Å resolution in 100 mM $MgCl_2$, 50 mM MES (pH 5.5) and 15–20% (w/v) PEG 8000 (PDB ID#1D4R). This structure shows one visible inner sphere coordination to the N7 of G19 (~2.8 A) and other outer sphere

interactions with the O6 of G19 and the N7 and O6 of G20 through the four visible water molecules surrounding the metal. Such a mode of binding is consistent with our results in P4 which suggest at least one inner sphere binding site in the G22-G23 region. A working model contains a direct coordination of Mg^{2+} to the N7 of G22, based on the large chemical shift changes in Zn^{2+} in the C8H8 and N1H1 atom pairs, but other binding sites are possible such as the O6 in G22 and G23 about which no information was obtained in this study (Figure 3-5).

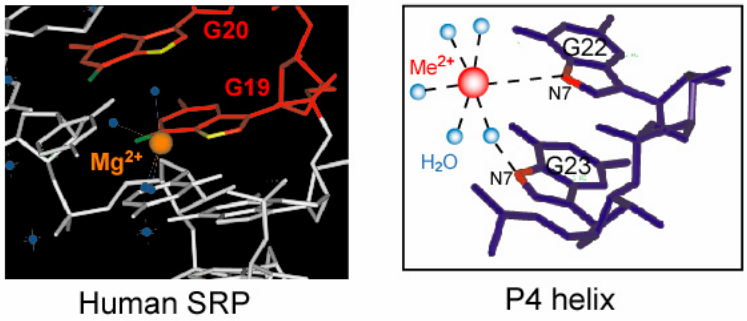

Figure 3-5. Inner sphere binding observed in SRP crystal structure and proposed in P4. Crystal structure of Human SRP at 2.0 Å resolution (100 mM $MgCl_2$, 50 mM MES (pH 5.5) and 15–20% (w/v) PEG 8000; PDB ID#1D4R) showing tandem guanine residues binding Mg^{2+} with inner and outer sphere coordination[20]. Proposed model of inner sphere binding with the bases of P4, an inner sphere contact in G22 and an outer sphere contact in G23.

We have seen that P4 has the potential to bind both outer and inner sphere metals which makes it a possible candidate for the catalytic metal site, based on the binding properties of the site deduced by biochemical data. By *in vitro* studies, it has been seen that $Co(NH_3)_6^{3+}$ inhibits the enzyme RNase P at high concentrations[21, 22] so it is expected that an inner sphere metal must bind perhaps in place of an outer sphere metal in order to initiate catalysis. It is possible that the $Co(NH_3)_6^{3+}$ which binds P4 is inhibitory, but can

be partially replaced with Zn^{2+} which has the potential to be a catalytic or co-catalytic metal. We propose that P4 and its highly conserved sequence of tandem G's could function as an inner sphere binding site in the enzyme or in the least, provide the site of an essential metal ion that mediates enzyme-substrate interactions, as proposed by Christian and co-workers[23]. Future studies of P4 in the context of the holoenzyme will determine once and for all if these discovered inner sphere binding sites remain in the holoenzyme.

Materials and Methods

NMR spectroscopy

Metal binding experiments were carried out on an Avance Bruker 600 MHz NMR spectrometer equipped with a triple-resonance 5 mm cryogenic probe at 298 K. Sample volumes of ~300 μL in Shigemi tubes were used in all experiments. 2D ^{13}C–^{1}H S^3E HSQC experiments[24-26] were used to monitor chemical shift changes with the following carrier frequencies: ^{1}H 4.69 ppm, $^{13}C1'$ 89.50 ppm, $^{13}C5$ 99.00 ppm, and ^{15}N 154 ppm. NMR spectra were processed using NMRPipe/NMRDraw[27] or Felix[28], analyzed using NMRView[29], and overlaid using SPARKY 3[30].

Detection of metal association by chemical shift mapping

Changes in chemical shift upon addition of Mg^{2+}, $Co(NH_3)_6^{3+}$, and Zn^{2+} were quantified using the equation $\Delta\delta = \sqrt{(\Delta\delta_H)^2 + (\alpha\Delta\delta_X)^2}$, where $\Delta\delta_H$ and $\Delta\delta_X$ are the changes in proton and carbon/nitrogen chemical shift and α is the ratio of the C/N and H gyromagnetic ratio. The most significant changes (> 0.08 ppm, using the above equation)

for each vector type are highlighted on the P4 secondary structure (Figure 3-1A, 3-2B, 3-3). The terminal residues were excluded from the analysis. To measure site-specific binding affinities of Mg^{2+} for P4, 2D HSQC spectra were recorded following incremental addition of $MgCl_2$ (0.5, 1, 3, 5, 10, and 15 mM). The apparent K_d values were obtained using the following equation[11]:

$$\delta_{obs} = \frac{\Delta\delta_T\{([Mg^{2+}]_T + [RNA]_T + K_d) - \sqrt{([Mg^{2+}]_T + [RNA]_T + K_d)^2 + (4[Mg^{2+}]_T[RNA]_T)}\}}{2[RNA]_T},$$

where δ_{obs} is the observed chemical shift, $\Delta\delta_T$ is the chemical shift difference between the free and fully bound state, $[Mg^{2+}]_T$ is the amount of added $MgCl_2$, and $[RNA]_T$ is the RNA concentration obtained from its absorbance at 260 nm. The data were fitted using Origin (Origin Lab Corp.) in which the unknown values $\Delta\delta_T$ and K_d are optimized during the fit (Figure 3-1B).

Mn^{2+} peak broadening

The intensity for each type of C–H and N-H spin measured in Mn^{2+} was normalized to = $1\text{-}I_M/I_F$ (M-Mn^{2+}, F-Free) so that a higher normalized value means a greater extent of peak broadening (identical experiments were used to record without and with Mn^{2+} so no other normalization was necessary, Figure 3-2A).

Structure-based electrostatic calculations

Residues 48–57 and 392–398 from the crystal structure of *B. stearothermophilus* RNase P[12] (PDB ID #2A64) were included in the electrostatic calculation (Fig. 3-1C). For calculations in a larger portion of RNase P the following residues were included: 44-

57, 253-255, 329-338, and 384-401 from the *B. stearothermophilus* crystal structure[12]. The nonlinear Poisson–Boltzmann equation was used to calculate the potential using the Delphi (Accelrys) module of Insight II (Molecular Simulations, Inc). The Debye–Huckel equation and full Coulombic boundary conditions were used to approximate the boundary potentials. Partial charges were obtained from the AMBER force field[31]. Input parameters for the calculations were as described previously[32]. A monovalent salt concentration of 0.01 M was used to match experimental conditions. The three-dimensional molecular surfaces (Fig. 3-1C) were displayed using GRASP, provided by the Honig laboratory[33] (http://honiglab.cpmc.columbia.edu).

References

1. Sigel, R. K.; Pyle, A. M., Alternative roles for metal ions in enzyme catalysis and the implications for ribozyme chemistry. *Chem. Rev.* **2007,** *107*, 97-113.

2. Hardt, W. D.; Warnecke, J. M.; Erdmann, V. A.; Hartmann, R. K., Rp-phosphorothioate modifications in RNase P RNA that interfere with tRNA binding. *EMBO J.* **1995,** *14*, (12), 2935-2944.

3. Harris, M. E.; Pace, N. R., Identification of phosphates involved in catalysis by the ribozyme RNase P RNA. *RNA* **1995,** *1*, (2), 210-8.

4. Crary, S. M.; Kurz, J. C.; Fierke, C. A., Specific phosphorothioate substitutions probe the active site of *Bacillus subtilis* ribonuclease P. *RNA* **2002,** *8*, (7), 933-47.

5. Christian, E. L.; Kaye, N. M.; Harris, M. E., Helix P4 is a divalent metal ion binding site in the conserved core of the ribonuclease P ribozyme. *RNA* **2000,** *6*, 511-519.

6. Butcher, S. E.; Allain, F. H.; Feigon, J., Determination of metal ion binding sites within the hairpin ribozyme domains by NMR. *Biochemistry* **2000,** *39*, 2174-82.

7. Cuzic, S.; Hartmann, R. K., Studies on *Escherichia coli* RNase P RNA with Zn^{2+} as the catalytic cofactor. *Nucleic Acids Res.* **2005,** *33*, 2464-2474.

8. Schmitz, M.; Tinoco, I. J., Solution structure and metal-ion binding of the P4 element from bacterial RNase P RNA. *RNA* **2000,** *6*, 1212-1225.

9. Pervushin, K.; Ono, A.; Fernandez, C.; Szyperski, T.; Kainosho, M.; Wüthrich, K., NMR scalar couplings across Watson-Crick base pair hydrogen bonds in DNA observed by transverse relaxation-optimized spectroscopy. *Proc. Natl. Acad. Sci. USA* **1998,** *95*, (24), 14147-51.

10. Dingley, A. J.; Grzesiek, S., Direct observation of hydrogen bonds in nucleic acid base pairs by internucleotide $^{2}J_{NN}$ couplings. *J. Am. Chem. Soc.* **1998,** *120*, (33), 8293-8297.

11. Gonzalez, R. L. J.; Tinoco, I. J., Solution structure and thermodynamics of a divalent metal ion binding site in an RNA pseudoknot. *J. Mol. Biol.* **1999,** *289*, 1267-1282.

12. Kazantsev, A. V.; Krivenko, A. A.; Harrington, D. J.; Holbrook, S. R.; Adams, P. D.; Pace, N. R., Crystal structure of a bacterial ribonuclease P RNA. *Proc. Natl. Acad. Sci. USA* **2005,** *102*, (38), 13392-13397.

13. Glemarec, C.; Kufel, J.; Foldesi, A.; Maltseva, T.; Sandstrom, A.; Kirsebom, L. A.; Chattopadhyaya, J., The NMR structure of 31mer RNA domain of *Escherichia coli* RNase P RNA using its non-uniformly deuterium labeled counterpart [the 'NMR-window' concept]. *Nucleic Acids Res.* **1996,** *24*, 2022-2035.

14. Bertini, I.; Luchinat, C., *NMR of Paramagnetic Molecules in Biological Systems*. Benjamin/Cummings: Menlo Park, CA, 1986.

15. Wedekind, J. E.; McKay, D. B., Crystal structure of the leadzyme at 1.8Å resolution: metal ion binding and the implications for catalytic mechanism and allo site ion regulation. *Biochemistry* **2003,** *42*, 9554-9563.

16. Markley, J. C.; Godde, F.; Sigurdsson, S. T., Identification and characterization of a divalent metal ion-dependent cleavage site in the hammerhead ribozyme. *Biochemistry* **2001,** *40*, 13849-13856.

17. Klein, D. J.; Moore, P. B.; Steitz, T. A., The roles of ribosomal proteins in the structure assembly, and evolution of the large ribosomal subunit. *J. Mol. Biol.* **2004,** *340*, 141-177.

18. Cate, J. H.; Gooding, A. R.; Podell, E.; Zhou, K.; Golden, B. L.; Szewczak, A. A.; Kundrot, C. E.; Cech, T. R.; Doudna, J. A., RNA tertiary structure mediation by adenosine platforms. *Science* **1996,** *273*, (5282), 1696-9.

19. Wimberly, B. T.; Brodersen, D. E.; Clemons, W. M. J.; Morgan-Warren, R. J.; Carter, A. P.; Vonrhein, C.; Hartsch, T.; Ramakrishnan, V., Structure of the 30S ribosomal subunit. *Nature* **2000,** *407*, 327-339.

20. Wild, K.; Weichenrieder, O.; Leonard, G. A.; Cusack, S., The 2 A structure of helix 6 of the human signal recognition particle RNA. *Structure* **1999,** *7*, (11), 1345-52.

21. Guerrier-Takada, C.; Haydock, K.; Allen, L.; Altman, S., Metal ion requirements and other aspects of the reaction catalyzed by M1 RNA, the RNA subunit of ribonuclease P from *Escherichia coli*. *Biochemistry* **1986,** *25*, 1509-15.

22. Brannvall, M.; Kirsebom, L. A., Metal ion cooperativity in ribozyme cleavage of RNA. *Proc. Natl. Acad. Sci. USA* **2001,** *98*, (23), 12943-7.

23. Christian, E. L.; Smith, K. M. J.; Perera, N.; Harris, M. E., The P4 metal binding site in RNase P RNA affects active site metal affinity through substrate positioning. *RNA* **2006,** *12*, 1463-7.

24. Meissner, A.; Sorensen, O. W., The role of coherence transfer efficiency in design of TROSY-type multidimensional NMR experiments. *J. Magn. Reson.* **1999,** *139*, 439-442.

25. Pitt, S. W.; Zhang, Q.; Patel, D. J.; Al-Hashimi, H. M., Evidence that electrostatic interactions dictate the ligand-induced arrest of RNA global flexibility. *Angew. Chem. Int. Ed. Engl.* **2005,** *44*, 3412-5.

26. Meissner, A.; Duus, J. O.; Sorensen, O. W., Spin-state-selective excitation. Application for E.COSY-type measurement of J_{HH} coupling constants. *J. Magn. Reson.* **1997,** *128*, 92-97.

27. Delaglio, F.; Grzesiek, S.; Vuister, G. W.; Zhu, G.; Pfeifer, J.; Bax, A., NMRPipe: a multidimensional spectral processing system based on UNIX pipes. *J. Biomol. NMR* **1995,** *6*, (3), 277-93.

28. Accelrys; Inc., *FELIX User Guide*. San Diego, CA, 2002.

29. Johnson, B. A.; Blevins, R. A., NMR View- A computer program for the visualization and analysis of NMR data. *J. Biomol. NMR* **1994,** *4*, (5), 603-614.

30. Goddard, T. D.; Kneller, D. G., *SPARKY 3*. University of California, San Franscisco: 2004.

31. Cornell, W. D.; Cieplak, P.; Bayly, C. I.; Gould, I. R.; Merz, K. M.; Ferguson, D. M.; Spellmeyer, D. C.; Fox, T.; Caldwell, J. W.; Kollman, P. A., A second generation force field for the simulation of proteins, nucleic acids, and organic molecules. *J. Am. Chem. Soc.* **1995,** *117*, 5179 - 5197.

32. Chin, K.; Sharp, K.; Honig, B.; Pyle, A., Calculating the electrostatic properties of RNA provides new insights into molecular interactions and function. *Nat. Struct. Biol.* **1999,** *6*, 1055-1061.

33. Nicholls, A.; Sharp, K.; Honig, B., Protein folding and association: insights from the interfacial and thermodynamic properties of hydrocarbons. *Proteins* **1991,** *11*, 281-296.

Chapter 4

Structure, dynamics, and metal binding of $P4_{G8C23}$ by NMR[3]

I. Introduction

Our results in Chapters 2 and 3 suggest that the weakly hydrogen bonded C8-G23 base-pair above the bulge is an important determinant of the structural, dynamical and metal binding properties of P4. To test the importance of this base-pair, we examined the conformational and metal binding behavior of a P4 mutant ($P4_{G8C23}$) in which the C8-G23 base-pair was replaced with a G8-C23 counterpart. This mutant allows us to test the hypotheses that the specific sequence flanking the P4 bulge codes for specific structural dynamics and metal binding properties. The first goal was to determine to what extent the weaker hydrogen bond alignment of the C8-G23 base-pair was the consequence of the specific sequence of Watson-Crick base-pairs flanking the bulge and further, to assess how potential changes in the hydrogen bond alignment of these flanking base-pairs may affect the resultant local and global P4 structural dynamics. The second aim was to test the hypothesis that the tandem guanines G22 and G23 in P4 are required for metal binding. To relate these findings to function, the effects of this mutation on the catalytic rate of the holoenzyme RNase P were measured by *in vitro* assays.

[3] *In vitro* activity assays for *B. subtilis* RNase P of wild-type, single, and double mutant forms were performed by Dr. Andrew J. Andrews. Dr. John Hsieh supplied T7 polymerase used for RNA synthesis.

II. Resonance assignment and hydrogen bond alignment

The NMR characterization of $P4_{G8C23}$ was initially carried out in the absence of divalent ions using the same buffer conditions used to characterize P4 (10 mM sodium

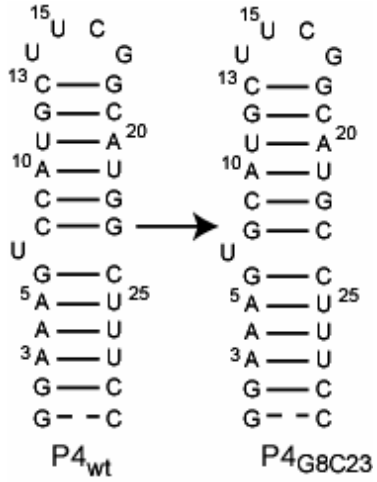

Figure 4-1. RNA sequence of *B. subtilis* P4 and $P4_{G8C23}$ constructs for NMR studies.

chloride, 10 mM sodium phosphate, pH ~6.2). An overlay of the 2D HSQC spectra of $P4_{G8C23}$ onto those of P4 revealed significant chemical shift differences. This indicated that the mutation had a significant effect on the P4 conformation and thus the resonance assignments had to be carried out independently using the same approach outlined for P4. Following resonance assignment, comparison of chemical shifts yielded insights into the structural and dynamical differences between P4 and $P4_{G8C23}$. Residues up to two base pairs away from the site of mutation show significant chemical shift differences, including the bulge residue, the base pair flanking the bulge on the 3' end, and A10 and U21 (> 0.05 ppm; Fig. 4-2). These are fairly large changes span a relatively large region of P4, which indicates that a simple base flip could have a dramatic effect on conformational dynamics.

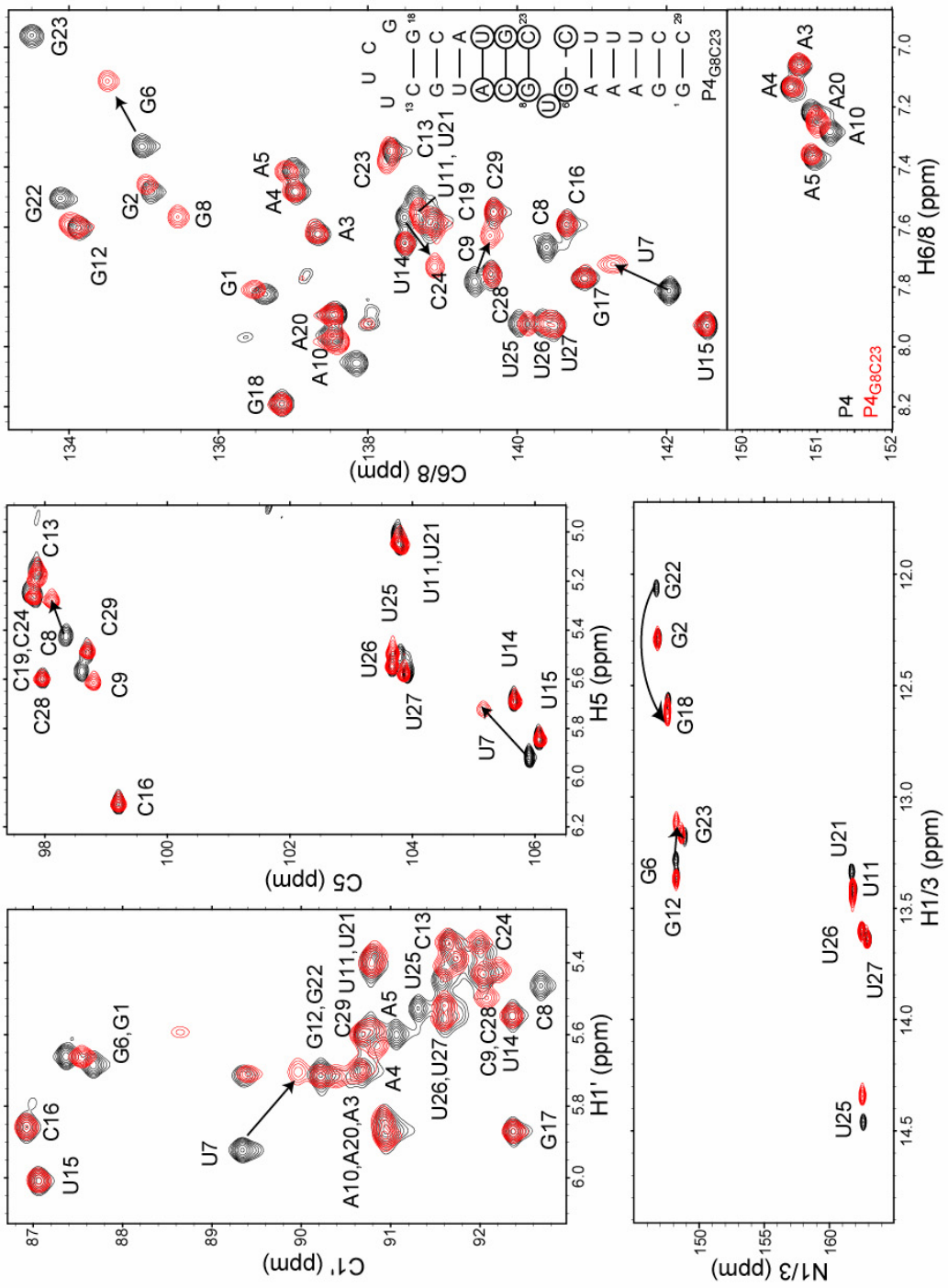

Figure 4-2. Resonance assignments of $P4_{G8C23}$ and comparison of chemical shifts with P4. Shown are 2D HSQC spectra for the aromatic (C6H6, C8H8, and C2H2), C5H5, N1H1-N3H3, and C1'H1' regions. Inset: circled residues are those that demonstrate significant (> 0.05 ppm) chemical shift differences from P4.

As in P4, the NOE walk[1] for nonexchangeable protons was uninterrupted from A3 to C13, and also from G18 to U25, which indicated a continuous helical conformation (Fig. 4-3A). Unlike P4, the NOE walk on this mutant construct continued through the bulge residue U7 indicating that this base adopts an A-form like geometry at least some of the time. Unlike P4, the U7 cross peaks in $P4_{G8C23}$ are also exchange broadened, suggesting slow μs-ms dynamics at the bulge. Peak assignments from the NOE walk were confirmed using an HCN experiment which allowed direct correlation of the H6/H8 resonance in the base to the H1' resonance in the same residue[2] (Fig. 4-3B).

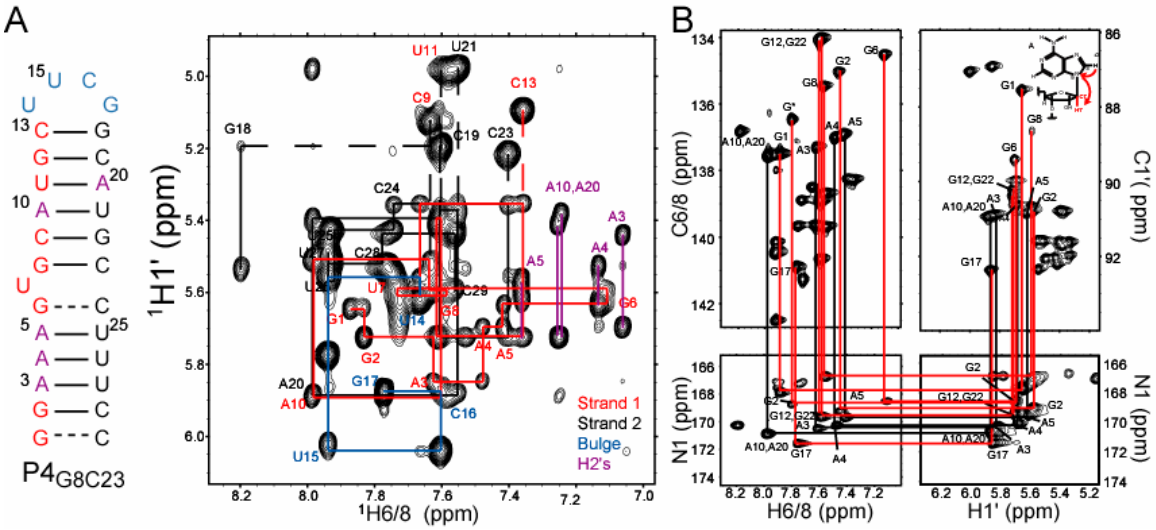

Figure 4-3. Resonance assignment of $P4_{G8C23}$. (A) 2D non-exchangeable NOESY showing intra and inter-residue cross-peaks which connect H1' and H6/H8 as well as H2. (B) 2D HCN experiment shown as two spectra and their corresponding HSQC spectra of aromatic and C1'H1' regions. The two lower spectra show intra-residue aromatic to N1 atoms and N1 to C1'H1' respectively for purine residues (pyrimidine region not shown).

The hydrogen bond alignment of $P4_{G8C23}$ as determined by $^{2h}J_{NN}$-COSY experiment (Fig. 4-4)[3, 4] was very different from P4 around the bulge region. In P4 the C8-G23 base-pair above the bulge deviates from ideality to a greater extent compared to

other G-C/C-G base pairs. In contrast, in $P4_{G8C23}$, an anomalous hydrogen bond is observed for the G6-C24 base pair below the bulge as judged by the weak auto and cross peaks (Fig. 4-4). This shows that the simple C-G to G-C flip causes an interchange in the stability/ideality of Watson-Crick base-pairs flanking the bulge. This and the changes in chemical shift were the first signs that this mutation may have significant effects on the conformation of P4.

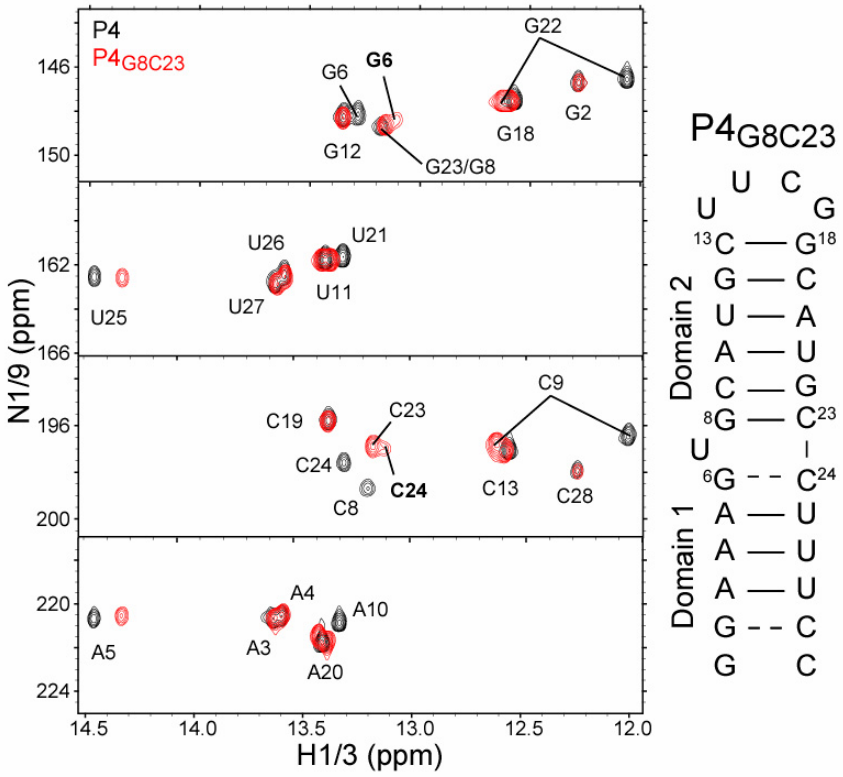

Figure 4-4. Hydrogen bond alignment in $P4_{G8C23}$. 2D $^{2h}J_{NN}$-COSY experiment showing auto peaks of hydrogen bond donors and cross peaks of hydrogen bond acceptors in $P4_{G8C23}$ (red) and the corresponding secondary structure, and peaks for P4 (black).

III. Mg^{2+} binding localization and apparent dissociation constants in $P4_{G8C23}$

To examine the impact of the mutation on the Mg^{2+} binding properties of P4, we recorded 2D HSQC spectra of $P4_{G8C23}$ following Mg^{2+} titration up to 15 mM

concentration. While some sites in $P4_{G8C23}$ exhibited similar response to Mg^{2+} perturbations as those of P4, such as A5 and neighboring residues, differences were also observed, with the most notable being the magnesium dependence of the chemical shifts of the bulge residue U7 and a nearby residue C9 (Fig. 4-5A). Overall, the K_d values observed for $P4_{G8C23}$ (0.05 to 3.0 mM) are lower and less variable than K_d values for P4 (0.7 to 7.3 mM). The locations for the highest affinity binding site in $P4_{G8C23}$ are residues A5, G6, C9, and C24-U26, all but one of which are in domain 1 (Fig. 4-5B). This is in contrast to P4 where the highest affinity binding site (smallest K_d value) is located in domain 2, G22. Comparison was not possible due to spectral overlap in $P4_{G8C23}$ for G22 N1H1 and other resonances in domain 2. Overall, the Mg^{2+} perturbations suggest that this mutation alters the metal binding mode and/or the effects of the metal on the P4 structural dynamics.

IV. Structural dynamics in the absence and presence of Mg^{2+} by RDCs

To examine if and how the mutation affects the P4 conformation, we used an RDC order tensor analysis to characterize the conformational dynamics of $P4_{G8C23}$. Comparison of one bond RDCs [C1'H1', C2H2, C5H5, C6H6, C8H8, N1H1, and N3H3] measured in the absence of divalent ions using 15 mg/mL of Pf1-phage[5-8] provided qualitative insight into the effects of the mutation. As expected from a pseudo-continuous helical conformation, RDCs measured for a given type of vector fall within a relatively narrow range (Fig. 4-6A). The small RDCs observed in the terminal residues reflect dynamical averaging due to end fraying. As in P4, all three sites measured in the bulged U7 show much smaller RDCs (near zero values) in both the base and sugar moieties (Fig.

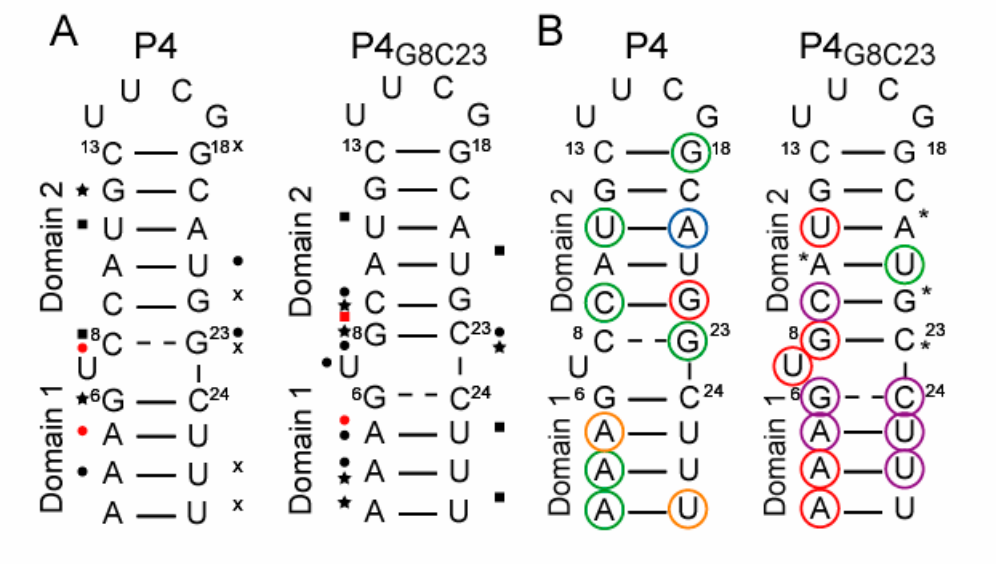

Figure 4-5. Comparison of Mg^{2+} binding localization and affinity of $P4_{G8C23}$ with P4. (A) Significant chemical shift changes (> 0.08 ppm) in 15 mM Mg^{2+} shown on P4 secondary structures where the red symbols indicate largest shifts across all vectors: C8H8/C6H6 (circles), C5H5 (squares), C1'H1' (stars), and N1H1/N3H3 ("x"). (B) Binding affinity (represented as K_d) of Mg^{2+} to P4 and $P4_{G8C23}$ where tightest binding sites are circled for wild type P4: < 1 mM (red), 1 to 2 mM (orange), 2 to 4 mM (green), > 4 mM (blue) and $P4_{G8C23}$: < 0.5 mM (purple), 0.7 to 1.0 mM (red), 2 to 4 mM (green). Astericks indicate residues for which peak overlap prevented analysis.

4-6A). Though an unusual static conformation (such as an orientatation along the magic angle) could not be ruled out, these attenuated RDCs suggested a high degree of local mobility at U7 occurring at sub-millisecond timescales.

The relative orientation and dynamics of the two $P4_{G8C23}$ helical domains was determined in the absence of divalent ions by subjecting RDCs measured in non-terminal residues to an order tensor analysis as was done for P4 in Chapter 2[9-11]. Shown in Figure 4-6B is the correlation between measured and back-calculated RDCs (15 for each domain) when independently fitting each domain to an order tensor using an idealized A-form helix geometry (Table 4.1). A very good fit is observed with the root-mean-square deviation (RMSD = 1.1 and 2.7 Hz for domains 1 and 2/loop, respectively) approaching

the RDC measurement uncertainty (2.4 Hz) estimated from duplicate measurements[12]. Again, for $P4_{G8C23}$, the targeted Watson–Crick residues in the two domains adopt the expected local A-form helix geometry. The C8-G23 base pair that was perturbed in P4, i.e. had large deviations between measured and back-calculated RDC values (RMSD > 9.0 Hz) no longer has large deviations in $P4_{G8C23}$ (RMSD < 4 Hz). Small deviations (~ 4 Hz) are observed between the measured and back-calculated values for G6 C8H8 and C24 C6H6, suggesting only small deviations from the A-form geometry (Fig. 4-6B).

The order tensor analysis of RDCs was used to determine the average inter-helical orientation in $P4_{G8C23}$ as was done for P4. The average global structure was nearly identical to P4. The inter-helical bend (10° ± 5°) and twist (-6° to 54°) angles compared favorably to those of P4 (10° ± 5° and -15° to 25°, respectively). The comparison of order tensor solutions for P4 and $P4_{G8C23}$ is illustrated in Figure 4-6C, where the domain 1 (red) and 2 (blue) order tensor frames are depicted relative to the free P4 inter-helical alignment. The very good overlap indicates that the two RNAs share a very similar global structure though our results do not rule out the presence of some differences in the average inter-helical twisting.

While the average global structures of P4 and $P4_{G8C23}$ are similar, their inter-helical motional amplitudes appear to be different. In P4, the ϑ value obtained for domain 2 (1.25×10^{-3} ± 8%) was smaller than that obtained for domain 1 (1.35×10^{-3} ± 3%), in $P4_{G8C23}$, on the other hand, domain 2 dominates alignment with a ϑ of 1.23×10^{-3} ± 2% while domain 1 has a ϑ of 0.98×10^{-3} ± 2%. To verify the $P4_{G8C23}$ results, we repeated the order tensor determination after randomly removing RDC data from the input pool. The resulting data still consistently show the same trend (Fig. 4-6D). Thus it appears that the

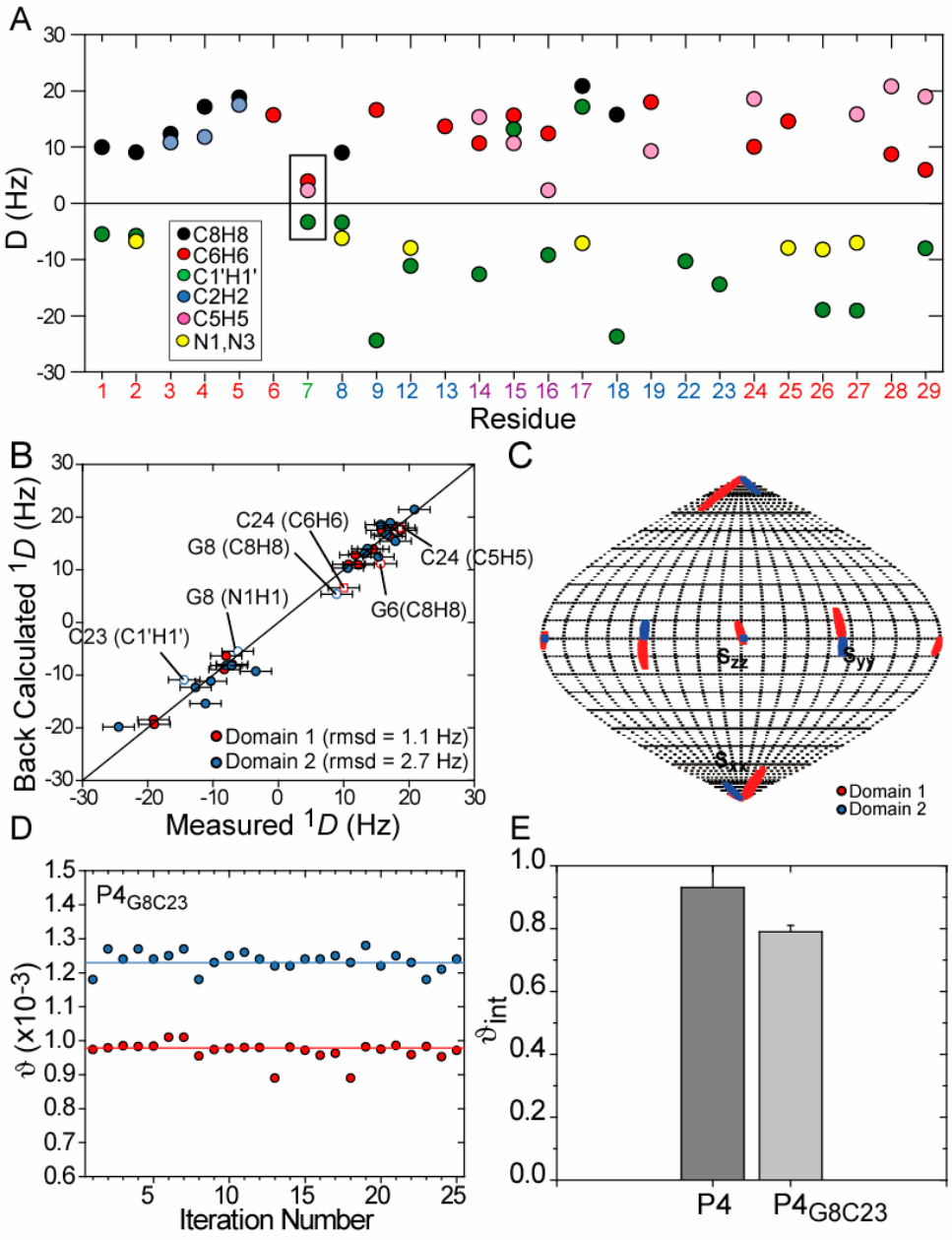

Figure 4-6. RDC order tensor analysis of $P4_{G8C23}$ in the absence of Mg^{2+}. (A) RDCs as a function of residue for $P4_{G8C23}$ in 15 mg/mL Pf1 phage for a variety of vectors: C8H8 (black), C6H6 (red), C1'H1' (green), C5H5 (pink), C2H2 (blue), and N1H1/N3H3 (yellow). (B) Back-calculated RDCs from the best-fit order tensor as determined by SVD as a function of measured RDCs for domain 1 (red) and 2 (blue) with RMSD's of 1.1 and 2.7 Hz respectively. (C) Top 10 % of solutions for $P4_{G8C23}$ RDCs fit to P4 structure shown on a Sanson-Flamsteed map for domain 1 (red) and domain 2 (blue). (D) ϑ output as a function of included RDCs as performed in Chapter 2. Shown are domain 1 (red) and domain 2 (blue). (E) ϑ_{int} comparison for P4 (dark grey) and $P4_{G8C23}$ (light grey).

Table 4.1 Measured and back-calculated RDCs for $P4_{G8C23}$. Back-calculated values are from the best-fit order tensor obtained from an in-house modified version of SVD.

	Domain 1	
	Meas. (Hz)	Pred. (Hz)
3 C2H2	10.7	11.0
3 C8H8	12.3	10.9
27 C1'H1'	-19.1	-18.5
27 C5H5	15.8	17.5
27 N3H3	-7.1	-7.9
4 C2H2	11.8	12.8
4 C8H8	17.1	16.4
26 C1'H1'	-19.0	-19.3
26 N3H3	-8.3	-8.9
5 C2H2	17.5	18.3
5 C8H8	18.8	17.5
25 C6H6	14.5	13.9
25 N3H3	-8.0	-6.4

	Domain 2	
	Meas. (Hz)	Pred. (Hz)
9 C1'H1'	-24.5	-23.6
9 C6H6	16.6	18.3
22 C1'H1'	-10.3	-8.8
12 C1'H1'	-11.2	-13.1
12 N1H1	-8.0	-8.5
19 C6H6	17.9	16.1
13 C6H6	13.6	13.7
18 C8H8	15.7	18.1
14 C1'H1'	-12.7	-10.9
14 C5H5	15.3	12.9
14 C6H6	10.6	9.4
15 C1'H1'	13.2	11.5
17 C1'H1'	17.1	18.4
17 C8H8	20.8	21.4
17 N1H1	-7.1	-8.2

domain which aligns less strongly is the one that contains the weaker base-pair flanking the bulge; domain 2 in P4 and domain 1 in $P4_{G8C23}$. This is as expected if the center of mass and/or pivot point of motion is located in the weaker junctional base-pair.

In $P4_{G8C23}$, the ϑ_{int} value was smaller (0.79 ±0.02) compared to P4 (0.93 ±0.08) which means a greater amplitude of motion for $P4_{G8C23}$, on the order of ~32° compared to P4's ~18°, assuming isotropic motions in a cone[11, 13] (Fig. 4-6E). Since the domains are similar in size, any change in the motional coupling between the two domains could cause different amplitudes of motion and thus the difference in motional amplitudes observed should be treated cautiously. Nevertheless, it is remarkable that a single C-G to G-C base pair flip changed the preference for domain alignment, supporting the idea that the sequence identity of base pairs flanking bulges is a critical determinant of structural flexibility.

In order to determine if and how Mg^{2+} affects the $P4_{G8C23}$ structural dynamics, we repeated the NMR characterization by RDC analysis in the presence of 20 mM Mg^{2+}. Results are summarized in Figure 4-7 and RDCs are listed in Table 4.2. The U7 bulge is still dynamic in the presence of Mg^{2+} in $P4_{G8C23}$ as was seen by attenuated RDC values (Fig. 4-7A), with little change in the relative orientation of domains. The average inter-helical alignment obtained from the RDCs measured in Mg^{2+} (inter-helical bend and twist angles of 12° ± 5° and 2° to 62°) was virtually identical to that obtained in the absence of Mg^{2+} (inter-helical bend and twist angles of 10° ± 5° and bend -6° to 54°, respectively). The domain 1 and 2 Mg^{2+} order tensor frames of $P4_{G8C23}$ are depicted relative to Mg^{2+} P4 (Fig. 4-7B). Again, very good overlap was observed.

Table 4.2 Measured and back-calculated RDCs for $P4_{G8C23}$ in 20 mM $MgCl_2$.

	Domain 1			Domain 2	
	Meas. (Hz)	Pred. (Hz)		Meas. (Hz)	Pred. (Hz)
5 (C2H2)	10.6	13.5	10 (C8H8)	16.4	19.1
4 (C2H2)	8.5	9.7	12 (N1H1)	-5.2	-5.9
3 (C2H2)	8.4	8.7	9 (C6H6)	20.9	18.5
5 (C1'H1')	-21.8	-21.9	19 (C6H6)	9.4	11.4
26 (C1'H1')	-14.5	-13.4	9 (C1'H1')	-18.4	-15.0
27 (C1'H1')	-18.6	-19.1	14 (C5H5)	11.4	9.9
4 (C8H8)	14.8	11.0	17 (C1'H1')	12.4	12.1
5 (C8H8)	13.0	12.1	18 (C8H8)	14.2	16.8
25 (C6H6)	9.1	11.1	17 (C8H8)	14.8	13.4
26 (C5H5)	12.6	11.1	13 (C1'H1')	-7.3	-7.0
25 (C5H5)	15.1	14.1	8 (C1'H1')	-11.8	-12.6
27 (C5H5)	14.0	14.2	23 (C1'H1')	-7.3	-7.0
27 (N3H3)	-4.7	-5.4	23 (C6H6)	15.7	15.5
26 (N3H3)	-5.6	-6.2	8 (C8H8)	13.3	9.6
25 (N3H3)	-6.0	-5.0	15 (C1'H1')	9.2	12.9

In contrast, the same order tensor analysis yields a ratio between degree of alignment for the two domains (ϑ_{int} = 0.98 ± 11%) in Mg^{2+}, which is larger than that observed in the absence of Mg^{2+} (ϑ_{int} = 0.79 ± 2%). Thus, unlike P4, in which domain

motions persist even in the presence of Mg^{2+}, the binding of Mg^{2+} to $P4_{G8C23}$ seems to arrest the inter-helical motions (Fig. 4-7C,D). Although, as mentioned previously, identical ϑ values for two domains implies that each domain has a similar degree of alignment, it does not rule out symmetric motions, i.e. identical amplitudes of motion for each domain.

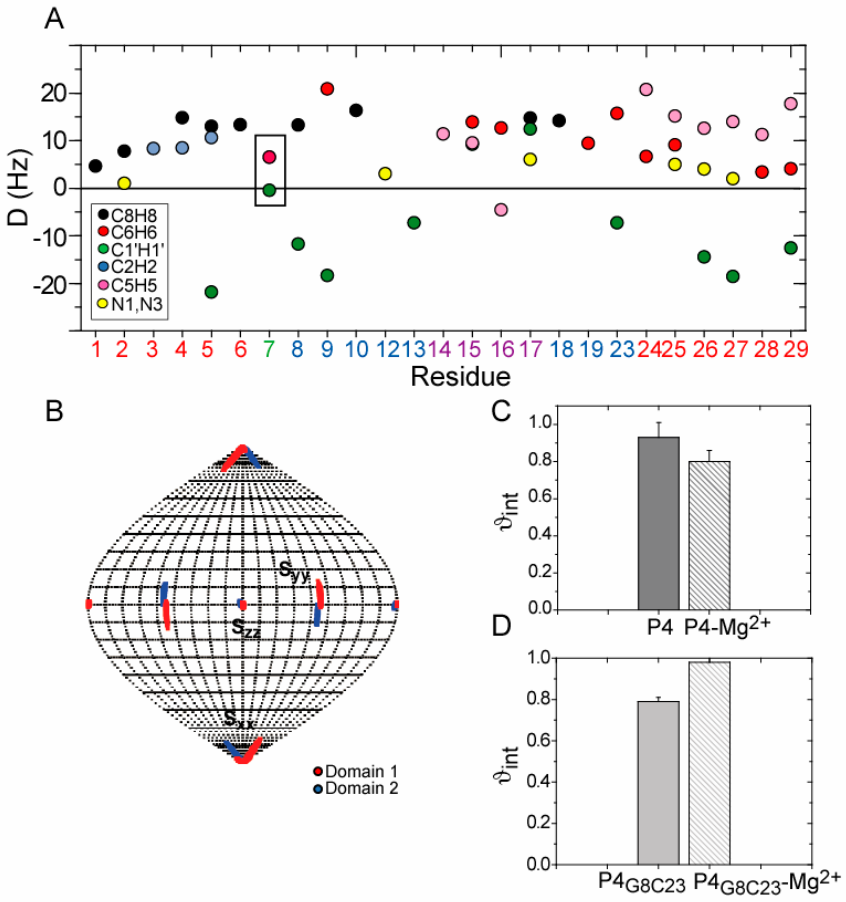

Figure 4-7. RDC order tensor analysis of $P4_{G8C23}$ in 20 mM Mg^{2+}. (A) RDCs as a function of residue for $P4_{G8C23}$. Shown are the values for C8H8 (black), C6H6 (red), C1'H1' (green), C5H5 (pink), C2H2 (blue), and N1H1/N3H3 (yellow). (B) Top 10 % of solutions for $P4_{G8C23}$ Mg^{2+} RDCs fit to P4 Mg^{2+} bound structure shown on a Sanson-Flamsteed map for domain 1 (red) and domain 2 (blue). (C) ϑ_{int} comparison for P4 free (dark grey) and Mg^{2+} (dark grey stripes). (D) ϑ_{int} comparison for $P4_{G8C23}$ free (light grey) and in 20 mM Mg^{2+} (light grey stripes).

V. Picosecond-nanosecond motions in $P4_{G8C23}$ in the absence and presence of Mg^{2+} by motionally decoupled spin relaxation

Our RDC results suggested that $P4_{G8C23}$ has altered dynamical properties at sub-millisecond timescales compared to P4 and that its dynamics are more greatly affected by Mg^{2+} binding. To further characterize the dynamical properties of $P4_{G8C23}$, we applied domain-elongation and measurements of relaxation data to examine picosecond-to-nanosecond dynamics in the presence and absence of Mg^{2+}.

Once again, excellent overlap was observed between spectra of elongated and non-elongated $P4_{G8C23}$, showing that the elongation did not significantly alter the properties of $P4_{G8C23}$ (data not shown). The shortage of well resolved imino nitrogen probes made it crucial to also measure carbon relaxation data (C8) using experiments developed in the group (Hansen and Al-Hashimi). Shown in Figure 4-8A are example single exponential decay curve fits for ^{15}N G1, ^{15}N G17, and ^{13}C8 G18, of both the longitudinal (R_1) and transverse (R_2) relaxation rates (Table 4.3).

Although based on only two values in each domain, the imino nitrogen R_2/R_1 ratios for E-$P4_{G8C23}$ show evidence for inter-helical motion on the nanosecond timescale. The amplitude of inter-helical motion in E-$P4_{G8C23}$ appears to be larger than in E-P4 as judged from the larger gap in the domain R_2/R_1 ratios (Fig. 4-8B). In E-P4, the domain 2 R_2/R_1 values are attenuated by ~17 % relative to domain 1 whereas in E-$P4_{G8C23}$, the domain 2 values are attenuated by ~37%. This is consistent with the RDC data which showed larger inter-helical motions in $P4_{G8C23}$ (ϑ_{int} = 0.79) compared to P4 (ϑ_{int} = 0.93). Unlike the RDC results, the domain motions are only marginally decreased in E-$P4_{G8C23}$ upon addition of up to 40 mM Mg^{2+} (the attenuation changed from ~37% to ~30%; Fig.

4-8B). A similar picture was painted by the nucleobase carbon C8 R_2/R_1 ratios (Fig. 4-8B), and extended model-free analysis of the ^{15}N relaxation data confirms the above qualitative interpretation of the R_2/R_1 ratios (Fig. 4-8C, Table 4.4).

Table 4.3 ^{15}N Relaxation data and Model-free results for E-AU-P4$_{G8C23}$ in the absence and presence of 40 mM Mg^{2+} recorded at 298 K, 600 MHz.

Free

	R_1 (Hz)	R_2 (Hz)	NOE
G1	0.749±0.003	24.26±0.23	0.699±0.015
G2	0.746±0.004	22.26±0.09	0.682±0.014
G12	0.976±0.008	17.99±0.78	0.569±0.011
G17	0.946±0.019	19.51±0.38	0.660±0.017

	Model	S^2_f	S^2_s	τ_f(ps)	τ_s(ns)	Γ_i
G1	4	0.837±0.004		19.845±2.378		0.000
G2	1	0.831±0.003		21.971±2.144		0.000
G12	5	0.790±0.016	0.825±0.022		1.460±0.074	0.000
G17	5	0.849±0.011	0.834±0.012		1.696±0.134	0.000

Mg^{2+}

	R_1 (Hz)	R_2 (Hz)	NOE
G1	0.770±0.014	24.43±0.35	0.673±0.021
G2	0.751±0.008	24.35±0.30	0.703±0.023
G12	0.985±0.015	20.15±0.85	0.630±0.021
G17	0.943±0.015	22.96±1.31	0.622±0.040

	Model	S^2_f	S^2_s	τ_f(ps)	τ_s(ns)	Γ_i
G1	2	0.876±0.010		33.734±5.666		0.196
G2	2	0.867±0.007		23.121±4.667		0.142
G12	5	0.852±0.024	0.818±0.017		1.669±0.142	0.000
G17	5	0.911±0.035	0.879±0.021		1.260±0.224	0.000

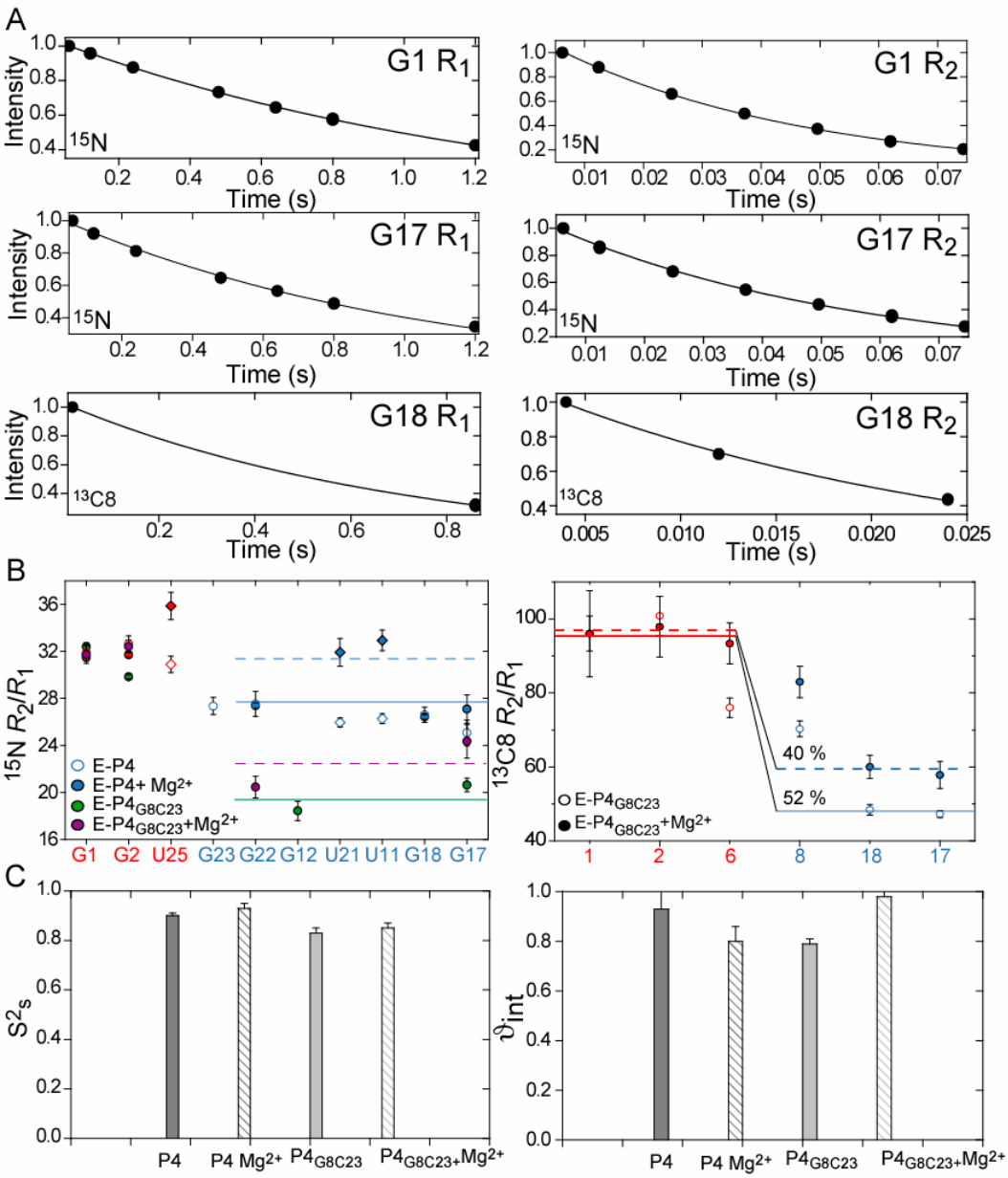

Figure 4-8. Dynamics determined by domain elongation and relaxation data for E-P4$_{G8C23}$ in the absence and presence of Mg^{2+}. (A) Example single exponential decay curve fits for ^{15}N R_1 and R_2 for G1 and G17 and ^{13}C R_1 and R_2 for G18 as a function of delay time (s). (B) R_2/R_1 values for ^{15}N (left) and $^{13}C8$ (right) for E-P4$_{G8C23}$ (closed symbols for free (green) and Mg^{2+} (purple)) compared to E-P4 (open symbols). Guanine residues are shown as circles, uridine as diamonds with domain 1 in red and domain 2 in blue. Lines represent average values for each domain for free (solid) and Mg^{2+} (dotted). (C) Dynamical parameters for E-P4$_{G8C23}$ derived from extended Model-free[14, 15] and order tensor analysis. Shown are amplitudes for slow (S^2_s) internal motions from relaxation and ϑ_{int} from order tensor analysis.

Table 4.4 ^{13}C relaxation data for E-AU-$P4_{G8C23}$ in the absence and presence of Mg^{2+} at 298 K and 600 MHz.

Free

Residue	Atom	R_1 (Hz)	R_2 (Hz)
1	C8	1.007 ± 0.022	96.66 ± 4.25
2	C8	0.956 ± 0.005	96.39 ± 4.85
6	C8	1.107 ± 0.026	84.21 ± 2.10
8	C8	1.153 ± 0.029	81.04 ± 1.38
17	C8	1.316 ± 0.005	62.20 ± 1.24
18	C8	1.366 ± 0.014	66.14 ± 1.79

40 mM Mg^{2+}

Residue	Atom	R_1 (Hz)	R_2 (Hz)
1	C8	1.044 ± 0.072	100.26 ± 9.99
2	C8	1.032 ± 0.032	101.04 ± 7.85
6	C8	1.070 ± 0.031	99.91 ± 5.22
8	C8	1.070 ± 0.031	88.82 ± 3.76
17	C8	1.254 ± 0.034	72.35 ± 5.93
18	C8	1.337 ± 0.023	80.26 ± 3.96

While RDCs measured in non-elongated $P4_{G8C23}$ suggest that Mg^{2+} arrests the collective motions, the spin relaxation data reveal only a small decrease in the inter-helical motional amplitudes. This contrasts with other RNAs such as SL1 from HIV-1 in which the addition of Mg^{2+} resulted in the arrest of domain motions both from the RDC and relaxation perspective[16]. One possibility is that Mg^{2+} binding alters the hinge point such that the two domains move by a similar amount in a coupled manner causing observation of $\vartheta_{int} \sim 1$ despite the presence of domain motions. We already have evidence that subtle variations in the location of the hinge can cause differences in the ϑ value observed for the two domains. In P4, the upper C8-G23 base-pair deviated from ideality. Location of the hinge closer to domain 2 led to the expected behavior in which domain 1 dominated alignment. In $P4_{G8C23}$, the non-ideal base-pair was shifted to the G6-C24 base-pair below the bulge and accordingly, domain 2 dominates alignment. It is possible

that Mg^{2+} binding created a situation in which $P4_{G8C23}$ exists in an equal mixture between the wild-type and mutant Mg^{2+} free states. Alternatively, Mg^{2+} binding may have changed the location of the hinge to be exactly at the bulge and therefore at the center of the two above cases.

The E-$P4_{G8C23}$ resonance intensities provide additional insights into the dynamics of $P4_{G8C23}$ and differences relative to P4. While in E-P4 the bulge appears highly flexible at picosecond-to-nanosecond timescales, this mobility appears to be greatly diminished in $P4_{G8C23}$, as indicated by a loss of motional narrowing and the smaller resonance intensity in E-$P4_{G8C23}$ (Fig. 4-9). Based on intensities alone, it could be concluded that the bulge and its flanking residues were rigid. However, a slow (μs-ms) exchange process could mask the faster (ns) local motions. Considering that the RDC data clearly show that the bulge is dynamic (three RDCs within the uridine bulge were near zero), we conclude that there is an exchange process in the bulge region in $P4_{G8C23}$ but not in P4. The addition of Mg^{2+} seems to reduce the effects of this exchange process thus exposing fast local motions at the bulge as seen by a five-fold increase in its resonance intensity. A similar effect is observed in SL1m in which Mg^{2+} binding quenches an exchange process that masked fast local motions in a guanine loop residue[16].

What is the exchange process underlying the bulge uridine dynamics? As mentioned previously, the observation of continuous NOE connectivities throughout the bulge region in $P4_{G8C23}$ supports a flipped-in position while NOEs from G6 H1' to the base in C8 supports a flipped-out position, as observed in P4. The flipped-in NOEs are not observed in P4. This strongly suggests that the exchange process involves the flipping in and out of the uridine bulge in the absence of Mg^{2+}.

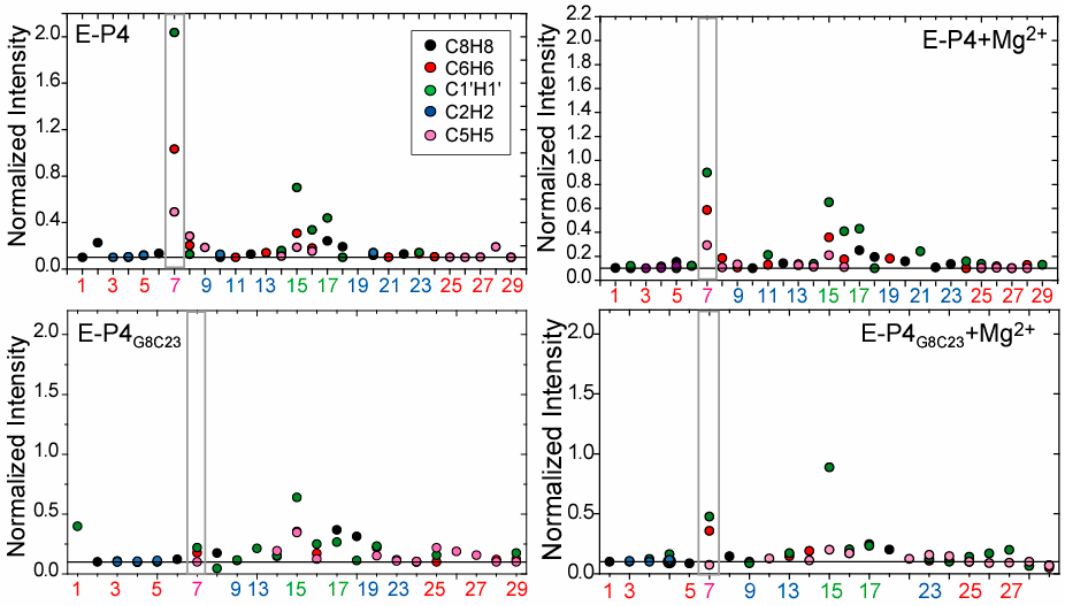

Figure 4-9. Local dynamics observed in E-P4$_{G8C23}$ compared to E-P4. Normalized resonance intensities for E-P4 (top) and E-P4$_{G8C23}$ (bottom) without and with Mg^{2+} (right) as a function of residue number for a variety of atom pairs: C8H8 (black), C6H6 (red), C1'H1' (green), C2H2 (blue), and C5H5 (pink). The bulged U7 is highlighted. The smallest peaks for each atom type were normalized to 0.1.

Why should this flipping process occur in P4$_{G8C23}$ but not in P4? Base stacking for purines is generally stronger than that for pyrimidines, so a uridine stacked between two guanines (as in P4$_{G8C23}$) would be more stable than between a purine and pyrimidine. This dynamic process at the inter-helical hinge may explain the larger amplitude inter-helical motions observed in E-P4$_{G8C23}$ compared to E-P4.

IV. The effect of P4$_{G8C23}$ on the activity of RNase P

Our study showed that the C-G to G-C base flip had large effects on the structural dynamics and metal binding properties of P4. To relate this information to RNase P function, A. Andrews (Fierke lab) introduced this mutation in the holoenzyme and performed *in vitro* activity assays. Results showed that the mutation had dramatic effects

on the activity of RNase P. The single turnover rate constant (k_{max}) for $P4_{G8C23}$ in the RNase P holoenzyme at saturating Mg^{2+} with a background of 2 mM $Co(NH_3)_6^{3+}$ (pre-formed ES complex) was down 60-fold compared to *wt* at high pH (Table 4.5). This decrease in rate constant placed it on par with the most dramatic effects on catalysis seen in the previous study by Kaye and co-workers such as moving the bulge in the 5' direction or changing it to a guanine which causes alternate base pairing (although direct comparisons could not be made due to different assay conditions: pH 6.0 and 300 mM Mg^{2+}, with a background of 10 mM $CaCl_2$[17]). The single turnover rate constant for the double G-C/G-C mutant at saturating Mg^{2+} is only down by 10-fold (the $K_{1/2}$ is not affected by the single mutation, and only exhibits a 3-fold reduction in the double mutant). The effect of a seemingly minor mutant, a single base pair flip of a C-G to G-C, has a dramatic effect on the activity of RNase P. The double mutant, where the tandem purines are conserved but located on the opposite strand, restores some of the activity of the enzyme, but not completely. This suggests that the functional groups on the

	Low pH (5.5)			High pH (7.7)		
	$K_{1/2}^{Mg}$ (mM)	a_H	k_{max} (s^{-1})	$K_{1/2}^{Mg}$ (mM)	a_H	k_{max} (s^{-1})
single C-G (G8C23)	14.7±4.6	1.9±0.3	0.006±0.001	6.7±1.0	1.6±0.3	0.01±0.001
double C-G G8C23,G9C22)	15.0±2.0	1.7±0.07	0.007±0.001	20.4±1.4	1.6±0.03	0.05±0.002
wild-type	13.7±1.3	1.8±0.06	0.07±0.01	6.8±1.8	1.1±0.2	0.6±0.1

Table 4.5 Magnesium ion dependence of the rate constant for single turnover cleavage by wild-type *B. subtilis* RNase P, single mutant (G8C23) and double mutant (G8C23,G9C22) of pre-tRNA. The k_{max} is the maximum rate constant at saturating Mg^{2+}, $K_{1/2}$ is the concentration of Mg^{2+} at half maximal activity and a_H is the cooperativity of the magnesium dependence. The conditions for these reactions were 2 μM holoenzyme, 50 mM Mes/tris, 133-200 mM KCl, 0-20 mM $MgCl_2$ incubated at 37°C. Used with permission from A. Andrews (unpublished results).

nucleotides and their exact location have an essential role in catalysis and/or substrate binding. One possible role consistent with the NMR data is that this region of P RNA binds a Mg^{2+} ion important for stabilizing the active site structure or the transition state.

V. Discussion

In this study, we have identified metal binding, structural, and dynamical properties of $P4_{G8C23}$ that were different from those in the P4 sequence. These alterations also correlate with the effects of this mutation on the activity of the holoenzyme RNase P. Chemical shift perturbations were present at two additional sites in $P4_{G8C23}$, C9 and U7, which were not affected in P4. The Mg^{2+} binding affinity was uniformly higher (most have between 0.05 and 1 mM apparent K_ds) in $P4_{G8C23}$ whereas in P4 there was a range of 0.7 to 7.3 mM, suggesting several sites of similar affinity in $P4_{G8C23}$. The change in location and affinity for Mg^{2+} in $P4_{G8C23}$ could have affected the location of metals essential for catalysis and/or substrate binding in RNase P.

Characterization of $P4_{G8C23}$ structure and dynamics in the absence of divalent ions provides new insights into how sequence codes for structure and dynamics in P4 and in RNA in general. First, the amplitude of motion was slightly larger in $P4_{G8C23}$ than in P4 as measured by both RDCs and spin relaxation with domain elongation. Second, the hydrogen bond alignment of base-pairs flanking the bulge is altered, and the pivot point of the motion appears to have shifted from being near domain 2 (P4) to domain 1 ($P4_{G8C23}$). Third, the U7 bulge shows slower μs-ms motions that are consistent with flipping motions in $P4_{G8C23}$ that are absent in the P4 sequence. This base flipping in and out motion would explain both the slow dynamics of the bulge, the larger amplitude

inter-helical motions and perhaps the slightly increased inter-helical twist angle in the average structure (Fig. 4-10).

In RNase P, the G-C mutation may cause slower folding of P RNA as indicated by the need for a longer pre-incubation time to form active RNase P: 50+ minutes in the mutant compared to 30 minutes in wild-type (A. Andrews, unpublished data). This slow folding may be caused by the change in the basic conformational properties of $P4_{G8C23}$ in the absence of divalent ions. Importantly, similar bulge looping motions have been observed in other RNAs, including U6 RNA where at low pH a key cytosine residue is protonated and the bulge is flipped out; at high pH (where the base pair forms), the bulge is flipped in[18]. Both U6 and $P4_{G8C23}$ have purines flanking bulged uridine residues which, due to their ability to form favorable stacking interactions, play a key role in determining the location and motional properties of the bulge residue.

The more relevant conditions for probing structure and dynamics of $P4_{G8C23}$ are in Mg^{2+}. Our results suggest that Mg^{2+} only slightly reduces the amplitude of inter-helical motions in $P4_{G8C23}$. The similar degree of order observed for the two domains by RDCs likely reflected changes in the pivot point which apparently allow the two domains to move by a similar amount. This result underscores the importance of elongating RNA in order to decouple internal from overall motions. Alternatively, slower motions may be quenched by Mg^{2+} binding. The remaining faster motions that were observed by spin relaxation may evade detection by RDCs, for example, because they involve rotations around the axially symmetric S_{zz} which in non-elongated $P4_{G8C23}$ is expected to have an orientation that is quite distinct from the D_{zz} orientation governing the relaxation data.

In contrast, the motional narrowing data suggests that Mg^{2+} stabilizes the bulge in an extra-helical conformation, thus arresting the exchange process. This arrest explains the observed small reduction in the amplitude of inter-helical motions in the presence of Mg^{2+}.

It is beneficial to compare the inter-helical orientation of P4 with other single bulge containing RNAs. An inter-helical bend angle of 10° ± 5° was found using transient electric birefringence for double helices containing a single uridine bulge[19]. Other NMR studies suggest that the identity of the base pairs flanking the bulge

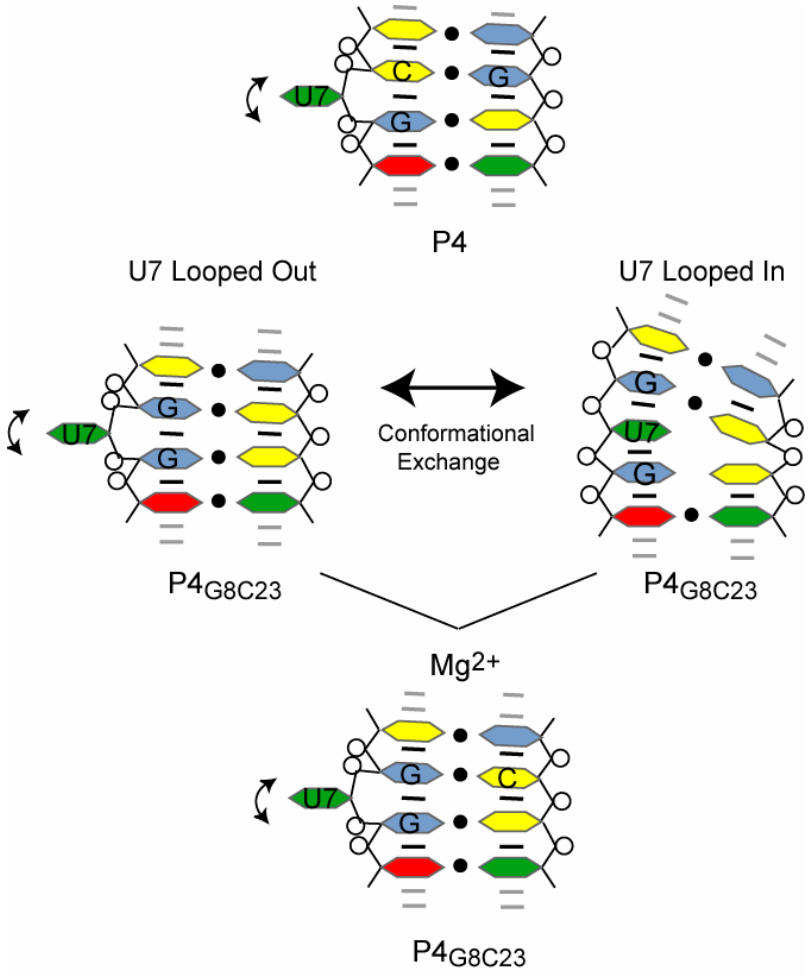

Figure 4-10. Schematic representation of local motions in P4 and $P4_{G8C23}$. Top: local bulge movement in P4, middle: model of base flipping motion for bulge in $P4_{G8C23}$, and bottom: Mg^{2+} stabilizes the looped out bulge position.

determine the inter-helical angle. For both P4 and $P4_{G8C23}$ which have C-G/G-C base pairs flanking the bulge, the inter-helical angle is 10°. For IRE (iron responsive element) the inter-helical angle is 15° with a G-C on one side of the bulge and an A-U on the other (Fig. 4-11) [20]. For HBV (hepatitis B viral genome) which has a C-G on one side and a U-G on the other, the inter-helical angle is 20° [21]. And, lastly, for SL-IV (*Tetrahymena thermophila* stemloop IV), the bulge residue is flanked by a C-G on one side and two A-U/U-A base pairs on the other. The two A-U/U-A base pairs form an unstable stretch between two bulge regions which has an inter-helical angle of 43° [22]. Based on this trend, it seems as though weaker base pairs flanking a single bulge enable more flexibility and give a larger average inter-helical angle. These examples also show a trend in dynamic properties of single residue bulges. The bulge residues have increased local flexibility which was also seen in P4 and $P4_{G8C23}$ (Fig. 4-11, purple circles). These examples were reviewed recently in Biopolymers[23].

The change in the structural dynamics of $P4_{G8C23}$ was accompanied by a change in its Mg^{2+} binding properties. This most likely reflected the disruption of the tandem guanine residues opposite the bulge. Two sites, U7 and C9 both showed significant chemical shift changes in Mg^{2+} in $P4_{G8C23}$ and not in P4, reflecting a change in the binding location away from the tandem guanine residues. If P4 has a role in substrate positioning, as has been shown recently[24], a change in the metal binding site could prevent an essential metal from binding properly and thereby prevent the substrate from binding the reactive conformation. The effects of $P4_{G8C23}$ on the activity of the holoenzyme shows both a change in the catalytic rate constant and the number of metals involved in catalysis in the holoenzyme. The 60-fold lower rate constant for enzymatic

activity of the single mutant in RNase P along with an increased Hill coefficient to 1.6 ±0.3 from 1.1 ±0.1 in wild-type are consistent with a role of the tandem guanines in P4 in enhancing the binding affinity of the catalytic metal ion. The disruption of the tandem guanine residues and decreased affinity of a catalytic metal could have increased the dependence on co-catalytic metals which explains the higher Hill coefficient. Further analysis in the context of the RNA component is required to determine to what extent the metal binding properties of P4 and its dynamics contribute to catalytic activity.

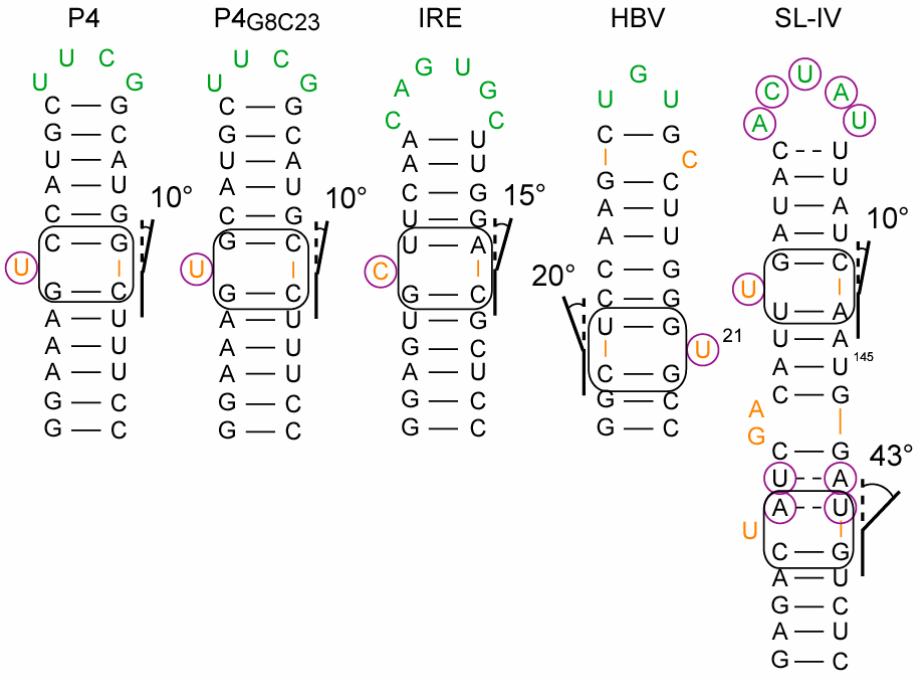

Figure 4-11. Secondary structures of previously studied single bulge RNAs. Locally flexible residues are shown as purple circles, and inter-helical bend angles are indicated for P4, $P4_{G8C23}$, IRE (iron responsive element), HBV (hepatitis B viral genome), and SL-IV (*Tetrahymena thermophila* stem loop IV). Residues flanking the bulges are in boxes.

Materials and Methods

Preparation and purification of $^{13}C/^{15}N$ labeled RNA and NMR spectroscopy

$P4_{G8C23}$, E-AU-$P4_{G8C23}$, and E-GC-$P4_{G8C23}$ RNA samples (Fig. 4-1) for NMR studies were prepared and purified as discussed previously by *in vitro* transcription reactions using T7 RNA polymerase[25], uniformly ^{13}C/ ^{15}N labeled (Spectra Stable Isotopes, Inc. and ISOTEC, Inc.) or unlabeled (Sigma) nucleotide triphosphates, and synthetic DNA templates (Integrated DNA Technologies, Inc.) containing the T7 promoter and sequence of interest. For details see Appendix. An additional $P4_{G8C23}$ NMR sample for measurement of RDCs was prepared containing 15 mg/mL of Pf1 phage[7] (Asla Biotech). The final RNA concentration in the NMR samples ranged between 0.2 and 1 mM.

Resonance assignment, RDCs, and relaxation experiments were carried out as in Chapter 2. The $^{1}H–^{13}C$ splittings were measured in the divalent ion-free $P4_{G8C23}$ sample as the difference in the upfield and downfield components of the $^{1}H–^{13}C$ doublet along the ^{1}H and ^{13}C dimension[26-28] while RDCs for $P4_{G8C23}$ in the presence of 20 mM Mg^{2+} were obtained using splittings measured in the ^{13}C dimension. In all cases, RDCs from base pairs G1–C29, G2–C28, and G6–C24, which based on the $^{2h}J_{NN}$-COSY experiment have partial or no hydrogen bonding, were excluded from analysis.

All of the ^{15}N relaxation data were measured in free and Mg^{2+} samples for E-$P4_{G8C23}$ closely following the procedure described previously[29]. Briefly, imino ^{15}N longitudinal (R_1) and transverse ($R_{2(CPMG)}$) relaxation rates and $^{1}H–^{15}N$ NOEs were measured as in Chapter 2[30].

Longitudinal (R_1) and rotating-frame ($R_{1\rho}$) relaxation rates were measured for nucleobase carbon C8 using TROSY detected (TD) experiments (Hansen and Al-Hashimi, *submitted*) which was adapted from the TS-$R_{1\rho}$ experiment described by Palmer and co-workers for measurement of nitrogen relaxation dispersion in proteins[31]. In the R_1 experiment, cross relaxation to neighboring carbons is suppressed, as originally described by Kay and co-workers, by gradient dephasing carbon magnetization at the beginning of the pulse sequence followed by selective excitation of the carbon nucleus of interest using selective refocusing ^{13}C 180° pulses during the INEPT period[32]. High power off-resonance spin locks were used in the $R_{1\rho}$ experiment to minimize contributions from chemical exchange while also being optimized to suppress Hartman-Hahn type transfers to scalar coupled carbon spins (*vide infra*). Accurate alignment of the $\pm C_z$ magnetization to and from the effective field tilt angle θ at the beginning and end of relaxation period was achieved using an adiabatic half passage[33]. Spin lock powers were carefully calibrated by Hansen and Al-Hashimi as described by Palmer *et. al.*[34]. For E-AU-P4$_{G8C23}$, the spin lock offset was +2750 Hz for C8 and the carrier set to 136.5 ppm. The $R_{1\rho}$ rates were corrected for off-resonance effects according to $R_{1\rho} = R_1 \cos^2\theta + R_2 \sin^2\theta$, in which $\theta = \arctan(\nu_{SL}/\Omega)$ is the effective tilt angle of the spinlock field, ν_{SL} is the spinlock field strength in Hz, and Ω is the resonance offset from the spinlock carrier frequency in Hz (Hansen and Al-Hashimi, *submitted*). Measurement delays were chosen following a strategy described previously where the first point is at zero (or very close) and the last four points are at 1.3 T[35]. Delays for E-AU-P4$_{G8C23}$ for ^{13}C8 were: 20, and 860 (x4) ns for R_1 and 4, 12 (x2), and 24 (x2) ns for $R_{1\rho}$. All relaxation series were recorded in an interleaved manner with alternating short and long relaxation (T) delays. Relaxation rates

and errors were determined by fitting intensities to a mono-exponential decay using Origin 7.0 (OriginLab Corporation).

Mg^{2+} induced perturbations in chemical shifts and binding affinities were measured as in Chapter 3. Inter-helical orientation and dynamics were determined for $P4_{G8C23}$ with and without Mg^{2+} as described in Chapter 2.

Model-free analysis of relaxation data

Model-free analysis of relaxation data was performed as described in Chapter 2. The final model selections comprised models 2 and 5 for residues in domains 1 and 2, respectively, in E-$P4_{G8C23}$. With the exception of residue G1 in domain 1 (model 4), the model selections for E-$P4_{G8C23}$-Mg were also models 2 and 5 for residues in domains 1 and 2, respectively.

References

1. Wüthrich, K., *NMR of Proteins and Nucleic Acids*. John Wiley and Sons: New York, 1986.

2. Sklenar, V.; Peterson, R. D.; Rejante, M. R.; Feigon, J., Two- and three-dimensional HCN experiments for correlating base and sugar resonances in $^{15}N,^{13}C$-labeled RNA oligonucleotides. *J. Biomol. NMR* **1993,** *3*, 721-7.

3. Dingley, A. J.; Grzesiek, S., Direct observation of hydrogen bonds in nucleic acid base pairs by internucleotide $^{2}J_{NN}$ couplings. *J. Am. Chem. Soc.* **1998,** *120*, (33), 8293-8297.

4. Pervushin, K.; Ono, A.; Fernandez, C.; Szyperski, T.; Kainosho, M.; Wüthrich, K., NMR scalar couplings across Watson-Crick base pair hydrogen bonds in DNA observed by transverse relaxation-optimized spectroscopy. *Proc. Natl. Acad. Sci. USA* **1998,** *95*, (24), 14147-51.

5. Tjandra, N.; Bax, A., Direct measurement of distances and angles in biomolecules by NMR in a dilute liquid crystalline medium. *Science* **1997,** *278*, (5340), 1111-1114.

6. Clore, G. M.; Starich, M. R.; Gronenborn, A. M., Measurement of residual dipolar couplings of macromolecules aligned in the nematic phase of a colloidal suspension of rod- shaped viruses. *J. Am. Chem. Soc.* **1998,** *120*, (40), 10571-10572.

7. Hansen, M. R.; Mueller, L.; Pardi, A., Tunable alignment of macromolecules by filamentous phage yields dipolar coupling interactions. *Nat. Struct. Biol.* **1998,** *5*, (12), 1065-1074.

8. Prestegard, J. H.; Al-Hashimi, H. M.; Tolman, J. R., NMR structures of biomolecules using field oriented media and residual dipolar couplings. *Quart. Rev. Biophys.* **2000,** *33*, (4), 371-424.

9. Losonczi, J. A.; Andrec, M.; Fischer, M. W.; Prestegard, J. H., Order matrix analysis of residual dipolar couplings using singular value decomposition. *J. Magn. Reson.* **1999,** *138*, 334-342.

10. Tolman, J. R.; Al-Hashimi, H. M.; Kay, L. E.; Prestegard, J. H., Structural and dynamic analysis of residual dipolar coupling data for proteins. *J. Am. Chem. Soc.* **2001,** *123*, (7), 1416-1424.

11. Al-Hashimi, H. M.; Gosser, Y.; Gorin, A.; Hu, W.; Majumdar, A.; Patel, D. J., Concerted motions in HIV-1 TAR RNA may allow access to bound state conformations: RNA dynamics from NMR residual dipolar couplings. *J. Mol. Biol.* **2002,** *315*, (2), 95-102.

12. Pitt, S. W.; Majumdar, A.; Serganov, A.; Patel, D. J.; Al-Hashimi, H. M., Argininamide binding arrests global motions in HIV-1 TAR RNA: Comparison with Mg^{2+} induced conformational stabilization. *J. Mol. Biol.* **2004,** *338*, 7-16.

13. Tolman, J. R.; Flanagan, J. M.; Kennedy, M. A.; Prestegard, J. H., NMR evidence for slow collective motions in cyanometmyoglobin. *Nat. Struct. Biol.* **1997,** *4*, (4), 292-297.

14. Lipari, G.; Szabo, A., Model-free approach to the interpretation of nuclear magnetic resonance relaxation in macromolecules. 1. Theory and range of validity. *J. Am. Chem. Soc.* **1982,** *104*, 4546-4559.

15. Clore, G. M.; Szabo, A.; Bax, A.; Kay, L. E.; Driscoll, P. C.; Gronenborn, A. M., Deviations from the simple two-parameter model-free approach to the interpretation of nitrogen-15 nuclear magnetic relaxation of proteins. *J. Am. Chem. Soc.* **1990,** *112*, 4989 - 4991.

16. Sun, X.; Zhang, Q.; Al-Hashimi, H. M., Resolving fast and slow motions in the internal loop containing stem-loop 1 of HIV-1 that are modulated by Mg2+ binding: role in the kissing-duplex structural transition. *Nucleic Acids Res.* **2007**.

17. Kaye, N. M.; Zahler, N. H.; Christian, E. L.; Harris, M. E., Conservation of helical structure contributes to functional metal ion interactions in the catalytic domain of ribonuclease P RNA. *J. Mol. Biol.* **2002,** *324*, (3), 429-42.

18. Reiter, N. J.; Blad, H.; Abildgaard, F.; Butcher, S. E., Dynamics in the U6 RNA intramolecular stem-loop: a base flipping conformational change. *Biochemistry* **2004,** *43*, (43), 13739-47.

19. Zacharias, M.; Hagerman, P. J., Bulge-induced bends in RNA: quantification by transient electric birefringence. *J. Mol. Biol.* **1995,** *247*, (3), 486-500.

20. McCallum, S. A.; Pardi, A., Refined solution structure of the iron-responsive element RNA using residual dipolar couplings. *J. Mol. Biol.* **2003,** *326*, 1037-1050.

21. Flodell, S.; Petersen, M.; Girard, F.; Zdunek, J.; Kidd-Ljunggren, K.; Schleucher, J.; Wijmenga, S., Solution structure of the apical stem-loop of the human hepatitis B virus encapsidation signal. *Nucleic Acids Res.* **2006,** *34*, (16), 4449-57.

22. Chen, Y.; Fender, J.; Legassie, J. D.; Jarstfer, M. B.; Bryan, T. M.; Varani, G., Structure of stem-loop IV of Tetrahymena telomerase RNA. *EMBO J.* **2006,** *25*, (13), 3156-3166.

23. Getz, M.; Sun, X.; Casiano-Negroni, A.; Zhang, Q.; Al-Hashimi, H. M., NMR studies of RNA dynamics and structural plasticity using NMR residual dipolar couplings. *Biopolymers* **2007,** *86*, 384-402.

24. Christian, E. L.; Smith, K. M. J.; Perera, N.; Harris, M. E., The P4 metal binding site in RNase P RNA affects active site metal affinity through substrate positioning. *RNA* **2006,** *12*, 1463-7.

25. Milligan, J. F.; Uhlenbeck, O. C., Synthesis of small RNAs using T7 RNA polymerase. *Methods Enzymol.* **1989,** *180*, 51-62.

26. Meissner, A.; Duus, J. O.; Sorensen, O. W., Spin-state-selective excitation. Application for E.COSY-type measurement of J_{HH} coupling constants. *J. Magn. Reson.* **1997,** *128*, 92-97.

27. Meissner, A.; Sorensen, O. W., The role of coherence transfer efficiency in design of TROSY-type multidimensional NMR experiments. *J. Magn. Reson.* **1999,** *139*, 439-442.

28. Pitt, S. W.; Zhang, Q.; Patel, D. J.; Al-Hashimi, H. M., Evidence that electrostatic interactions dictate the ligand-induced arrest of RNA global flexibility. *Angew. Chem. Int. Ed. Engl* **2005,** *44*, 3412-5.

29. Zhang, Q.; Sun, X.; Watt, E. D.; Al-Hashimi, H. M., Resolving the motional modes that code for RNA adaptation. *Science* **2006,** *311*, (5761), 653-6.

30. Palmer, A. G., NMR characterization of the dynamics of biomacromolecules. *Chem. Rev.* **2004,** *104*, 3623-3640.

31. Igumenova, T. I.; Frederick, K. K.; Wand, A. J., Characterization of the fast dynamics of protein amino acid side chains using NMR relaxation in solution. *Chem. Rev.* **2006,** *106*, (5), 1672-99.

32. Yamazaki, T.; Muhandiram, R.; Kay, L. E., NMR Experiments for the Measurement of Carbon Relaxation Properties in Highly Enriched, Uniformly 13C, 15N-Labeled Proteins: Application to 13Cα Carbons. *J. Am. Chem. Soc.* **1994,** *116*, 8266-8278.

33. Mulder, F. A.; De Graaf, R. A.; Kaptein, R.; Boelens, R., An off-resonance rotating frame relaxation experiment for the investigation of macromolecular dynamics using adiabatic rotations. *J. Mag. Reson.* **1998,** *131*, 351-357.

34. Palmer, A. G., 3rd; Kroenke, C. D.; Loria, J. P., Nuclear magnetic resonance methods for quantifying microsecond-to-millisecond motions in biological macromolecules. *Methods Enzymol.* **2001,** *339*, 204-38.

35. Jones, J. A.; Hodgkinson, P.; Barker, A. L.; Hore, P. J., Optimal sampling strategies for the measurement of spin-spin relaxation times. *J. Mag. Reson. Ser. B* **1996,** *113*, 25-34.

Chapter 5

Conclusion and Future Directions

I. Conclusion

We have examined how the highly conserved P4 sequence uniquely codes for structure, dynamics, and metal binding through a combination of RDCs, motionally decoupled relaxation, and chemical shift mapping experiments both for a P4 construct from *B. subtilis* and a functionally disruptive mutant $P4_{G8C23}$. We have shown how RDCs and motionally decoupled relaxation can be combined to give a comprehensive description of the structure and dynamics of a small RNA that could not be obtained with either method alone. For example, in the case of $P4_{G8C23}$ in Mg^{2+}, inter-helical motions would have gone undetected if not for the relaxation analysis on the elongated RNA (since order tensor analysis showed nearly identical ϑ_{int} values for each domain). In a second example, local motions at the bulge U7 in the mutant would have gone undetected (based on similar intensities to residues within the helix) if not for combination with RDC analysis which showed attenuated RDCs at multiple sites within the bulge. Both of these examples show that relaxation of elongated domains and order tensor analysis are highly complementary techniques which can give a wealth of both structural and

dynamical informational about RNA.

In addition to dynamics, the P4 sequence also codes for a unique Mg^{2+} binding scaffold. Previous NMR studies of P4 would suggest an outer sphere binding role (hence a structural/folding role) for Mg^{2+} in P4 due to its potential for binding $Co(NH_3)_6^{3+}$ [1]. Our results show that Mg^{2+} binding does not significantly alter the structure and/or dynamics of P4 and thus does not seem to play the role of changing the isolated P4 conformation (and the RDC-solved structure very closely matches that of the X-ray structure of RNase P in *B. stearothermophilus*). There are two remaining possible roles for the Mg^{2+} ions bound in the P4 helix. The first is inner sphere binding for which we have evidence for in the isolated P4 construct through substitution of Mg^{2+} with the combination of $Co(NH_3)_6^{3+}/Zn^{2+}$ and Zn^{2+} alone. The P4 helix contains the tandem guanine motif which has been shown in other RNAs to contain sites for inner sphere binding[2-4]. Further studies are necessary to determine if these sites remain present in the entire RNA component of RNase P and if they are accessible to the solvent in the holoenzyme.

Another possible role of the associated Mg^{2+} ions in P4 is substrate binding, since they are near a site of local flexibility (U7 and C8) that is known to interact with the pre-tRNA substrate. It is possible that the P4-associated metals form nonspecific intermolecular backbone bridging interactions with the tRNA substrate. Such Mg^{2+} intermolecular bridges have been observed between 16S and 30S ribosomal subunits[5] and between the thiamine pyrophosphate riboswitch and its cognate ligand TPP[6]. These interactions could aid in positioning the pre-tRNA substrate relative to the active site[7].

We have also shown that the slightly perturbed C8-G23 base pair above the bulge is an important determinant of the structural, dynamical and metal binding properties of

P4. This, along with the tandem guanine metal binding motif, led us to test the importance of this base-pair by studying the effects on structural dynamics and metal binding in $P4_{G8C23}$ in which the C8-G23 base-pair is flipped for a G8-C23. Characterization of the properties of $P4_{G8C23}$ in comparison to those of P4 showed critical differences in both Mg^{2+} binding affinity and location and dynamics of Mg^{2+} bound $P4_{G8C23}$. The mutation also causes significant effects on the activity of the enzyme, as shown by A. Andrews (Fierke lab). Decreased catalytic activity and an increased Hill coefficient in the presence of cobalt (III) hexamine suggests that the binding affinity for the inner sphere metal is lowered in $P4_{G8C23}$ and therefore catalysis is enhanced by other co-catalytic metals. This suggests a role for P4 in binding an inner sphere metal ion which would be involved in lowering the pK_a of the catalytic metal. If the role of P4 in RNase P is to position the substrate pre-tRNA, our results which show a change in the pivot point of motion in $P4_{G8C23}$ suggest that this alteration could prohibit RNase P from making the correct conformational change required to bind the substrate, release the product tRNA, or bind a metal ion required for substrate binding. Further analysis in the context of the RNA component is required to determine which of these alterations will have the greatest effect on catalytic activity.

II. Future Directions

Ligation of P4 into RNA component

An important future study is to compare the structure, dynamics, and metal properties of P4 in the context of the entire RNase P. A proposed method for this analysis is to incorporate a segment of $^{13}C/^{15}N$ isotopically-labeled P4 into an unlabeled RNase P

RNA, similar to the approach used to investigate the structure of HCV IRES RNA[8]. First, a 10 nucleotide oligomer primer of one strand of P4 can be prepared by primer directed transcription in the presence of labeled nucleotides and purified by denaturing PAGE and/or HPLC to remove the 3' end heterogeneity. This RNA oligomer can then be ligated to a circularly permuted P RNA[9, 10]. This method can be scaled up in order to yield the necessary amount of RNA for NMR analysis. The same method can be used to label the other half of P4 in a separate sample and join it to a P RNA without the other sequence. The chemical shifts of the P4 sequence should be fairly similar to those in RNase P and easy to identify since we have shown that the fragment of P4 had a similar structure as that in the crystal structure (Chapter 2). If analysis of the full RNA component of RNase P is too difficult, smaller functional forms of the enzyme can be studied such as the MRP *E. cunicui* (165 nt) which has all the residues in the conserved region of P4[11].

Paramagnetic metal localization and structure from alignment (RDCs)

In this study we have used Mn^{2+} dependent line broadening to detect inner sphere binding sites in P4 (Chapter 3). We have found intermediate Mn^{2+} concentrations where peaks are affected but not broadened beyond detection which are therefore useful in other analyses. In order to determine the position of the bound metal ion, ^{1}H Γ_2 relaxation can be measured for a variety of spins and this information potentially used in generating a statistical distribution for the diffusive metals which do not obey stoichiometric binding and are therefore difficult to characterize. Another application for paramagnetic metals which has been used in proteins is to exploit their inherently large anisotropic magnetic

susceptibility to measure field induced RDCs[12]. An advantage to paramagnetic alignment is that there is no need for an alignment medium which could affect the structure and/or dynamics of the molecule of interest.

References

1. Schmitz, M.; Tinoco, I. J., Solution structure and metal-ion binding of the P4 element from bacterial RNase P RNA. *RNA* **2000,** *6*, 1212-1225.

2. Cate, J. H.; Gooding, A. R.; Podell, E.; Zhou, K.; Golden, B. L.; Kundrot, C. E.; Cech, T. R.; Doudna, J. A., Crystal structure of a group I ribozyme domain: principles of RNA packing. *Science* **1996,** *273*, (5282), 1678-85.

3. Nowakowski, J.; Shim, P. J.; Stout, C. D.; Joyce, G. F., Alternative conformations of a nucleic acid four-way junction. *J. Mol. Biol.* **2000,** *300*, (1), 93-102.

4. Wild, K.; Weichenrieder, O.; Leonard, G. A.; Cusack, S., The 2 A structure of helix 6 of the human signal recognition particle RNA. *Structure* **1999,** *7*, (11), 1345-52.

5. Ghosh, S.; Joseph, S., Nonbridging phosphate oxygens in 16S rRNA important for 30S subunit assembly and association with the 50S ribosomal subunit. *RNA* **2005,** *11*, 657-667.

6. Serganov, A.; Polonskaia, A.; Phan, A. T.; Breaker, R. R.; Patel, D. J., Structural basis for gene regulation by a thiamine pyrophosphate-sensing riboswitch. *Nature* **2006,** *441*, 1167-1171.

7. Christian, E. L.; Smith, K. M. J.; Perera, N.; Harris, M. E., The P4 metal binding site in RNase P RNA affects active site metal affinity through substrate positioning. *RNA* **2006,** *12*, 1463-7.

8. Kim, I.; Lukavsky, P. J.; Puglisi, J. D., NMR study of 100 kDa HCV IRES RNA using segmental isotope labeling. *J. Am. Chem. Soc.* **2002,** *124*, (32), 9338-9.

9. Moore, M. J.; Query, C. C., Joining of RNAs by splinted ligation. *Methods Enzymol.* **2000,** *317*, 109-23.

10. Crary, S. M.; Kurz, J. C.; Fierke, C. A., Specific phosphorothioate substitutions probe the active site of *Bacillus subtilis* ribonuclease P. *RNA* **2002,** *8*, (7), 933-47.

11. Banci, L.; Bertini, I.; Huber, J. G.; Luchinat, C.; Rosato, A., Partial Orientation of Oxidized and Reduced Cytochrome b5 at High Magnetic Fields: Magnetic Susceptibility Anisotropy Contributions and Consequences for Protein Solution Structure Determination. *J. Am. Chem. Soc.* **1998,** *120*, 12903-12909.

12. Bertini, I.; Luchinat, C.; Parigi, G.; Pierattelli, R., NMR spectroscopy of paramagnetic metalloproteins. *Chembiochem* **2005,** *6*, (9), 1536-49.

Appendix

RNA sample preparation

P4, $P4_{G8C23}$, $P4_{Abulge}$, E-AU-P4, E-GC-P4, E-AU-$P4_{G8C23}$, and E-GC-$P4_{G8C23}$ RNA samples (Figs. 2-1A, 2-6A, 4-2A) for NMR studies were prepared by *in vitro* transcription reactions using T7 RNA polymerase [1], uniformly $^{13}C/\ ^{15}N$ labeled (Spectra Stable Isotopes, Inc. and ISOTEC, Inc.) or unlabeled (Sigma) nucleotide triphosphates, and synthetic DNA templates (Integrated DNA Technologies, Inc.) containing the T7 promoter and sequence of interest. Multiple small scale (50 μL) reactions were performed first with varying conditions (Table A1).

						Nucleotides (100mM)							
Rxn	H_2O	0.5M Mg^{2+}	0.5M Tris	1M DTT	0.25M Sperm.	A	U	C	G	PEG	Poly	DNA	H_2O
1	11.3	2	10	1.5	0.4	3	3	3	3	4	3	0.8	5
2	13.3	2	8	1.5	0.4	3	3	3	3	4	3	0.8	5
3	15.3	2	6	1.5	0.4	3	3	3	3	4	3	0.8	5
4	19.3	2	2	1.5	0.4	3	3	3	3	4	3	0.8	5
5	9.3	4	10	1.5	0.4	3	3	3	3	4	3	0.8	5
6	11.3	4	8	1.5	0.4	3	3	3	3	4	3	0.8	5
7	13.3	4	6	1.5	0.4	3	3	3	3	4	3	0.8	5
8	17.3	4	2	1.5	0.4	3	3	3	3	4	3	0.8	5

Table A1. Example test transcriptions, total volume 50 μL, volumes listed are in μL. DTT represents dithiolthreitol, Sperm. is spermidine, PEG polyethylene glycol, Poly is polymerase, and DNA deoxyribonucleic acid.

Added volumes were doubled or halved in order to see noticeable effects on yield. Shown is varying $MgCl_2$ and Tris, but nucleotide, polymerase, and DNA amounts were also optimized. Transcription yields were visualized via denaturing (8M urea/TBE) 15 %

(w/v) polyacrylamide gels stained in ethidium bromide and photographed on a UV transilluminator (Figure A1).

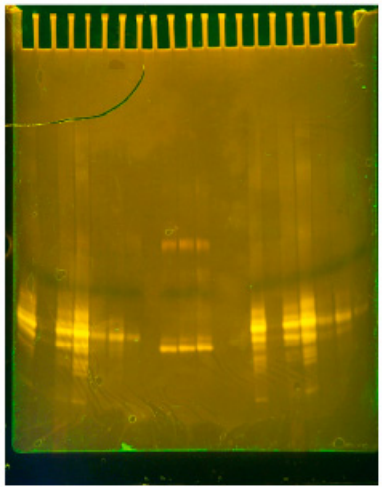

Figure A1. 15 % (w/v) polyacrylamide gel stained with ethidium bromide showing transcription yields for P4. The intensity of the band is proportional to the product yield. Approximately 2 μL of sample and 4 μL of loading buffer (Urea, glycerol, xylene cyanol, and bromophenol blue) were loaded into each lane.

Sample reactions are incubated at 37°C for two hours, then loaded onto the gel and run at 16W for 1-2 hours.

Once the optimum sample conditions were obtained, the transcription reaction was scaled up to 5-10 mL and incubated at 37°C overnight. The product was sterile filtered and concentrated using an Amicon device to reach a volume of 1 mL. The sample was purified by a large 15 % (w/v) polyacrylamide gel under denaturing conditions (8 M urea/ TBE). RNA was recovered from the gel by passive elution followed by ethanol precipitation. The RNA pellet was dissolved and repeatedly exchanged into NMR buffer (10 mM sodium chloride, 10 mM sodium phosphate at pH ~6.2) using a Centricon

Ultracel YM-3 concentrator (Millipore Corp). The elongated samples were annealed at 95°C for 2 min in H_2O to ensure proper folding, then exchanged into NMR buffer.